Predictive Method for Pipeline Strain Demand Subject to Permanent Ground Displacements with Internal Pressure & Temperature

By

Ismael Samuel Allouche

A thesis submitted in partial fulfillment of the requirements for the degree of

Master of Science

in

Structural Engineering

Department of Civil and Environmental Engineering

University of Alberta

Abstract

Pipelines subject to ground deformations generated by geohazard loads carry high importance on pipeline analysis, design, and assessment due to risk of structural damage or failure. Additionally, internal pressure and temperature variation within an operating pipe induce additional strains in combination with pipe strains generated by ground displacement. In this thesis, these additional loads are implemented in several hypothetical finite element analysis (FEA) simulations to assess the impact of internal pressure and temperature change for pipes subject to ground displacement in soils of varying stiffnesses. Furthermore, an enhanced predictive method is proposed founded upon methods employed by Zheng et al. (2021b) to predict pipeline behaviour subject to permanent ground displacement, while considering effects of internal pressure and temperature variation. The proposed method accounts for the initial thermal strains, and biaxial stress state in the pipe due to hoop stress generated by internal pressure. These additional strains are considered within the expressions of internal axial force and bending moment, derived based on the actual stress distribution on the pipes' cross-section. The accuracy of the proposed method is validated against the finite element method (FEM) with respect to results of pipe strain and deformation using several indicative case studies. This research provides a new effective method of incorporating temperature and internal pressure loads on the inelastic strain demand of pipelines subject to permanent ground displacement of varying types, magnitudes, and directions.

Preface

This is the original work by my research team comprising of myself, Qian Zheng, Dr. Samer Adeeb and Dr. Yong Li of the department of Civil & Environment engineering, structures group. This research was also conducted in collaboration with Enbridge Liquids Pipelines personnel Dr. Nader Yoosef-Ghodsi and Matthew Fowler through the MITACS program. Chapter 2 of this thesis has been published as Allouche, I., Zheng, Q., Yoosef-Ghodsi, N., Fowler, M., Adeeb, S., (2022). Combined Effect of Pressure, Temperature & Soil Stiffness on Pipeline Strain Demand in Geohazard Zones. Proceedings of the ASME Pressure Vessels & Piping Conference, July 17-22, Las Vegas, Nevada, USA. PVP2022-83754. Chapter 2 of this research was also presented by me at the ASME PVP conference under the category of new and emerging methods for pipeline design & analysis in Las Vegas, Nevada, USA on July 20, 2022. Chapter 3 of this thesis has been submitted for publication as Allouche, I., Zheng, Q., Yoosef-Ghodsi, N., Fowler, M., Li, Y., Adeeb, S., (2023), Enhanced Predictive Method for Pipeline Strain Demand Subject to Permanent Ground Displacements with Internal Pressure & Temperature: A Finite Difference Approach, Journal of Infrastructure Intelligence and Resilience. The paper number is yet to be determined and if accepted, will be published under the topic of reliability and risk management of underground energy pipeline systems.

Acknowledgements

This work is supported by the national research organization MITACS and the Natural Sciences and Engineering Council of Canada (NSERC). I would also like to acknowledge my research team for providing great guidance and support throughout my graduate degree endeavors.

TABLE OF CONTENTS

CHAPTER 1

THESIS OVERVIEW **1**

CHAPTER 2
COMBINED EFFECT OF PRESSURE, TEMPERATURE & SOIL STIFFNESS ON PIPELINE STRAIN DEMAND IN GEOHAZARD ZONES

1. INTRODUCTION **1**

2. MATERIALS AND METHODS **2**

2.1 PIPE MATERIAL MODEL 2
2.2 PIPELINE LOADING 3
2.3 SOIL PROPERTIES AND PIPE-SOIL INTERACTION 4
2.4 PIPELINE GEOHAZARD SIMULATIONS: CASE STUDIES 5

3. RESULTS AND DISCUSSION **6**

CHAPTER 3
ENHANCED PREDICTIVE METHOD FOR PIPELINE STRAIN DEMAND SUBJECT TO PERMANENT GROUND DISPLACEMENTS WITH INTERNAL PRESSURE & TEMPERATURE: A FINITE DIFFERENCE APPROACH

4. CONCLUSION **14**

1. INTRODUCTION **17**

2. MATERIALS AND METHODS **19**

2.1 GOVERNING DIFFERENTIAL EQUATIONS 19
2.1.1 Pipe Subject to Ground Displacement *19*
2.1.2 Euler Bernoulli Beam Under Large Deformation *20*
2.2 PIPE MATERIAL & MECHANICAL MODEL 21
2.2.1 Strain Due to Internal Pressure *21*
2.2.2 Strain Due to Temperature Change *22*
2.2.3 Strain Due to Ground Movement *23*
2.2.4 Tensile & Compressive Plastic Slopes *23*
2.3 MODIFIED AXIAL FORCE & BENDING MOMENT EQUATIONS 26
2.3.1 Bending Strain Excluded *26*
2.3.2 Bending Strain Included *26*
2.4 IMPLEMENTATION TO FINITE DIFFERENCE EQUATIONS 29
2.4.1 Finite Difference Notation *29*
2.4.2 Implementation Procedure *30*

3. RESULTS AND DISCUSSION **31**

3.1 CASE STUDIES: PIPE & SOIL PARAMETERS 31
3.2 PRESSURE, TEMPERATURE, PRESSURE & TEMPERATURE 34
3.3 VARYING GROUND DISPLACEMENT MAGNITUDE & GROUND INTERSECTION ANGLE 40
3.3.1 Ground Intersection Angle of 0 Degrees *40*
3.3.2 Ground Intersection Angle of 60 Degrees *41*

3.3.3 Ground Intersection Angle of 90 Degrees ... *42*
3.3.4 Large Strains and Ground Displacements (β = 90˚) ... *43*
3.4 Specified Pipeline Geohazard Case ... 45
4. CONCLUSION ... **47**

CHAPTER 4

SUMMARY AND CONCLUSION ... **50**

BIBLIOGRAPHY ... **51**

APPENDIX A: SUB-FUNCTION OF PYTHON CODE USED FOR PREDICTIVE METHOD ... **53**

APPENDIX B: MAIN-FUNCTION OF PYTHON CODE USED FOR PREDICTIVE METHOD ... **61**

LIST OF TABLES

CHAPTER 2
Table 1: Soil properties for each simulation case 5

CHAPTER 3
Table 1: Soil properties for each soil case 33

LIST OF FIGURES

CHAPTER 2

Figure 1: Bilinear stress-strain response for grade 448 steel 3
Figure 2: Visual interpretation of pipe subject to ground displacement 4
Figure 3: Soil spring properties in each direction 4
Figure 4: Simplified pipeline mode 6
Figure 5: Representation of pipe deformation induced by ground motion & critical locations 7
Figure 6: Vertical pipe deformation for case **I** with & without P&T, δ = 100 mm. 7
Figure 7: Vertical pipe deformation for case **II** with & without P&T, δ = 500 mm. 7
Figure 8: Vertical pipe deformation for case **III** with & without P&T, δ = 500 mm. 8
Figure 9: Vertical pipe deformation for case **IV** with & without P&T, δ = 100 mm. 8
Figure 10: Axial pipe deformation for case **I** with & without P&T, δ = 100 mm. 9
Figure 11: Axial pipe deformation for case **II** with & without P&T, δ = 500 mm. 9
Figure 12: Axial pipe deformation for case **III** with & without P&T, δ = 500 mm. 9
Figure 13: Axial pipe deformation for case **IV** with & without P&T, δ = 100 mm. 10
Figure 14: Strain demand for case **I** with & without P&T 11
Figure 15: Strain demand for case **II** with & without P&T 11
Figure 16: Strain demand for case **III** with & without P&T 11
Figure 17: Strain demand for case **IV** with & without P&T 12
Figure 18: Pipe stresses at L_c^1 for case **I** & **IV** 13
Figure 19: Pipe stresses at L_c^1 for case **II** 13
Figure 20: Pipe stresses at L_c^1 for case **III** 14

CHAPTER 3

Figure 1: Schematic View of Pipe Subject to Ground Displacement 19
Figure 2: Euler Bernoulli beam under large deformation 20
Figure 3: Soil Spring Properties in Each Direction (ALA, 2001) 20
Figure 4: Uniaxial and biaxial state of stress on pipe wall 21
Figure 5: Axial strain and bending strain distribution on the pipe cross-section due to ground movement 23
Figure 6: Uniaxial and biaxial stress-strain relationship for steel pipe 24
Figure 7: Longitudinal strain distribution without bending in the pipe cross-section 26
Figure 8: Longitudinal strain distribution with bending in the pipe cross-section 27
Figure 9: Schematic view for the calculation procedure of the proposed method by Zheng et al. (2021a) 31
Figure 10: Simplified pipeline model 32
Figure 11: Uniaxial and biaxial bilinear stress-strain response for grade 448 steel 32
Figure 12: Representation of pipe deformation induced by ground deformation with critical locations 35
Figure 13: Maximum strain locations in pipe's cross-section 35
Figure 14: Comparison of the proposed method and Abaqus in terms of pipe deformation and longitudinal strain response for Case **I** (δ = 500 mm, β = 90˚) 36
Figure 15: Comparison of the proposed method and Abaqus in terms of pipe deformation and longitudinal strain response for Case **II** (δ = 500 mm, β = 90˚) 36
Figure 16: Comparison of the proposed method and Abaqus in terms of pipe deformation and longitudinal strain response for Case **III** (δ = 500 mm, β = 90˚) 37
Figure 17: Comparison of the proposed method and Abaqus in terms of pipe deformation and longitudinal strain response for Case IV (δ = 500 mm, β = 90˚) 37
Figure 18: Maximum pipe deformation predicted by the PM and Abaqus for all cases 38
Figure 19: Strain demand predicted by the PM and Abaqus for all cases 39
Figure 20: Comparison between PM and Abaqus in terms of strain demand and maximum pipe deformation at different intervals of δ and β = 0˚ 41
Figure 21: Comparison between PM and Abaqus in terms of strain demand and maximum pipe deformation at different intervals of δ and β = 60˚ 42

Figure 22: Comparison between PM and Abaqus in terms of strain demand and maximum pipe deformation at different intervals of δ and β = 90˚ 43
Figure 23: Comparison between PM and Abaqus in terms of strain demand and maximum pipe deformation for large strains at different intervals of δ and β = 90˚ 44
Figure 24: Idealization of pipeline subject to geohazard for specified case 45
Figure 25: Comparison between PM and Abaqus in terms of strain demand and maximum pipe deformation for specified geohazard at different intervals of δ 46
Figure 26: Comparison of the proposed method and Abaqus in terms of pipe deformation and longitudinal strain response for specified geohazard 47

CHAPTER 1

THESIS OVERVIEW

Buried steel pipelines travel vast distances to transport crude oil, natural gas and liquids, and refined products for long distances across various landscapes. As a result, pipelines are inevitably subject to risk of crossing a geohazard zone (unstable landscapes, fault-lines, landslide zones, etc.) where danger of geotechnical or geological failure may induce permanent ground displacement (PGD) onto the pipeline causing severe deformation and damage. Additionally, due to the nature of transmission pipelines, operation at high pressure and varying temperature is required to effectively transport contents. Therefore, consideration of pipeline stresses developed by internal operating pressure and temperature variation during a geohazard event is essential for accurately predicting the pipes physical and mechanical response. Consequently, in the occurrence of a damaged pipeline, pipe rehabilitation or replacement may be required which is costly, impacts pipeline operation, and increases any associated environmental risks (Pipeline & Gas Journal, 2020). By assessing the pipe strains, development of a predictive method can be utilized as a preventative tool for pipeline design and analysis, as well as construction prescreening, where an accurate assessment of fully operating pipelines buried in geohazard zones is developed. The objectives of this research are provided in the introduction section of chapter 2 and chapter 3 of this thesis.

Chapter 2 of this thesis considers developing an effective 3D model using finite element analysis (FEA) software Abaqus Standard to simulate a pipeline subject to a PGD, while considering internal pressure load and temperature change to predict the pipes strain and deformation response. A comparative analysis is also performed for simulation cases of varying soil stiffnesses between cases with and without pressure and temperature loading to study the impact of pressure, temperature, and soil stiffness on pipelines subject to PGD. Results from Chapter 2 act as a justification for the research of developing a new proposed method founded upon methods developed by Zheng et al. (2021b) that includes the influence of internal operating pressure and temperature change.

Chapter 3 discusses development of the predictive method in detail, where a new analytical method is proposed for predicting the pipes strain and deformation response while considering effects of internal pressure and temperature change. This method is modelled according to Euler-Bernoulli beam theory, with consideration of stress biaxiality caused by internal pressure, and material plasticity according to the Von Mises flow rule. The method is solved numerically with Python programming software using the finite difference method, where the pipes strain response is solved incrementally based on the pipes predicted lateral and vertical deformation. The proposed method enhances the method established by Zheng et al (2021b) and is the first to incorporate a model that describes the effects of pressure and temperature in the nonlinear strain demand of pipe subject to ground displacement in both the longitudinal and axial directions.

The main body of this thesis follows a chapter-based format, combining two papers which develop the main body of the thesis. Each chapter in the main body of the thesis includes its own introduction section describing the objective of the research performed as well as review of the literature pertaining to the related work, and advancement of the current research. Results of the work are also concluded within chapter 2 and chapter 3, respectively. There is repeatability in certain figures to emphasize the methods employed in the study performed for the main body of the thesis. Table numbers, figure numbers, and table and figure references in the literature are relative to their respective chapter. Finally, chapter 2 and 3 include their own respective bibliography denoted as the references section containing any references to cited literature within this thesis. The bibliography section is also included which lists all the references contained in this paper.

Chapter 4 of this thesis provides a final summary and conclusion of the results established in this work discussing the capabilities of the developed methods discussed in chapter 2 and chapter 3.

CHAPTER 2

Proceedings of the ASME 2022
Pressure Vessels & Piping Conference
PVP2022
July 17-22, 2022, Las Vegas, Nevada, USA

PVP2022-83754

COMBINED EFFECT OF PRESSURE, TEMPERATURE & SOIL STIFFNESS ON PIPELINE STRAIN DEMAND IN GEOHAZARD ZONES

Ismael Allouche[1], Qian Zheng[1], Nader Yoosef-Ghodsi[2], Matt Fowler[2], Samer Adeeb[1]

[1]University of Alberta, Civil & Environmental Engineering, Edmonton, Alberta, Canada
[2]Enbridge Liquids Pipelines, Edmonton, Alberta, Canada

ABSTRACT

Pipelines subject to ground deformations produced by geohazard loads carry high importance on pipeline analysis, design, and assessment due to risk of structural failure. An appropriate approach for evaluation is the finite element method (FEM), providing efficient and sophisticated results. Methods proposed by Zheng et al. (2021) using finite element analysis (FEA) software Abaqus/Standard provide highly accurate results by simulating a displacement-controlled analysis of buried steel pipes subject to ground displacement of varying magnitudes and direction. This paper aims to further develop this pipe strain demand assessment by including variable effects of internal pressure and temperature of steel pipes buried in soils of different stiffness. The developed strain demand criterion considers inelastic material behaviour for different grades of steel pipe, as well as bi-linear soil force-displacement interaction, accounting for soil plasticity (ALA, 2001). Assuming the effects of thermal expansion are negligible prior to ground motion initiation, the pipe loads can be assessed by modelling a pipeline with initial temperature and pressure loads, followed by a ground motion in a series of steps. Several case studies were performed by modelling an X65 grade pipeline subject to ground displacements varying from 100 to 1000 mm, across a length at the midsection of the pipe. Simulations are assessed with a specified temperature increase, and internal pressure required to induce an operating hoop stress of up to 80% of the specified minimum yield strength (SMYS). By assessing the pipeline in soils of different stiffness (low, intermediate, high) at different increments of ground displacement, an accurate representation of the material stress/strain response can be acquired for each respective case. This research may provide guidance for further studies of pipelines involving internal pressure & temperature.

Keywords: pipeline, deformation, geohazard, finite element method, strain demand, displacement-controlled, inelastic, internal pressure, temperature, soil stiffness

1. INTRODUCTION

Buried steel pipelines transport contents over vast distances and varying geographies, where risk of geological failure caused by geohazards is apparent. Pipelines subject to permanent ground deformations induced by geohazard loads such as earthquakes, landslides, creep of slopes, thaw settlements, frost heave or other phenomena may experience large strains (Yoosef-Ghodsi, 2008). This will inevitably impact pipeline structural integrity, and therefore directly influence pipeline operation. Strain demand analysis recognizes that pipes retain large portions of their structural capacity, even under initial plastic deformation in contrast to the conventional stress-based design methods (C-FER Technologies, 2020).

The finite element method is a widely accepted computational tool when analyzing pipelines subject to ground deformation where sophisticated models developed in Abaqus/Standard provide high variability with respect to element type, size, pipeline constitutive model, and pipe-soil interaction (Zheng et al., 2021). Several studies have been developed using finite element simulation such as Takada et al. (2001), where Euler-Bernoulli beam shell elements were utilized to help predict the flexural response of a pipeline near the fault plane due to fault displacement. This method was further developed by Liu et al. (2016), where applying equivalent boundary conditions to the ends of the pipe helped predict the effects of yield strength and strain hardening parameters on the buckling behaviour of high-strength pipes (Zheng et al., 2021).

When accounting for the soil/pipe-soil model representation, research conducted by Vazouras et al. (2015) and Sarvanis et al. (2018) suggested solid elements with contact constraints defined for the pipe-soil interface. For simplification, soil springs are recommended by ALA guidelines (ALA, 2001), accounting for crucial pipe-soil interaction properties characterized by a bilinear soil displacement response. These properties consider soil stiffness parameters, yield displacements, burial depth, and pipe geometry. This technique allows for ease of implementation when inputting parameters during simulation and analysis. Methods developed by Zheng et al. (2021) utilizing Abaqus/Standard help predict the strain demand and deformation of steel pipes subject to ground displacement for both longitudinal and transverse loading. An arbitrary ground motion simulation is modelled using pipe elements derived from Euler-Bernoulli beam elements for the pipeline (Dassault Systems Simulia Corporation, 2022). Fewer pipe elements allow for finer convergence results and are selected based on the relative length of the pipeline and optimal execution period. A finer mesh is selected for elements directly impacted by the region of ground displacement. Techniques established by ALA guidelines (2001) for the pipe-soil interaction, provide highly accurate results for strain demand analysis. The pipe is simulated by PIPE32 elements (3-node quadratic pipe in space), widely utilized in practice of preliminary design for pipes against geohazards (Zheng et al., 2021). This model also accounts for material non-linearity, where plastic strains can be developed depending on the magnitude of ground displacement. It was found that the magnitude of ground motion provides a greater influence on pipe strains in contrast to the direction of ground motion (Zheng et al., 2021).

It is also noted that the pipe-soil interaction heavily influences the allowable strain capacity that may be developed by a pipe subject to ground displacement (ALA, 2001). Strain demand analysis can still be further developed to include effects of internal operating pressure and temperature, allowing for more sophisticated predictions when a pipe experiences ground movement. An analytical model developed by Yoosef-Ghodsi et al. (2008) considers the impact of internal pipe pressure and temperature change on pipelines subjected to longitudinal ground movement. It was concluded that internal pressure tends to induce axial tension in the pipe, while temperature tends to induce axial compression (Yoosef-Ghodsi et al., 2008). The specified soil constraint assumed no additional longitudinal displacement or strain, although this is not the case for other pipe-soil constraints. No studies have looked at this effect on pipes subjected to lateral or inclined ground movements.

The objective of this paper is to investigate the additional effects of internal operating pipe pressure and temperature loads on strain demand of pipes subjected to general ground movements. Four hypothetical cases are studied to test the impact of pressure and temperature in soils of varying stiffness, assessing the overall influence on pipeline strain demand and deformation as a result.

2. MATERIALS AND METHODS

2.1 Pipe Material Model

The model developed by Zheng et al. (2021) was enhanced with the inclusion of the effects of internal pressure and temperature change. As described by Yoosef-Ghodsi et al. (2008), the presence of internal pressure results in a biaxial state of stress rather than the explicit use of a uniaxial stress-strain relationship. Therefore, the steel response is considered as a bilinear curve with elastic modulus E, and strain-hardening modulus E_m. This paper assumes that the effect of temperature on the material yield stress of the steel is negligible. The hypothetical material used for the pipe is considered as X65 grade 448 steel.

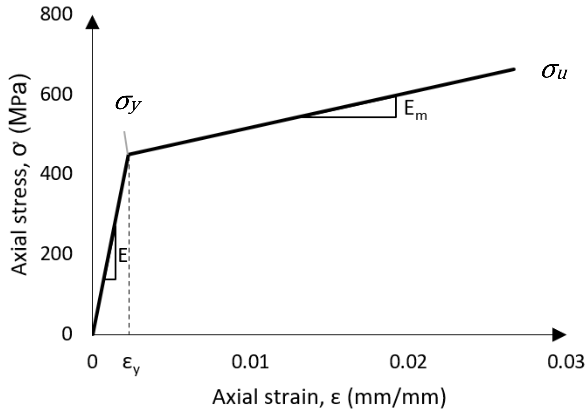

Figure 1: Bilinear stress-strain response for grade 448 steel

Where:
Yield strain, ε_y = 0.00226 mm/mm.
Yield stress, σ_y = 450 MPa.
Ultimate tensile strength, σ_u = 663 MPa.
Modulus of elasticity, E = 199 GPa
Strain hardening modulus, E_m = 7.68 GPa

The equivalent plastic strain is calculated using Abaqus/Standard definition of plasticity.

$$\varepsilon^{pl} = \varepsilon_t - \frac{\sigma}{E} \tag{1}$$

Where:
ε_t = True total strain.
σ = True stress.
ε^{pl} = True plastic strain.

By setting $\sigma = \sigma_u$ and ε_t = 0.03 mm/mm, the equivalent plastic strain corresponding to the ultimate stress is calculated as ε^{pl} = 0.0267 mm/mm for grade 448 steel.

2.2 Pipeline Loading

The finite element model developed considers three different loads, applied sequentially in a series of steps on the pipeline: internal operating pressure, temperature differential, and ground displacement. The model established considers the simulation as general static motion defined by the finite element method using Abaqus.

The biaxial state of stress is considered by the circumferential hoop stress (σ_h) generated by the internal pressure. According to CSA Z662:19 standard, the allowable operating hoop stress is limited to 80% of the specified minimum yield stress (SMYS), applied prior to ground motion initiation. Barlow's formula is used to calculate the hoop stress as

$$\sigma_h = \frac{P(D-2t)}{2t} \leq 0.8\sigma_y \tag{2}$$

Where:
P = internal pressure.
D = outside diameter of pipe.
t = pipe wall thickness.

Using grade 448 material properties results in allowable operating hoop stress of 360 MPa. This provides the maximum allowable influence of internal pipe pressure according to CSA Z662:19 standard.

Additionally, a uniform temperature differential of -30 ℃ to +30 ℃ is applied to the entirety of the steel pipe. The temperature change refers to the change in temperature from regular operating conditions to the time when ground motion is apparent. The temperature change was selected to emulate realistic seasonal variations experienced by the pipeline. Temperature effects on pipe strains are deemed negligible prior to ground motion initiation due to the bounds provided by the pipe-soil interaction.

The pipeline is modelled as a straight pipe crossing a geohazard zone, such as a landslide inducing a permanent ground deformation. The load generated by the geohazard is represented as a displacement-controlled analysis, with the segment of ground movement characterized as a sliding block with magnitude δ. The direction of the ground displacement is separated into axial and vertical components, denoted as U and W respectively. The angle at which the pipe longitudinal axis and ground movement intersect is considered the ground intersection angle, β (Figure 2).

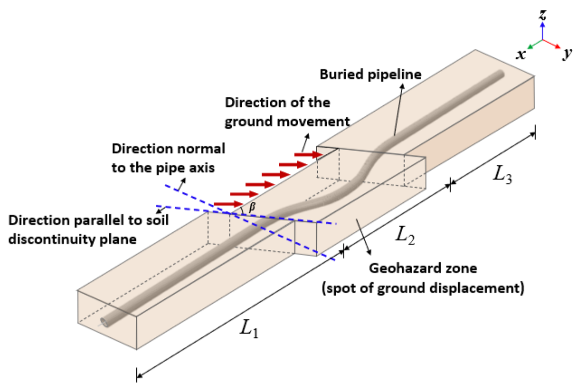

Figure 2: Visual interpretation of pipe subject to ground displacement

For this study, it was determined that the magnitude of ground motion carried high impact on analysis results in contrast to the direction of ground motion. It was also discovered that analyses with β = 90˚ developed the most significant outcomes when including pressure and temperature in the pipe. Simulations were performed for a range of δ between 100 mm and 1000 mm, increasing by increments of 100 mm.

2.3 Soil Properties and Pipe-Soil Interaction

The soil simulation is modelled according to ALA guidelines, with bilinear soil displacement response interaction (ALA, 2001). Non-linear soil springs were considered for modelling the relationship between the stiffness of the soil onto the pipe in the event of ground displacement in the axial, lateral, and vertical directions.

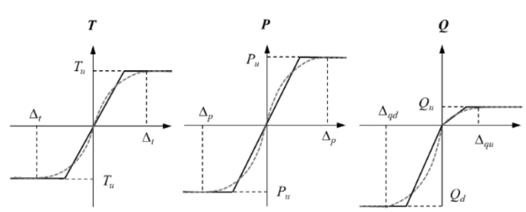

(a) Axial **(b) Lateral** **(c) Vertical**

Figure 3: Soil spring properties in each direction

From Figure 3:

T_u = Soil resistance in the axial direction.
Δt = Displacement in the axial direction.
P_u = Soil resistance in the lateral direction.
Δp = Displacement in the lateral direction.
Q_u = Soil resistance in bearing direction (vertical upward).
Δq_u = Displacement in bearing direction.
Q_d = Soil resistance in uplift direction (vertical downward).
Δq_d = Displacement in uplift direction.

Figure 3 represents the soil force on the pipe against the displacement in the three directions identified, with the dashed lines illustrating this soil property as a bilinear curve. The values of these parameters depend on the soil classification, pipe diameter, burial depth, and coating of the pipe (ALA, 2001).

According to the unified soils classification system (USCS) adopted by ASTM D-2487-98 (2017), soils may be classified and identified for general engineering purposes. A generalized categorization of soil strength denoted as weak, intermediate, and strong soil was adopted for this study. The relative "strength" of the soil is dependent on the stiffness parameter and relative yield displacement in the specified directions, with large influence carried by the soil bearing capacity. Classification of soil strength was established during the analysis phase of this study based on the resultant pipe strains.

2.4 Pipeline Geohazard Simulations: Case Studies

After performing numerous trial simulations, it was deemed that altering pipe size or ground intersection angle (β) provided considerably less significant impact on results directly related to effects of temperature and pressure when compared to varying ground motion magnitude, and soil stiffness. Therefore, pipe length, size, and β were maintained constant for the four case studies performed.

The critical analyses are separated into four separate case studies based on the soil stiffness and loading to better determine the impact of implementing pressure and temperature. Case **I**, **II**, and **III** are identified as soft clay (weak), firm clay (intermediate), and stiff clay (strong) respectively. Case IV is classified as the same soil in Case **I**, but with half the applied internal pressure and temperature loading.

A theoretical straight pipeline was modelled with the following parameters for all cases.

X65 Steel Pipe:	**Pipe Geometry:**	**Soil Properties:**
Grade 448 Steel.	D = 508 mm. t = 7.14 mm. Pipe length, L = 210 m.	Soil properties for each case are classified in TABLE 1.

Table 1: Soil properties for each simulation case

Parameter	Case I	Case II	Case III	Case IV
T_u (kN/m)	1.4	14	14	1.4
Δt (mm)	5	8	5	5
P_u (kN/m)	20.4	40	40	20.4
Δp (mm)	46	51	46	46
Q_u (kN/m)	20.4	60	513	20.4
Δq_u (mm)	46	65	92	46

The pipe is buried at a depth of 1.8 m to the centerline of the pipe from the surface of the ground.

Pipeline Loading:

Case I, II, III
P = 10260 kPa.
ΔT = + 60 ˚C.
β = 90˚.
δ = 100 to 1000 mm (in increments of 100 mm).

Case IV
P = 5130 kPa.
ΔT = + 30 ˚C.
β = 90˚.
δ = 100 to 1000 mm (in increments of 100 mm).

The pipe is loaded symmetrically (the transverse soil resistance at both sides of the pipe is the same), with the pipeline crossing a 10-meter geohazard zone across the mid-point location of the pipeline in the longitudinal direction. The geohazard zone induces ground motion according to the relative pipeline loading.

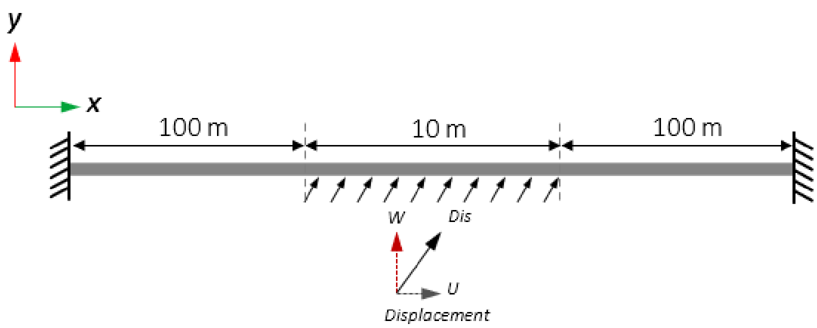

Figure 4: Simplified pipeline mode

The mesh of the pipeline includes 51 nodes for each of the 100 m spans between the supports and geohazard zone, while a finer mesh of 11 nodes was selected for the 10m span within the geohazard zone.

3. RESULTS AND DISCUSSION

Results for each simulation case indicate that the inclusion of internal pressure & temperature provides significant increase on pipeline strain demand, and pipe deformation in both the vertical and axial directions for the segment of pipe located within the geohazard zone. This increase is proportional to the magnitude of temperature and pressure applied to the pipes.

The maximum tensile and compressive longitudinal strain occurs at the top and bottom extreme fibres of the pipes cross-section, located at the center-span of the pipeline and near the end-zones of the ground displacement. These critical locations are identified in Figure 5 by the red dashed lines on the deformed pipe. L_c^1 represents the location along the pipe near where the ground motion is first initiated, L_c^2 represents the location at the center of the pipeline, and L_c^3 represents the location along the pipe near where the ground motion ends, with respect to the longitudinal direction. L_c^1 and L_c^3 are equal distances from the center of the pipeline due to symmetry in geometry and loading.

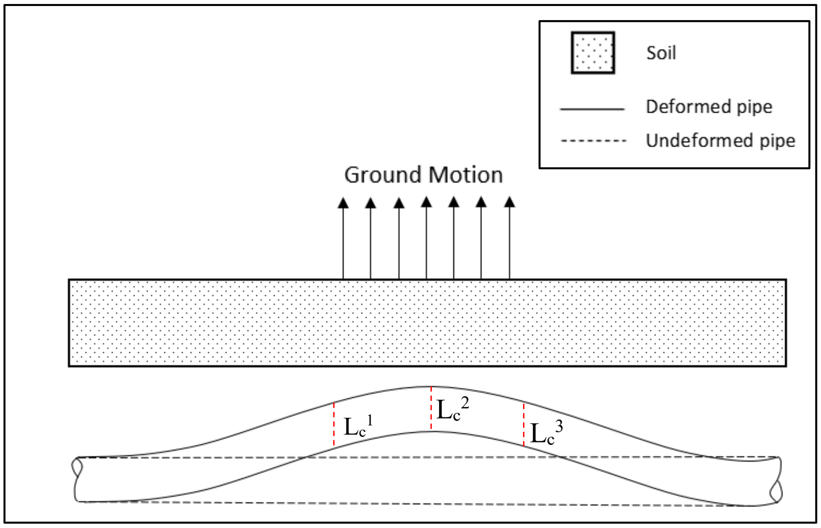

Figure 5: Representation of pipe deformation induced by ground motion & critical locations

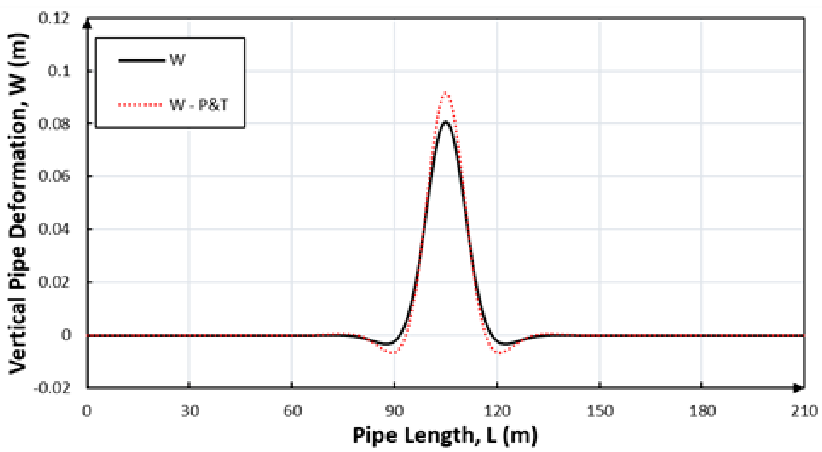

Figure 6: Vertical pipe deformation for case I with & without P&T, δ = 100 mm.

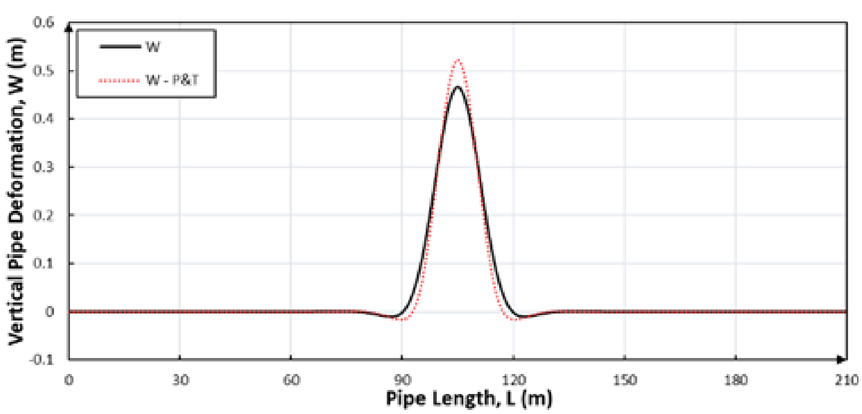

Figure 7: Vertical pipe deformation for case II with & without P&T, δ = 500 mm.

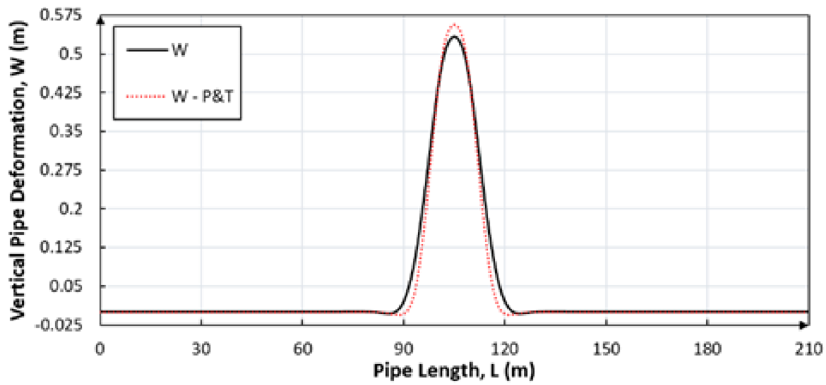

Figure 8: Vertical pipe deformation for case III with & without P&T, δ = 500 mm.

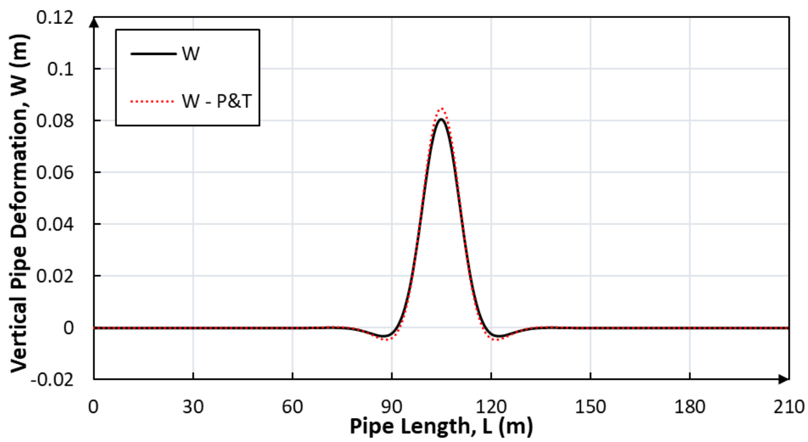

Figure 9: Vertical pipe deformation for case IV with & without P&T, δ = 100 mm**.**

The relative distance from the left support of the pipeline indicated in Figure 4 to the critical locations are L_c^1 = 92 m, L_c^2 = 105 m, and L_c^3 = 118 m. The critical locations are based on the pipe size, geometry, load symmetry, and direction of ground displacement.

Each case study was compared to a model with identical parameters but excluding internal pressure and temperature loading, respectively. P&T in Figures 6-17 are denoted as the case with pressure and temperature included. An arbitrary magnitude of ground motion was selected for each case to assess the deformation response along the length of the pipeline. Weak soil was evaluated at smaller ground displacement (δ = 100 mm), while intermediate/strong soil was evaluated at larger ground displacement (δ = 500 mm). This paper advises evaluating deformation response at lower magnitudes for weaker soils to maintain model convergence and stability.

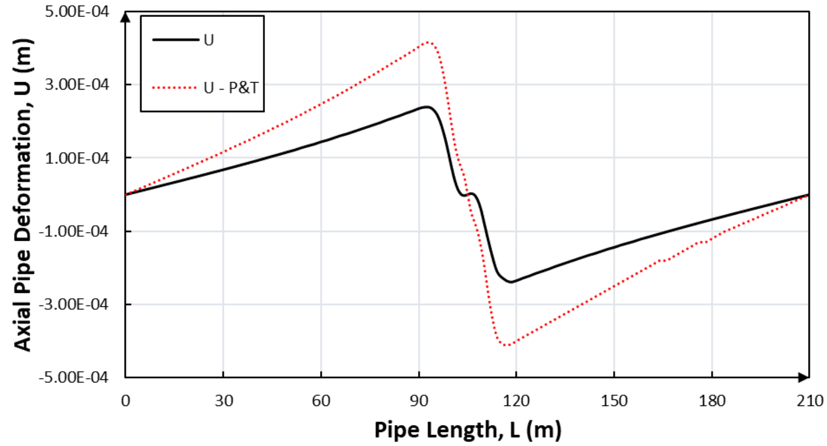

Figure 10: Axial pipe deformation for case I with & without P&T, δ = 100 mm.

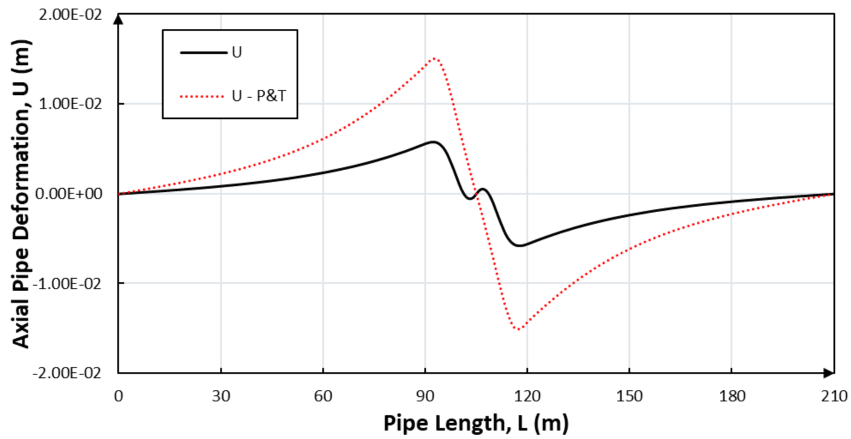

Figure 11: Axial pipe deformation for case II with & without P&T, δ = 500 mm.

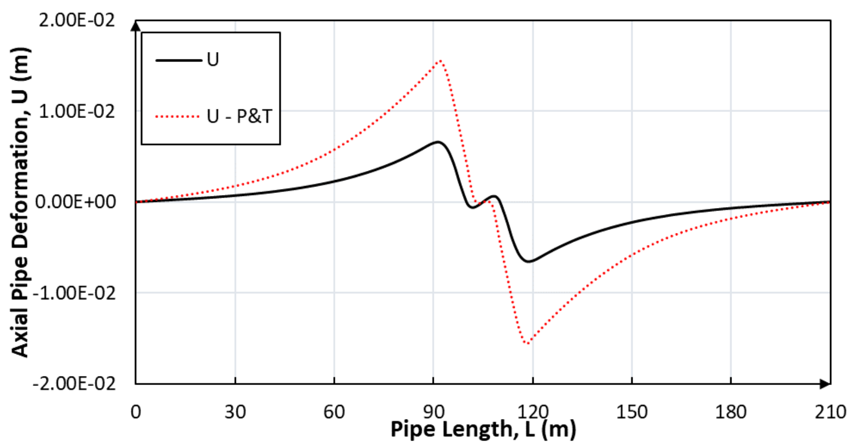

Figure 12: Axial pipe deformation for case III with & without P&T, δ = 500 mm.

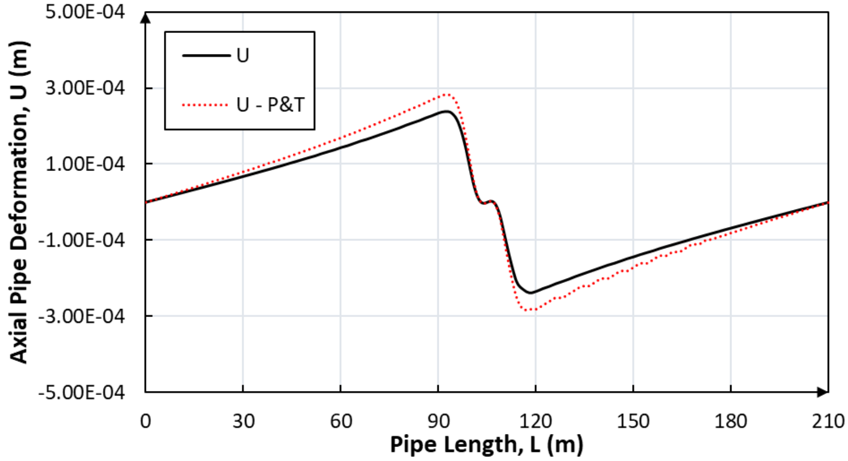

Figure 13: Axial pipe deformation for case IV with & without P&T, δ = 100 mm.

Figures 6-9 illustrate the vertical pipe deformation induced by the ground motion for each case compared to the same case excluding pressure and temperature. The profiles for each figure indicate higher response occurred at the critical locations. For Case I, deformations increased by up to 13.7% when compared to analysis without pressure and temperature. Case II and III resulted in an increase of up to 11.7% and 4.5%, respectively. Case IV produced results less significant due to less internal pressure and temperature differential, with maximum deformation increasing by 5.5%. The largest vertical displacements occurred at L_c^2. Small negative deformation is apparent at the critical locations due to the interaction of the soil resistance in accordance with the bending response.

Figures 10-13 illustrate the axial pipe deformation induced by the ground motion for each case compared to the same case excluding pressure and temperature, once again with the maximum response occurring at critical locations L_c^1 and L_c^3. Change in axial deformation due to including internal pressure and temperature load indicates higher significance in contrast to impact on vertical deformation. Case I illustrates an increase in pipe deformation of up to 72.9%. Case II and III resulted in an increase of up to 159% and 139%, respectively. Analysis of Case IV shows an increase of up to 17.5% in axial deformation. Axial pipe displacement carries high disparity due to relatively small deformations, greater impacted by inclusion of pressure and temperature.

Temperature and pressure effects on vertical pipe deformation tend to be less significant due to the relatively high bearing stiffness and soil yield displacements in the vertical direction compared to the soil springs interacting with the pipe in the lateral and axial directions. Stronger soil tends to allow for less additional deformation overall, depending on the magnitude of ground motion, and relative soil-spring stiffness in the specified direction. Deformation response is heavily dependent on the pipe's capacity to remain intact with the soil as ground motion occurs. After a certain magnitude of ground displacement, the soil force-displacements will yield and thus plastify, constraining the pipes' ability to deform further as ground motion continues to increase. The magnitude of ground motion required to cause the soil to plastify increases as the soil stiffness increases. This phenomenon is disrupted by including internal pressure & temperature due to the biaxial state of stress in the steel and an increased strain rate due to temperature, promoting inelastic material behavior of the pipe at the critical locations. Pipe deformation will further develop as ground displacement increases, depending on the magnitude of internal pressure and temperature applied to the pipe, as well as the soil stiffness.

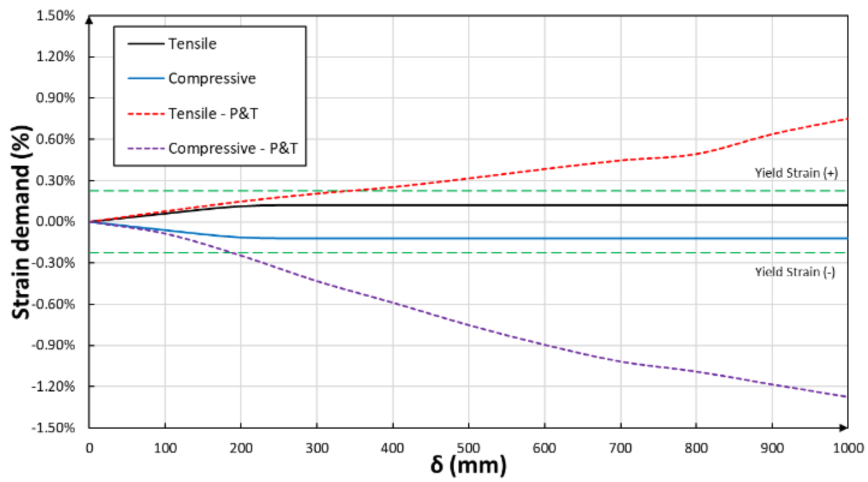

Figure 14: Strain demand for case I with & without P&T

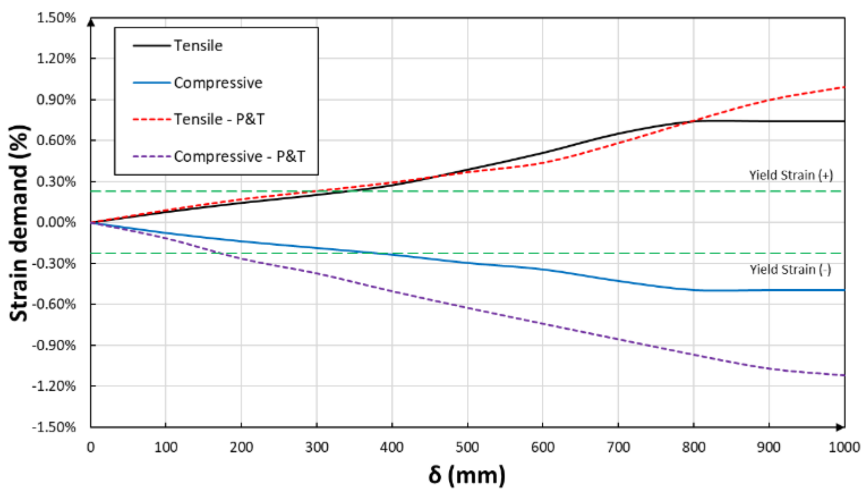

Figure 15: Strain demand for case II with & without P&T

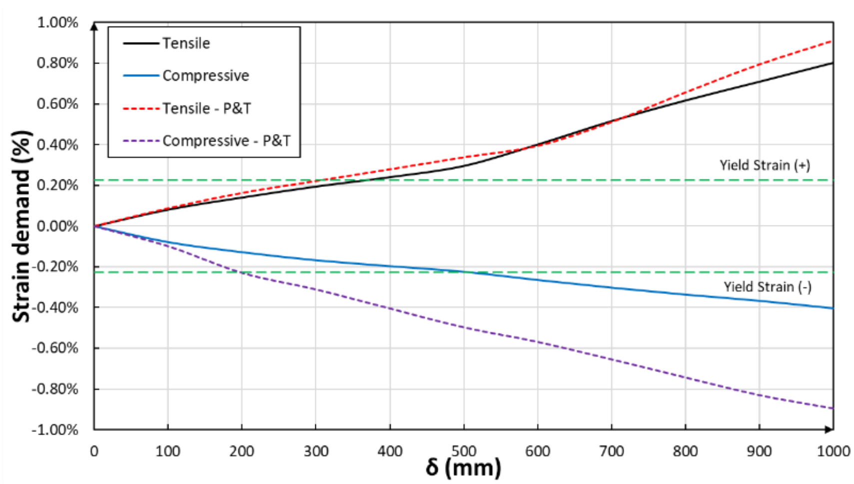

Figure 16: Strain demand for case III with & without P&T

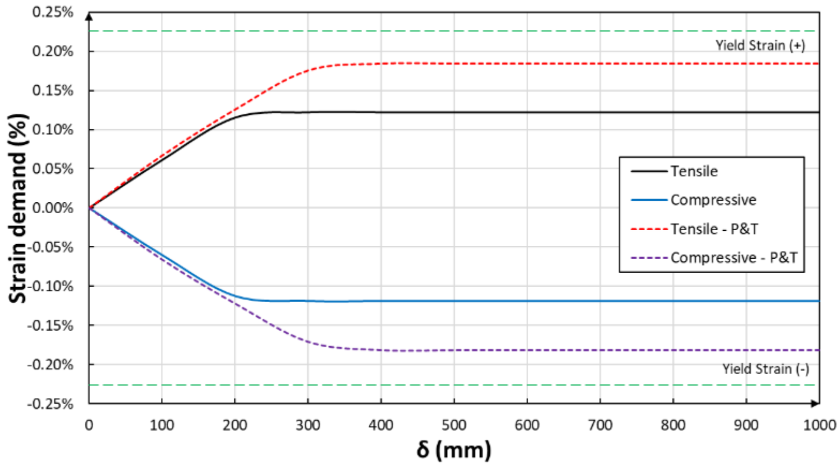

Figure 17: Strain demand for case IV with & without P&T

Figure 14 demonstrates how implementing maximum allowable pressure and temperature result in a monotonic increase in strain demand as magnitude of ground displacement increases for Case I. When the model excludes pressure and temperature, the soil plastifies at a ground displacement of 220 mm, resulting in the pipe strains plateauing at 0.12% in both compression and tension. The pipe strains remain elastic and cease to further increase due to the pipe passing through the soil.

For the case of pressure and temperature, strains further develop as ground motion increases, with the pipe remaining intact with the soil. This is a result of the soil failing to reach yield displacement prior to the pipe yielding at all critical locations. The compressive pipe strain demand at δ = 200 mm is 0.25%, surpassing the yield strain (dashed green lines) of the steel, and continues to deform inelastically as δ increases. Strain demand significantly increases at larger ground motion due to elevated material non-linearity, where the pipe continues to plastically deform until material failure.

Similarly, Case II illustrates how a stiffer soil yields at larger ground motion (δ = 800 mm). Stiffer soil also allows the pipe to achieve material non-linearity due to experiencing greater induced strains by remaining intact with the soil for larger magnitudes of ground displacement. Excluding pressure & temperature results in the pipe plateauing at a compressive strain demand of 0.49% and tensile strain of 0.74%, respectively. With pressure and temperature, the profile of the tensile strain remains consistent until evidently increasing passed δ = 800 mm. The compressive strain demand increases at all instances of ground displacement, with the margin of disparity increasing proportionally with δ when compared to the case of no pressure and temperature (97% increase in strain demand at δ = 800 mm). The monotonic increase in strains is attributed to the steel yielding at critical locations L_c^1 and L_c^3 in the pipe prior to the soil plastifying.

Figure 16 demonstrates that the strain demand of the pipe becomes inelastic at lower increments of ground displacement when buried in strong soil. For Case III, the pipe remains intact with the soil at larger ground motion due to high pipe-soil stiffness interaction, allowing for larger induced strains. Distinct from the other cases, the pipe achieves material non-linearity at all critical locations with and without pressure and temperature. This relationship causes the soil displacements to remain elastic for larger ground deformation, while the steel continues to develop inelastic strains until inevitably reaching failure. Pressure and temperature effects for the pipe buried in strong soil primarily result in increased strain, with compressive strains most impacted. This paper concludes that steel pipes buried in intermediate to stiff soil follow relatively similar strain demand as ground motion increases, with the soil plastifying at larger ground motion as stiffness increases.

Figure 17 shows that the strain demand response for Case IV remains entirely elastic due to the reduced pressure and temperature loads. Contrary to Case I, the soil now yields at a larger ground motion of 330 mm, rather than increasing monotonically. The pipe strains plateau at 0.18% in both compression and tension, resulting in an increase of 53% when compared to the pipe without pressure and temperature load. This is a result of the pressure and temperature differential being low enough for the pipe to remain elastic at the critical locations, in specific near the end locations of the geohazard zone (L_c^1 and L_c^3). This paper concludes that as internal pressure and temperature variation increase, the strain demand of the pipe will also increase and plateau at larger ground displacement, such that the soil plastifies prior to yielding of the steel at the critical locations.

According to ASME B31.4/31.8 buried pipelines that are continually supported may be evaluated under the Von Mises failure criteria. Therefore, the output for the material yield stresses using the Von Mises criterion computed by Abaqus/Standard was employed to identify the pipe stresses at different ground displacements. Figures 18-20 illustrate the maximum stresses in the pipe for all cases near the initial point of the geohazard zone, L_c^1, as ground displacement increases.

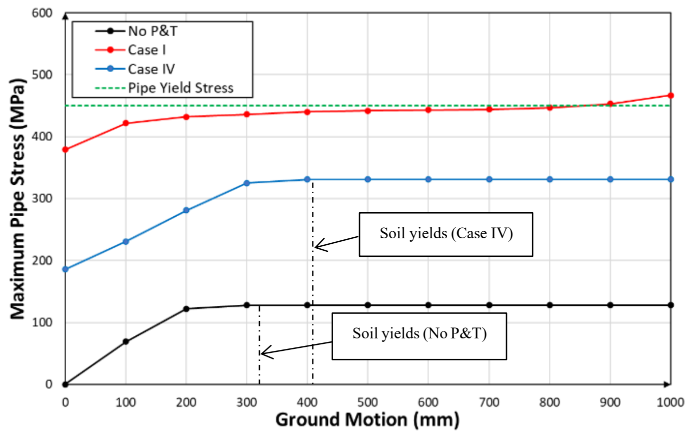

Figure 18: Pipe stresses at L_c^1 for case I & IV

It is evident that the pipe stresses increase and may eventually yield depending on the magnitude of pressure or temperature load as depicted in Figure 18. Verifying the strain demand results, soil tends to plastify at larger ground motion proportionately with applied pressure and temperature load.

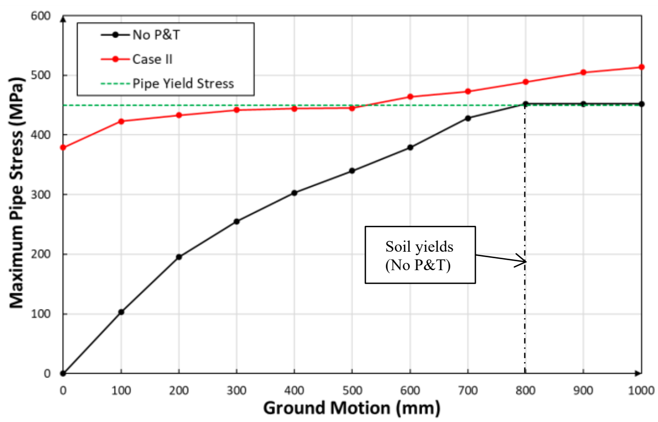

Figure 19: Pipe stresses at L_c^1 for case II

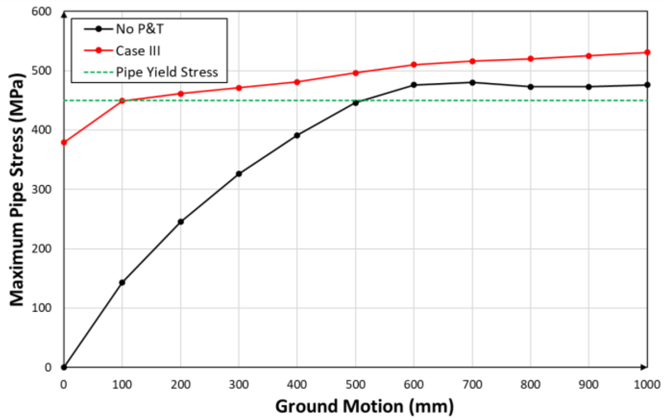

Figure 20: Pipe stresses at L_c^1 for case III

Figure 19 illustrates that the pipe for Case II yields and becomes inelastic at δ = 500 mm, prior to the soil plastifying at δ = 800 mm for the case without pressure and temperature. Figure 20 indicates that the pipe also yields at lower ground displacement of 100 mm compared to 500 mm, with higher stresses experienced by the pipe in both cases. Validating the strain response, Figure 19 demonstrates that the pipe material becomes non-linear at earlier magnitudes of ground motion at the specified location L_c^1 in the pipe. The influence of pressure and temperature is apparent, and this paper considers that pipelines may behave non-linearly if internal pressure and temperature load induce enough stress, which will influence the pipe-soil stiffness interaction and ultimately the maximum pipe deformation induced by a geohazard.

4. CONCLUSION

Geohazards pose significant risk for inducing large displacements to pipelines buried within geohazard zones, where risk of pipe failure is largely apparent. Results from four case studies analyzed using Abaqus/Standard suggest that the combined effect of internal pressure and temperature amplify the overall pipe deformation (axial & vertical) and strains, with significant impact on compressive strain at the top and bottom extreme fibres of the pipes' cross-section. Large pressure and temperature load in conjunction with increasing ground displacement produce considerable strains at the pipe's critical locations, with potential for inelastic material behaviour. This results in monotonic increases in pipe strains, where the soil plastifies at different stages based on the relative pipe-soil stiffness interaction, and magnitude of pressure and temperature. This discrepancy may be evident when comparing the relative increase in strains to models which exclude effects of pressure and temperature, where soil is expected to plastify at earlier magnitudes of ground motion, potentially underpredicting additional pipe strains. It is also found that whether the pipe material plastifies or not is heavily dependant on the relative soil stiffness, where soil stiffness carries an inverse relationship to the added effects of pressure and temperature. This is the first paper to describe the role of pressure and temperature in the nonlinear strain demand of pipes subjected to ground movement. Considering the additional loads provides more robust findings with greater relatability to real-world pipe operation.

ACKNOWLEDGEMENTS

This work is supported by MITACS and the Natural Sciences and Engineering Council of Canada (NSERC).

DISCLAIMER

REFERENCES

[1] Zheng, Q., Graf-Alexiou, G., Li, Y., Yoosef-Ghodsi, N., Fowler, M., Kainat, M., Adeeb, S., Strain demand of elastic pipes subjected to permanent ground displacements using the finite difference method, 2021.

[2] Takada, S., Hassani, N., Fukuda, K., A new proposal for simplified design of buried steel pipes crossing active faults. Earthq. Eng. Struct. Dyn. 30 (8), 2001, 1243–1257.

[3] Liu, X., Zhang, H., Li, M., Xia, M., Zheng, W., Wu, K., Han, Y., Effects of steel properties on the local buckling response of high strength pipelines subjected to reverse faulting. J. Nat. Gas Sci. Eng. 33, 2016, 378–387.

[4] Vazouras, P., Dakoulas, P., Karamanos, Pipe–soil interaction and pipeline performance under strike–slip fault movements. Soil Dyn. Earthq, S.A., 2015, Eng. 72, 48–65.

[5] Sarvanis, G.C., Karamanos, S.A., Vazouras, P., Mecozzi, E., Lucci, A., Dakoulas, P., Permanent earthquake-induced actions in buried pipelines: numerical modeling and experimental verification. Earthq. Eng. Struct. Dyn. 47 (4), 2018., 966–987.

[6] Yoosef-Ghodsi, N., Zhou, J., Murray, D.W., A simplified model for evaluating strain demand in a pipeline subjected to longitudinal ground movement. In: Proceedings of the International Pipeline Conference, 2008, p. 48593.

[7] Lin, Y., Lv, Y., Liu, X., Chen, F., Analysis of Longitudinal Mechanical Properties of Buried Suspended Pipeline Resisting Collapse, Advances in Civil Engineering, V. 2019, Article ID 3954390, 10p., 2019.

[8] American Lifelines Alliance, American Society of Civil Engineers, Guidelines for the Design of Buried Steel Pipe, 2001

[9] ASTM International, ASTM D2487, Standard Practice for Classification of Soils for Engineering Purposes (Unified Soil Classification System), 2017.

[10] CSA Group, CSA Z662:19, Oil and Gas Pipeline Systems, 2019.

[11] C-FER Technologies, a Subsidiary of Alberta Innovates, Strain Based Design, https://www.cfertech.com/2020/03/03/strain-based-design/, viewed January 21, 2022.

[12] Dassault Systems Simulia Corporation, Abaqus Overview, https://www.3ds.com/products-services/simulia/products/abaqus/, 2022.

[13] ASME B31.4, 2019 Edition, November 1, 2019 - Pipeline Transportation Systems for Liquids and Slurries.

CHAPTER 3

ENHANCED PREDICTIVE METHOD FOR PIPELINE STRAIN DEMAND SUBJECT TO PERMANENT GROUND DISPLACEMENTS WITH INTERNAL PRESSURE & TEMPERATURE: A FINITE DIFFERENCE APPROACH

Ismael Allouche[1], Qian Zheng[1], Nader Yoosef-Ghodsi[2], Matt Fowler[2], Yong Li[1], Samer Adeeb[1]

[1]University of Alberta, Civil & Environmental Engineering, Edmonton, Alberta, Canada
[2]Enbridge Liquids Pipelines, Edmonton, Alberta, Canada

ABSTRACT

Pipelines subject to ground deformations generated by geohazard loads carry high importance on pipeline analysis, design, and assessment due to risk of structural damage or failure. Additionally, internal pressure and temperature variation within an operating pipe induce additional strains in combination with pipe strains generated by ground displacement. In this study, an enhanced predictive method is proposed founded upon methods employed by Zheng et al. (2021b) to assess pipeline behaviour subject to permanent ground displacement, while considering effects of internal operating pressure and temperature variation. The finite difference-based method previously proposed for strain analysis of buried steel pipes subject to ground movement ignores the effects of internal pressure and/or temperature loading, limiting the applicability of this approach to exclude the operating conditions of pipelines. To address this limitation, the proposed enhanced method accounts for the initial thermal strains and biaxial stress state in the pipe due to hoop stress generated by internal pressure. These additional strains are considered within the expressions of internal axial force and bending moment, derived based on the actual stress distribution on the pipe cross-section. The accuracy of the proposed method is validated against the finite element method (FEM) with respect to results of strain and deformation demand using several indicative case studies. This research provides an effective method of incorporating temperature and internal pressure loads of pipelines subject to permanent ground displacements of varying types, magnitudes, and directions.

Keywords: pipeline, strain demand, deformation, ground displacement, inelastic, pressure, temperature, finite-difference method.

1. INTRODUCTION

Buried steel pipelines transport contents over vast distances and varying geographies, where geological risk caused by geohazards is apparent. Pipe segments are inevitably installed through geotechnically unstable environments, where risk of geological failure such as landslides, discontinuous permafrost (frost heave and thaw settlement), slope failures, ground subsidence, tectonic shifting, etc. is prevalent (Zheng et al., 2021). Pipelines subject to permanent ground deformations induced by geohazard loads may experience large strains, altering the mechanical integrity of the pipe material (EWI, 2007). This will inevitably impact pipeline structural integrity, and therefore directly influence pipeline operation. Strain demand analysis reveals that pipes retain large portions of their structural capacity, even under initial plastic deformation (C-FER Technologies, 2020). Strain demand analysis can still be further developed to include effects of internal operating pressure and temperature variation, allowing for more realistic predictions when a pipe experiences ground movement. Although several standard methods are fairly accurate (finite element analysis, experimental procedures, etc.), they require extensive time and resources when providing a precise simulation of a geohazard problem.

Presently, physical experimental studies of various scales have been conducted to validate the analytical procedures and finite element models using results of buried pipe response due to ground-induced deformation (O'Rourke MJ, 2005; Ha D, 2008; Rofooei FR, 2012; Feng W, 2015).

In the literature, several analytical methods have been developed to study the pipe response due to ground-induced deformation. Newmark and Hall (1975) originated the analytical study of pipelines subject to ground movement by means of solving pipe response to tectonic fault-based displacement under the small deflection assumption. Kennedy et al. (1977) extended this research by considering large deflections of pipes, assuming single constant curvature near the fault plane (Kennedy, 1977). These methods assume only axial tensile force is developed at the inflection point of the pipe, disregarding flexural behaviour. To account for bending rigidity and flexural response, Wang and Yeh (1985) further explored pipe's performance by establishing a connection to the shear force at the inflection point, modelling the pipe as a semi-infinite beam on an elastic foundation, yielding more coherent results (Wang LRL, 1985; Yeh Ya, 1986). To account for the mechanical behavior more realistically, Karamitros et al. (2007) proposed a refined method introducing both material and geometric nonlinearity, developing an analytical approach with greater applicability and prediction capability. In addition, improved methods based on subsequent studies such as Trifonov et al. (2011), Vazouras et al. (2015), and Liu et al. (2016) helped refine analytical pipe models by examining longitudinal deformation effects, and consideration of large deformation on pipe bending stiffness. Although these analytical methods provide reliable prediction on pipe response to ground deformation, all models are established specifically with regards to tectonic faults where only one ground discontinuity is observed, and cannot predict geohazard response due to landslides, frost heave, or ground subsidence (Zheng et al., 2021a). Various assumptions must also be accounted for which unavoidably provide restrictions on the geohazard condition.

Contrary to analytical methods, numerical analysis of pipe subject to ground movement has been deemed as an effective tool for modelling and evaluation. The Finite Element Analysis (FEA) method has become globally accepted due to its capabilities for accurate simulation and modelling of pipelines under various conditions (TWI, 2019). FEA aims to simulate the physical phenomena, thereby reducing the need for physical prototypes (TWI, 2019). Several FEA models have been developed using general-purpose software Abaqus (Simulia, 2019) for strain demand analysis of pipelines subject to ground displacement and are considered the optimal numerical technique for pipeline response prediction. Hu et al. (2004) provided an effective equivalent-boundary method for the shell analysis of buried pipelines under fault movement using Abaqus. Trifonov et al. (2015) developed an FE model performing stress-strain analysis of buried steel pipes crossing active strike-slip faults, with an emphasis on fault modeling aspects. Xu et al. (2017) propelled this research studying buried pipelines subjected to reverse fault motion using vector form intrinsic FEM. These studies provide effective parametric analysis using FE models typically calibrated with experimental data. FE-based models tend to provide great variability and applicability in both the elastic and inelastic regimes, providing accurate results regardless of the pipe's behaviour (Zheng et al., 2021a).

Furthermore, finite element simulations have the capability of capturing the full mechanical system of an operating pipeline by including the effects of internal operating pressure and temperature variation. Typical models developed in Abaqus are constructed by PIPE32 elements (3-node quadratic pipe in space derived from Euler-Bernoulli beam elements) widely utilized in practice, capable of capturing internal pressure load and thermal effects. It was deemed that inclusion of temperature and pressure for pipes subject to ground motion can significantly affect the compressive strain at the top and bottom extreme fibres of the pipe's cross-section within the region of ground displacement (Allouche et al., 2022). Vertical deformation tends to increase depending on the magnitude of pressure and temperature change applied, while axial deformation significantly increases due to the nature of temperature and pressure loads, producing additional axial strains.

Although FEA is highly applicable, its use becomes a challenge due to limiting access to commercial software such as Abaqus, as well as the requirement for developing robust models. FEA models also require considerable computational power and are not typically geared for simulation of pipelines subject to ground-motion. Broad understanding of model parameters such as element type, pipe-soil interactions, boundary conditions, and method of analysis must be treated with caution. This makes FEA somewhat tedious for underground pipeline simulation. Consequently, there is a need for a predictive method that is straightforward and capable of capturing pipe response due to ground displacement accurately.

The method proposed by Zheng et al. (2021a) using the finite difference method (FDM) provides accurate results for buried steel pipes subject to ground displacement of varying magnitudes and directions. This method is implemented using powerful Python packages, where non-linear analysis is performed by solving the governing differential equations of the pipe interacting with soil (Zheng et al., 2021b) considering large deformation based on Euler-Bernoulli beam theory. Accounting for material nonlinearity in the pipe is non-trivial in the finite difference-based approach due to interaction or coupling between the axial and bending behaviour (Zheng et al., 2021b). The developed strain analysis considers inelastic material behaviour for different grades of steel pipe, as well as bi-linear force-displacement for soil-pipe interaction, accounting for soil plasticity (ALA, 2001). Based on the bilinear stress-strain relationship assumed for steel, the axial force and bending moment are derived respectively for segments without and with flexure deformation. This leads to axial force and bending moment expressions obtained as a function of the axial and lateral deformations. These expressions are then incorporated into the governing equations along with the equations modelling the pipeline soil interaction because of soil movements. Finally, longitudinal strains can be solved using the definition of the Green-Lagrangian strain, valid for large rotations and small strains. Once the equations have been established, they are discretized using finite difference, where the pipes strain response can be solved by iteration for all pipe segments within the entirety of the pipeline. This paper aims to extend the pipe strain demand assessment method previously developed by Zheng et al. (2021) to include effects of internal pressure and temperature changes of steel pipes buried in soils of various stiffnesses.

To further develop the model constructed by Zheng et al. (2021b) consideration of internal operating pressure and temperature variation can be incorporated into the governing equations, in specific the equations describing the axial force and bending moment response in the pipe. An analytical model of methods proposed by Yoosef-Ghodsi et al. (2008) discusses the inclusion of the effects of internal pressure and temperature change on the strain demand in the pipe due to longitudinal ground movement. The internal pressure results in a biaxial state of stress, where the secondary stress is defined as the circumferential hoop-stress. Therefore, a plasticity formulation is developed based on the equivalent yield criterion and isotropic strain hardening for the pipeline material. The temperature change is modelled as thermal strain dependant on the steel's thermal expansion value, defined as the change in temperature from normal pipe operation to the time when ground movement is initiated. These additional loads are considered in what is defined as an initial stress and initial pseudo strain, implemented into the governing equations describing the pipe's response in both the axial and bending directions. The initial strain due to temperature and pressure is considered as an axial strain component.

Utilizing the model developed by Yoosef-Ghodsi et al. (2008) to account for effects of pressure and temperature change in combination with formulation derived in this paper allows for direct association to the finite difference equations established by Zheng et. al (2021a). This allows for effective formulation, with applicability to virtually any scenario of ground displacement.

This analysis will enhance the method proposed by Zheng et al. (2021b) and provide more robust findings with more relation to fully operational pipes subject to ground movement. This paper is the first to incorporate a model that describes the effects of pressure and temperature in the nonlinear strain demand of pipe subject to ground displacement in both the longitudinal and axial directions.

2. MATERIALS AND METHODS

2.1 Governing Differential Equations

2.1.1 Pipe Subject to Ground Displacement

The method discussed in this paper considers the pipe's deformation response represented graphically in a horizontal (*x*-*y*) or vertical plane (*x*-*z* or *y*-*z*) as illustrated by Figure 1. The portion of pipeline being assessed can be considered as a straight segment, with the geohazard inducing a permanent ground deformation (PGD) with magnitude (δ) and ground intersection angle (β) within the geohazard zone. Examples of horizontal ground induced deformation include landslides or strike-slip seismic faults while vertical induced PGDs include uplifting forced triggered by frost heave or a vertical fault displacement.

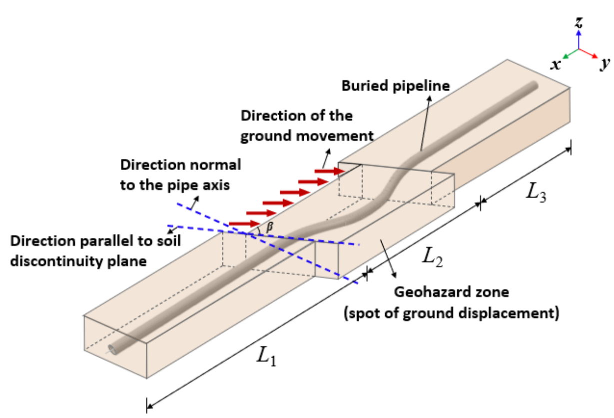

Figure 1: Schematic View of Pipe Subject to Ground Displacement

As discussed by Zheng et al. (2021a), the proposed method previously established considers the finite difference approach to solve the governing equations of pipeline (coupled nonlinear partial differential equations). Ultimately, the axial and flexural deformation fields along the pipe can be solved, utilized to further obtain the full pipe strain demand.

Consideration of pressure and temperature are expressed as internal pipe loads. These loads induce additional axial pipe strains, which can be included in the expression of longitudinal pipe strain developed due to ground movement.

2.1.2 Euler Bernoulli Beam Under Large Deformation

A pipeline subject to ground movement can be modelled as a Euler Bernoulli beam subject to distributed loads induced by soil with the assumption that plane cross-sections remain plane and perpendicular to the neutral axis before and after deformation (Figure 2). The governing equations can be expressed as coupled equations describing the beam deformation in the axial and transverse directions. The distributed loads applied to the pipe consider the exerted axial load density f and the lateral load density q. f depends on the difference between the axial displacement of the pipe $u(x)$ and the corresponding soil movement $U_g(x)$ along the pipe; q depends on the difference between the transverse (lateral or vertical depending on the direction of bending) displacement of the pipe $v(x)$ and the corresponding soil movement $V_g(x)$. The governing equations of the pipe considering large deformation are demonstrated by Eq. (1) as given by Zheng et al. (2021a).

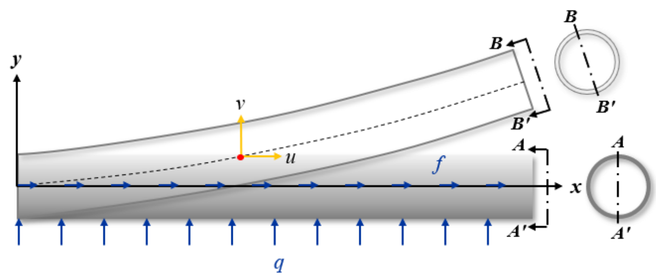

Figure 2: Euler Bernoulli beam under large deformation

$$\begin{cases} \dfrac{dN(x)}{dx} + f\left(U_g(x) - u(x)\right) = 0 \\ \dfrac{d^2M(x)}{dx^2} - \dfrac{d}{dx}\left(N(x)\dfrac{dv(x)}{dx}\right) - q\left(V_g(x) - v(x)\right) = 0 \end{cases} \quad (1)$$

$N(x)$ and $M(x)$ represent the internal axial force and bending moment in the pipe's cross section located at *x*, respectively.

The corresponding ground movement onto the pipe can be modelled by soil springs as recommended by ALA guidelines (ALA, 2001), accounting for crucial pipe-soil interaction properties characterized by a bilinear soil displacement response. These properties consider soil stiffness parameters, soil yield displacement, burial depth, and pipe geometry. The soil stiffness parameters are illustrated in Figure 3.

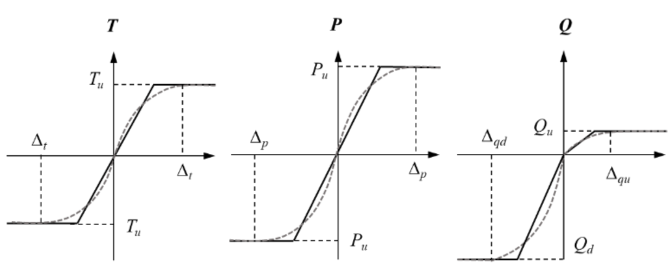

Figure 3: Soil Spring Properties in Each Direction (ALA, 2001)

From Figure 3:
T_u = Soil resistance in the axial direction.

Δt = Displacement in the axial direction.
P_u = Soil resistance in the lateral direction.
Δp = Displacement in the lateral direction.
Q_u = Soil resistance in bearing direction (vertical upward).
Δq_u = Displacement in bearing direction.
Q_d = Soil resistance in uplift direction (vertical downward).
Δq_d = Displacement in uplift direction.

This model can be utilized to develop the soil movement equations in Eq. (1), where the external distributed forces (f and q) can be represented by the soil spring properties in the axial and lateral/vertical direction. This can be expressed by equations developed by Zheng et al. (2021a) shown in Eq. (2) and Eq. (3), respectively.

$$f(u) = \begin{cases} T_u, & u > \Delta t \\ T_u/\Delta t.u, & -\Delta t \le u \le \Delta t \\ -T_u, & u < -\Delta t \end{cases} \tag{2}$$

$$q(v) = \begin{cases} P_u, & v > \Delta p \\ P/\Delta p.v, & -\Delta p \le v \le \Delta p \\ -P_u, & v < -\Delta p \end{cases} \tag{3}$$

The same formulation can be considered for soil resistance in the bearing and uplift direction, depending on the nature of the ground movement.

2.2 Pipe Material & Mechanical Model

2.2.1 Strain Due to Internal Pressure

Under the effect of bending alone, the pipe can be assumed to experience a uniaxial state of stress (Figure 4a). When internal pressure is applied, a hoop stress is generated in the circumferential direction, producing a biaxial state of stress as illustrated in Figure 4b.

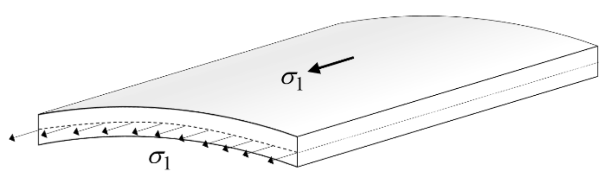

(a) Uniaxial

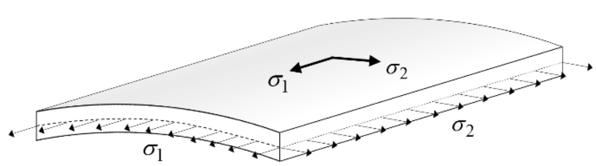

(b) Biaxial

Figure 4: Uniaxial and biaxial state of stress on pipe wall

σ_1 represents the longitudinal (axial) stress and σ_2 represents the circumferential (hoop) stress, respectively. This assumption is developed based on the plane stress criterion in curved surfaces.

Furthermore, the onset of yielding in the biaxial state of stress can be derived according to the Von Mises yield stress criterion, where the longitudinal and hoop stresses are equivalent to the principal stresses as demonstrated by Eq. (4). The hoop stress is determined based on the internal pressure (P), pipe wall thickness (t), and pipe outside diameter (D), which is assumed constant and expressed in Eq. (5). According to ASME B31.4/31.8 buried steel pipelines that are continually supported may be evaluated under the Von Mises failure criteria and can be adopted for this study.

$$\sigma_y^{VM} = \sqrt{\sigma_1^2 + \sigma_2^2 - \sigma_1\sigma_2} \tag{4}$$

$$\sigma_2 = \frac{P(D-2t)}{2t} \tag{5}$$

As developed by Yoosef-Ghodsi et al. (2008), an equivalent yield stress expression is implemented to account for the principal stresses, where the effective yield stress established increases or decreases (dependent on whether the steel is in tension or compression) from the initial value of uniaxial yield stress (σ_y) as the yielding of the material progresses (Yoosef-Ghodsi et al., 1994). Upon initiation of yielding, tensile and compressive axial stresses may be derived in each direction, denoted by σ_{1y}^T and σ_{1y}^C, respectively. These stresses are attained by solving Eq. (4) for σ_1 and are presented as Eq. (6). And Eq. (7), respectively.

$$\sigma_{1y}^T = \sigma_y^T = \frac{1}{2}\left(\sigma_2 + \sqrt{4\sigma_y^2 - 3\sigma_2^2}\right) > 0 \tag{6}$$

$$\sigma_{1y}^C = \sigma_y^C = \frac{1}{2}\left(\sigma_2 - \sqrt{4\sigma_y^2 - 3\sigma_2^2}\right) < 0 \tag{7}$$

Additionally, according to the plane stress condition, the equivalent yield strain in both the tensile and compressive state may also be derived according to the constitutive equations based on the Poisson's ratio (v) of the steel and young's modulus of elasticity, *E*. Akin to the stress expressions, the strain values obtained are denoted by ε_{1y}^T and ε_{1y}^C in Eq. (8) and (9), respectively.

$$\varepsilon_{1y}^T = \varepsilon_y^T = \frac{\sigma_{1y}^T}{E} - \frac{v\sigma_2}{E} > 0 \tag{8}$$

$$\varepsilon_{1y}^C = \varepsilon_y^C = \frac{\sigma_{1y}^C}{E} - \frac{v\sigma_2}{E} < 0 \tag{9}$$

It is important to note that $\sigma_y^T, \varepsilon_y^T$ and $\sigma_y^C, \varepsilon_y^C$ are inherently positive or negative as designated by the sign convention of tension or compression, respectively.

The equivalent yield strain expressions consider the effects of internal pressure and may be adopted in the expression of initial pseudo strain (ε_1^{init}) depending on the state of stress (Yoosef-Ghodsi et al., 2008). ε_1^{init} considers the effects of both temperature and pressure, where pressure tends to induce axial tension in the pipe and an increase in temperature tends to induce axial compression (Yoosef-Ghodsi et al., 2008).

2.2.2 Strain Due to Temperature Change

For this study, the temperature change ΔT refers to the change in temperature from the time of pipeline installment prior to operation, to when ground-movement is initiated. It is assumed that the temperature change is also constant during ground movement. The soil constraint also propels the assumption that no displacement or actual strain is considered when subject to internal pressure or temperature change without any ground displacement (Yoosef-Ghodsi et al., 2008).

The temperature change can be modelled according to the coefficient of thermal expansion α of the steel, where the thermal strain, $\varepsilon_1^{\Delta T}$ is expressed as Eq. (10).

$$\varepsilon_1^{\Delta T} = \alpha\Delta T \tag{10}$$

Finally, the initial pseudo strain ε_1^{init} can be adopted to include the effect of internal operating pressure and temperature change by incorporating the thermal strain with the strain developed by the hoop stress component according to Eq. (11).

$$\varepsilon_1^{init} = \frac{v\sigma_2}{E} - \alpha\Delta T \tag{11}$$

ε_1^{init} signifies the nonzero initial strain in the pipe prior to any ground movement due to internal pressure and temperature change. The initial strain value is then adopted into the expression of longitudinal strain induced by the ground movement simply by adding it to the derived axial and bending strain expressions developed by Zheng et al. (2021b).

2.2.3 Strain Due to Ground Movement

Building upon methods established by Zheng et al. (2021b), the expressions for the axial and bending strain are derived according to the strain and stress distribution on the pipe's cross-section. The axial strain ε_a is induced by axial elongation or compression of the pipe and the bending strain ε_b is induced under the flexural behavior (considered the normal strain caused by bending), accounting for both small and large deformations. These strains contribute to the longitudinal strain ε_l and are based upon the definition of Green-Lagrangian strain valid for large rotations and small strains. Therefore, ε_a and ε_b can be expressed in terms of the axial deformation *u*(*x*) and bending deformation *v*(*x*) induced by the ground displacement as defined in Eq. (1). ε_a and ε_b are demonstrated by Eq. (12) and Eq. (13), respectively.

$$\varepsilon_{axial} = \varepsilon_a = \frac{du(x)}{dx} + (\frac{dv(x)}{dx})^2 \tag{12}$$

$$\varepsilon_{bending} = \varepsilon_b = -\frac{d^2v(x)}{dx^2} \cdot z \tag{13}$$

where *z* represents the position along the axis of *z* as shown in Figure 5.

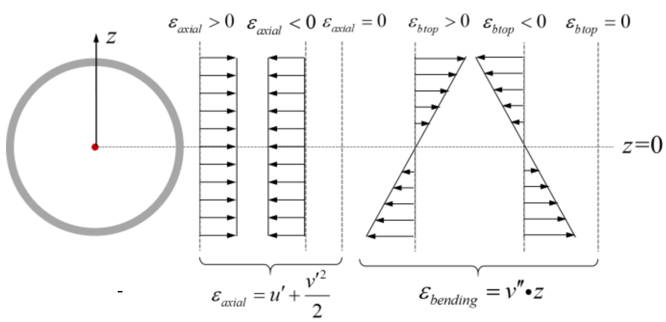

Figure 5: Axial strain and bending strain distribution on the pipe cross-section due to ground movement

The derived expression for the axial strain within the pipes cross-section can be further developed to include the axial initial pseudo strain (ε_1^{init}) previously established. This embodies the effects of axial deformation induced by ground motion, as well as pressure & temperature variation by adding the strains together, expressed by Eq. (14).

$$\varepsilon_a = \frac{du(x)}{dx} + (\frac{dv(x)}{dx})^2 + \varepsilon_1^{init} \tag{14}$$

Finally, based on the assumption that plane sections remain plane, the expression for the longitudinal strain can be achieved by summing the revised axial strain and bending strain to now account for pressure, temperature, and ground displacement, demonstrated according to Eq. (15).

$$\varepsilon_l = \varepsilon_a + \varepsilon_b = \left(\frac{du(x)}{dx} + \left(\frac{dv(x)}{dx}\right)^2 + \varepsilon_1^{init}\right) - \frac{d^2v(x)}{dx^2} \cdot z \tag{15}$$

The final expression described by Eq. (15) combines the method developed by Zheng et. al (2021b) describing the expression of longitudinal strain for pipes subject to ground deformation with the theory of initial pseudo strain hypothesized by Yoosef-Ghodsi et al. (2008) describing the effects of internal pressure and temperature change on pipes subject to ground deformation.

2.2.4 Tensile & Compressive Plastic Slopes

Based upon the nature of steel under a biaxial state of stress, the assumption of a uniaxial stress-strain relationship cannot be assumed, rather the strain hardening modulus E_p (plastic slope) must now account for a tensile and compressive state of stress (Yoosef-Ghodsi et al., 2008). The uniaxial and biaxial stress-strain relationship for a steel pipe is illustrated by Figure 5.

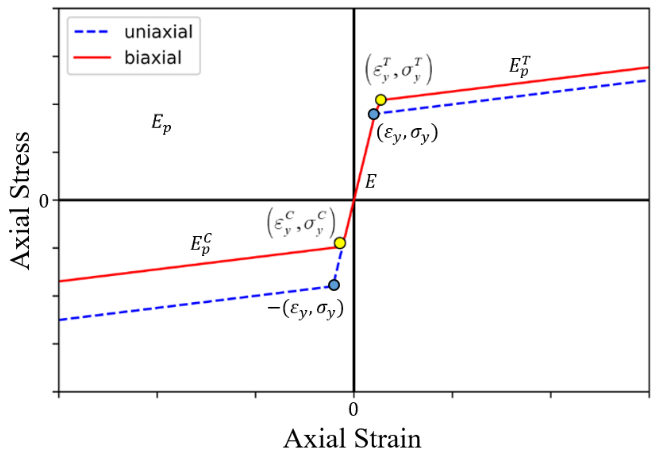

E_p

Figure 6: Uniaxial and biaxial stress-strain relationship for steel pipe

The uniaxial state of stress for the pipe material demonstrated by the blue dashed lines indicates that the yield stress (σ_y) and yield strain (ε_y) are equal in both the compressive (negative) and tensile (positive) directions. The material response of the steel is assumed to be a bilinear stress-strain response, where the elastic portion retains an elastic modulus of E, and the inelastic regions assume a constant strain hardening plastic modulus of E_p (indicated by the slopes of the blue dashed lines from Figure 6).

Contrary to a uniaxial stress state, the biaxial state of stress considers the influence of internal pressure, more specifically the hoop stress (σ_2). This response considers the equivalent yield stress and equivalent yield strain expressions established by Eq. (6) and Eq. (7), distinctive in both the tensile $(\varepsilon_y^T, \sigma_y^T)$ and compressive $(\varepsilon_y^C, \sigma_y^C)$ directions. It is observed in Figure 6 indicated by the red lines, a positive internal pressure decreases the compressive equivalent yield stress and increases the tensile equivalent yield stress, as expected due to the nature of hoop stress within the Von Mises yield criterion (Yoosef-Ghodsi et al., 2008).

The elastic portion of the biaxial response remains constant with an elastic modulus of E, while the plastic modulus in the inelastic portions of the graph carry distinct values indicated as E_P^T for the tensile direction, and E_P^C for the compressive direction, respectively (indicated by the slopes of the blue dashed lines from Figure 6). It is important to note that the response of the material after initiation of yielding is obtained using the flow (or incremental) theory of plasticity. The infinitesimal increment of axial stress during plastic deformation can be derived by solving for the expression of plastic strain and iterating through values of inelastic stress until the plastic modulus values are obtained (Yoosef-Ghodsi et al., 1994). The lines developed by the plastic portion of the bilinear red curve indicated in Figure 6 are nearly linear, thus can be assumed linear for simplicity to achieve a constant slope of E_P^T for the tensile direction, and E_P^C for the compressive direction.

Eq. (16) indicates the expression for the yield function ϕ, where σ_{vM} is equivalent to the von mises stress as expressed by Eq. (4).

$$\phi = \sigma_{vM} - \sigma_y \tag{16}$$

If the time derivative $\dot{\phi}$ of the yield function is set to zero, the material is assumed to be in the plastic state. From this, the plastic strain rate parameter $\dot{\bar{\varepsilon}}^p$ can be solved according to Eq. (17), and by the traditional von Mises associated flow rule, the plastic strain rate component in the first principal direction $\dot{\varepsilon}_1^p$ can be expressed by Eq. (18).

$$\dot{\bar{\varepsilon}}^p = \frac{1}{h}\frac{\partial\sigma_{vM}}{\partial\sigma_1}\dot{\sigma}_1 = \frac{2\sigma_1 - \sigma_2}{2h\sqrt{{\sigma_1}^2+{\sigma_2}^2-\sigma_1\sigma_2}}\dot{\sigma}_1 \qquad (17)$$

$$\dot{\varepsilon}_1^p = \dot{\bar{\varepsilon}}^p \frac{3S_1}{2\sigma_{vM}} = \frac{(2\sigma_1-\sigma_2)^2}{4h({\sigma_1}^2+{\sigma_2}^2-\sigma_1\sigma_2)}\dot{\sigma}_1 \qquad (18)$$

Where S_1 indicates the Deviatoric stress in the first principal direction.

The expression of the total strain rate $\dot{\varepsilon}_1$ can now be achieved by adding the elastic strain rate $\dot{\varepsilon}_1^e$ with the plastic strain rate $\dot{\varepsilon}_1^p$.

$$\dot{\varepsilon}_1 = \dot{\varepsilon}_1^e + \dot{\varepsilon}_1^p = \left(\frac{1}{E} + \frac{(2\sigma_1-\sigma_2)^2}{4h({\sigma_1}^2+{\sigma_2}^2-\sigma_1\sigma_2)}\right)\dot{\sigma}_1 \qquad (19)$$

where *h* can be expressed by Eq. (20).

$$h = \frac{EE_p}{E-E_p} \qquad (20)$$

Eqs. (19) and (20) developed by Yoosef-Ghodsi et al. (2008) were also employed in the study to consider the biaxial state of stress in the plastic state.

To calculate the plastic strain in both the tensile and compressive directions, Eq. (19) can be integrated in terms of the axial stress component (first principal stress), rendering Eq. (21) for the tensile state of strain $\varepsilon_1^{p,T}$ and Eq. (22) for the compressive state of strain $\varepsilon_1^{p,C}$, respectively.

$$\varepsilon_1^{p,T} = \varepsilon_{1y}^T + \frac{1}{E}\left(\sigma_1^{p,T} - \sigma_{1y}^T\right) + \frac{1}{4h}\int_{\sigma_{1y}^T}^{\sigma_1^{p,T}} \frac{(2\sigma_1-\sigma_2)^2}{({\sigma_1}^2+{\sigma_2}^2-\sigma_1\sigma_2)}d\sigma_1 \quad (21)$$

$$\varepsilon_1^{p,C} = \varepsilon_{1y}^C + \frac{1}{E}\left(\sigma_1^{p,C} - \sigma_{1y}^C\right) + \frac{1}{4h}\int_{\sigma_{1y}^C}^{\sigma_1^{p,C}} \frac{(2\sigma_1-\sigma_2)^2}{({\sigma_1}^2+{\sigma_2}^2-\sigma_1\sigma_2)}d\sigma_1 \quad (22)$$

where $\sigma_1^{p,T}$ denotes an inelastic state of stress in the tensile direction and $\sigma_1^{p,C}$ denotes an inelastic state of stress in the compressive direction, where:

$\sigma_1^{p,T} > \sigma_{1y}^T$ (Inelastic stresses larger than equivalent tensile yield stress).

$\sigma_1^{p,C} < \sigma_{1y}^C$ (Inelastic stresses less than equivalent compressive yield stress).

Utilizing Eqs. (21) and (22) by iterating at designated ranges of stresses from the inelastic tensile, elastic, and inelastic compressive zones allows the biaxial stress-strain relationship to be developed and plotted as illustrated by Figure 6.

Finally, the plastic slopes E_P^T and E_P^C can be developed as the slopes of the tensile and compressive axial-stress strain curves by assuming a linear response (Yoosef-Ghodsi et al., 1994). These expressions are provided by Eq. (23) and Eq. (24), respectively.

$$E_P^T = \frac{d\sigma_1^{p,T}}{d\varepsilon_1^{p,T}} = \frac{\Delta\sigma_1^{p,T}}{\Delta\varepsilon_1^{p,T}} \qquad (23)$$

$$E_P^C = \frac{d\sigma_1^{p,C}}{d\varepsilon_1^{p,C}} = \frac{\Delta\sigma_1^{p,C}}{\Delta\varepsilon_1^{p,C}} \qquad (24)$$

where $\Delta\varepsilon_1^{p,T}, \Delta\varepsilon_1^{p,C}$ represents the change in inelastic strain and $\Delta\sigma_1^{p,T}, \Delta\sigma_1^{p,C}$ represents the change in inelastic stress in the tensile and compressive directions, respectively.

Employing the theory of material plasticity allows for an accurate representation of the pipe material model under a biaxial state of stress.

2.3 Modified Axial Force & Bending Moment Equations

2.3.1 Bending Strain Excluded

This section aims to update the expressions of the axial force $N(x)$ and bending moment $M(x)$ equations previously established in the analysis performed by Zheng et al. (2021b). The revised equations have been modified to now include effects of temperature change and the biaxial material response due to the inclusion of internal pressure, which can be explicitly expressed as functions of $u(x)$ and $v(x)$ using the bilinear stress-strain relationship assumed for the pipe steel (Zheng et al., 2021b). As established in section 2.2 of this paper, the response of $N(x)$ and $M(x)$ can be modified to include the revised axial strain (Eq. (14)) and longitudinal strain response (Eq. (15)).

Furthermore, the expressions for the plastic slopes E_P^T and E_P^C can also be employed as a part of the $N(x)$ and $M(x)$ equations for capturing the inelastic material response and biaxial state of stress within the pipe in the compressive and tensile directions, respectively.

For the scenario when bending action does not exist ($v''(x) = 0$ and thus $M(x) = 0$ assuming no bending thermal strain), the stress and strain distributions on the pipe cross-section can be illustrated by the two cases as depicted in Figure 7 (Zheng et al., 2021b). This can also be derived by the red axial stress-axial strain curve shown in Figure 6. The stress-strain relationship is employed to formulate the constitutive expression described by Eq. (25), where the formulation of the internal axial force $N(x)$ can be derived as Eq. (26):

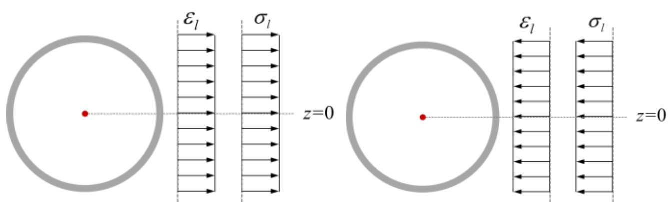

Figure 7: Longitudinal strain distribution without bending in the pipe cross-section

$$\sigma_l = \begin{cases} E_P^C\left(\varepsilon_l - \varepsilon_y^C\right) + \sigma_y^C\,, & \varepsilon_l < \varepsilon_y^C \\ E\varepsilon_l\,, & \varepsilon_y^C \le \varepsilon_l \le \varepsilon_y^T \\ E_P^T\left(\varepsilon_l - \varepsilon_y^T\right) + \sigma_y^T\,, & \varepsilon_l > \varepsilon_y^T \end{cases} \tag{25}$$

$$N(x) = \int_A \sigma_l dA = \begin{cases} \left(E_P^C\left(\varepsilon_l - \varepsilon_y^C\right) + \sigma_y^C\right)A\,, & \varepsilon_l < \varepsilon_y^C \\ E\varepsilon_l A\,, & \varepsilon_y^C \le \varepsilon_l \le \varepsilon_y^T \\ \left(E_P^T\left(\varepsilon_l - \varepsilon_y^T\right) + \sigma_y^T\right)A\,, & \varepsilon_l > \varepsilon_y^T \end{cases} \tag{26}$$

where A is the cross-sectional area of the pipe.

2.3.2 Bending Strain Included

The strain and stress distributions on the pipe cross-section with bending included can be generalized as two significant cases as depicted in Figure 8 (Zheng et al., 2021b). The two cases differ in terms of where the position of the tensile and compressive actions occur. Case (a) denotes the top section of the pipe being subject to tension and case (b) represents the top section of the pipe being subject to compression. In contrast to the derivation established by Zheng et. al (2021b), the longitudinal strain pattern within the pipe's cross section is now modified to include the equivalent yield strain in both the tensile and compressive zones, rather than the uniaxial yield strain due to the influence of pressure and temperature inducing a biaxial state of stress. The location of the equivalent yield strain within the distribution pattern relative to the neutral axis remains equivalent when compared to cases excluding effects of internal pressure or thermal strain (or a uniaxial state of stress). All potential patterns not depicted in Figure 8 are considered throughout the derivation within this section.

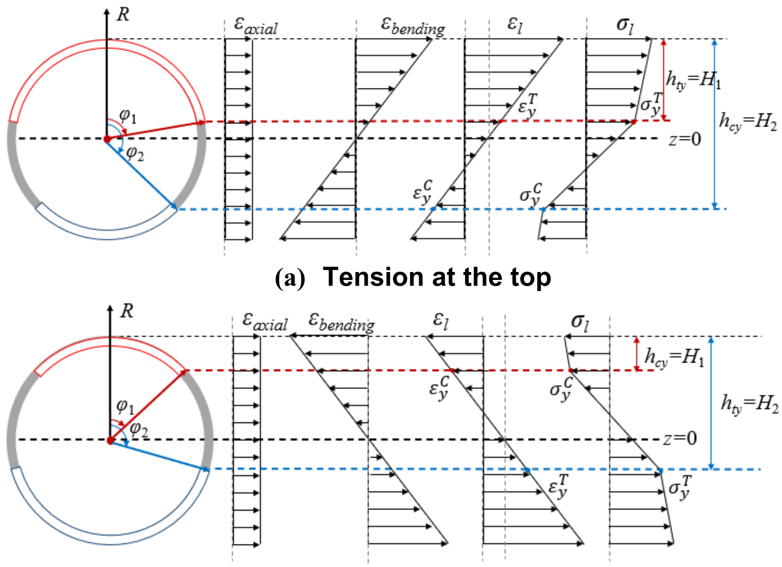

(a) Tension at the top

(b) Compression at the top

Figure 8: Longitudinal strain distribution with bending in the pipe cross-section

As defined by Zheng et al. (2021b), expressions describing the longitudinal strain on the pipe top ε_{top} and pipe bottom ε_{bot} can be derived from Eq (15). and expressed as Eqs. (27) and (28), respectively.

$$\varepsilon_{top} = \left(\frac{du(x)}{dx} + \left(\frac{dv(x)}{dx}\right)^2 + \varepsilon_1^{init}\right) - \frac{d^2v(x)}{dx^2} \cdot \left(\frac{D}{2}\right) \quad (27)$$

$$\varepsilon_{bot} = \left(\frac{du(x)}{dx} + \left(\frac{dv(x)}{dx}\right)^2 + \varepsilon_1^{init}\right) + \frac{d^2v(x)}{dx^2} \cdot \left(\frac{D}{2}\right) \quad (28)$$

where *D* represents the outer diameter of the pipe.

The positions of the yield points as depicted in Figure 8 are defined as the boundary between the elastic and plastic fields, where the vertical distance z from the pipe top to the tensile yield point h_{ty} and compressive yield point h_{cy} can be derived on the geometric basis defined by Eqs. (29) and (30) for Cases (a) and (b), respectively (Zheng et al., 2021b). The origin of the vertical coordinate is considered as the pipe center, with the positive side pointing in the upward direction.

$$h_{ty} = \frac{\varepsilon_{top}-\varepsilon_y^T}{\varepsilon_{top}-\varepsilon_{bot}} D = \frac{D}{2} - \frac{\varepsilon_y^T-\left(\frac{du(x)}{dx}+\left(\frac{dv(x)}{dx}\right)^2+\varepsilon_1^{init}\right)}{\frac{d^2v(x)}{dx^2}} \quad (29)$$

$$h_{cy} = \frac{\varepsilon_{top}+\varepsilon_y^C}{\varepsilon_{top}-\varepsilon_{bot}} D = \frac{D}{2} + \frac{\left(\frac{du(x)}{dx}+\left(\frac{dv(x)}{dx}\right)^2+\varepsilon_1^{init}\right)-\varepsilon_y^C}{\frac{d^2v(x)}{dx^2}} \quad (30)$$

The basis of the equations presented above have been modified to account for the equivalent yield points, which incapsulate the biaxial state of stress attributed to the hoop stress, as well as the initial pseudo strain ε_1^{init} established by Yoosef-Ghodsi et al. (2008) to account for the thermal strain and equivalent yield strain.

To distinguish the two conditions for the stress distributions shown in Figure 8, Zheng et al. (2021b) defined two auxiliary variables H_1 and H_2, which represent the lower and greater of h_{ty} and h_{cy}, respectively. These variables are introduced to facilitate the derivation of $N(x)$ and $M(x)$. The intersection angles attributed to h_{ty} and h_{cy} and defined as

φ_1 and φ_2 as shown in Figure 8 can be expressed according to Eq. (31). Due to the nature of the relationship between H_1 and H_2, φ_1 is less than φ_2, and captures all possible stress distribution patterns such as fully elastic and elastic-plastic. The definition of the intersection angles remains equivalent in this paper compared to the study established by Zheng et al. (2021b).

$$\varphi_i = \begin{cases} 0\,, & H_i \le 0 \\ \arccos\left(\frac{D-2H_i}{D}\right)\,, & 0 < H_i < D \quad (i = 1{,}2) \\ \pi\,, & H_i \ge D \end{cases} \tag{31}$$

To best account for the circular geometry of the pipes cross-section, the longitudinal strain ε_l (previously defined in rectangular coordinates) can be expressed in the cylindrical coordinate system and defined as ε_θ (Eq. (32)). The variation of strains in the radial direction can be neglected due to the thin-wall pipeline structure (Zheng et al., 2021).

$$\varepsilon_\theta = \left(u' + (v')^2 + \varepsilon_1^{init}\right) - v'' \cdot \left(\frac{D}{2}\right) \cdot cos\theta \tag{32}$$

where θ is the intersection angle between the axis of z and the position vector corresponding to the material fiber position, ranging from 0 to π (Zheng et al., 2021b).

Therefore, the stress distributions determined by the two scenarios presented in Figure 8 can now be established based on the bilinear property of the stress-strain relationship. due to the biaxial state of stress, the expressions for the stress distributions σ_θ must be separated into two cases: case (a) $h_{cy} > h_{ty}$ and case (b) $h_{cy} < h_{ty}$. This is based on the biaxial material response where the plastic slopes E_P^C and E_P^T must be considered, dependent on the direction of the plastic region developed in the pipe's cross-section (tensile or compressive).

Furthermore, based on the definition of the internal axial force and bending moment, the expressions of $N(x)$ and $M(x)$ are respectively derived for case (a) and case (b). The equations follow the same derivation developed in the study established by Zheng et al. (2021b), apart from the modified tensile and compressive plastic slopes, and modified strain distributions.

Case (a) $\boldsymbol{h_{cy} > h_{ty}}$:

$$\sigma_\theta = \begin{cases} \sigma_y^T + E_P^T\left(\varepsilon_\theta - \varepsilon_y^T\right), & 0 \le \theta \le \phi_1 \\ E\varepsilon_\theta, & \phi_1 \le \theta \le \phi_2 \\ \sigma_y^C + E_P^C\left(\varepsilon_\theta - \varepsilon_y^C\right), & \phi_2 \le \theta \le \pi \end{cases} \tag{33}$$

$$N(x) = 2\int_0^\pi \sigma_\theta \left(\frac{D-t}{2}\right) td\theta = (D-t)t \cdot \begin{pmatrix} (E_P^C\pi + (E - E_P^C)\phi_2)\varepsilon_a \\ -((E - E_P^T)sin\,\phi_1 - (E - E_P^C)sin\,\phi_2)\varepsilon_{bo} \\ -(E - E_P^T)\left(\varepsilon_a - \varepsilon_y^T\right)\phi_1 \\ +(E - E_P^C)(\pi - \phi_2)\varepsilon_y^C \end{pmatrix} \tag{34}$$

$$M(x) = 2\int_0^\pi \sigma_\theta \left(\frac{D-t}{2}\right)^2 tcos\theta d\theta = \frac{1}{4}(D-t)^2 t \cdot \begin{pmatrix} \left(E_P^C\pi + \begin{pmatrix} -(E - E_P^T)(\phi_1 + sin\,\phi_1\,cos\,\phi_1) \\ +(E - E_P^C)(\phi_2 + sin\phi_2\,cos\,\phi_2) \end{pmatrix}\right)\varepsilon_{bo} \\ -2\left((E - E_P^T)\,sin\,\phi_1 - (E - E_P^C)sin\,\phi_2\right)\varepsilon_a \\ +2\,sin\,\phi_1\,\varepsilon_y^T(E - E_P^T) - 2\,sin\,\phi_2\,\varepsilon_y^C(E - E_P^C) \end{pmatrix} \tag{35}$$

Case (b) $\mathbf{h_{cy} < h_{ty}}$:

$$\sigma_\theta = \begin{cases} \sigma_y^C + E_P^C(\varepsilon_\theta - \varepsilon_y^C), & 0 \le \theta \le \phi_1 \\ E\varepsilon_\theta, & \phi_1 \le \theta \le \phi_2 \\ \sigma_y^T + E_P^T(\varepsilon_\theta - \varepsilon_y^T), & \phi_2 \le \theta \le \pi \end{cases} \tag{36}$$

$$N(x) = 2\int_0^\pi \sigma_\theta\left(\frac{D-t}{2}\right)td\theta = (D-t)t \cdot \begin{pmatrix} (E_P^T\pi + (E - E_P^T)\phi_2)\varepsilon_a \\ -((E - E_P^C)sin\,\phi_1 - (E - E_P^T)sin\,\phi_2)\varepsilon_{bo} \\ -(E - E_P^C)(\varepsilon_a - \varepsilon_y^C)\phi_1 \\ +(E - E_P^T)(\pi - \phi_2)\varepsilon_y^T \end{pmatrix} \tag{37}$$

$$M(x) = 2\int_0^\pi \sigma_\theta\left(\frac{D-t}{2}\right)^2 tcos\theta d\theta = \frac{1}{4}(D-t)^2 t \cdot \begin{pmatrix} \left(E_P^T\pi + \begin{pmatrix} -(E - E_P^C)(\phi_1 + sin\,\phi_1\,cos\,\phi_1) \\ +(E - E_P^T)(\phi_2 + sin\phi_2\,cos\,\phi_2) \end{pmatrix}\right)\varepsilon_{bo} \\ -2\big((E - E_P^C)\,sin\,\phi_1 - (E - E_P^T)sin\,\phi_2\big)\varepsilon_a \\ +2\,sin\,\phi_1\,\varepsilon_y^C(E - E_P^C) - 2\,sin\,\phi_2\,\varepsilon_y^T(E - E_P^T) \end{pmatrix} \tag{38}$$

Where $\varepsilon_{bo} = -v''(x) \cdot \left(\frac{D}{2}\right)$, and represents the max bending strain based on Eq (13).

The modified internal axial force and bending moment equations now consider the contribution of the biaxial state of stress induced by the ground displacement and circumferential hoop stress, as well as the initial pseudo strain hypothesis established by Yoosef-Ghodsi et al. (2008). Eqs. (33) to (38) account for all distribution patterns in the elastic and plastic regimes for pipes subject to ground displacement in combination with internal operating pressure and temperature change as defined in this paper.

It is important to note that the equations for the axial force and bending moment are expressed as functions of $u(x)$ and $v(x)$ established by the definition of the max bending strain ε_{bo} and axial strain ε_a components. This allows for ease of implementation into the finite difference equations, where the axial and lateral deformation response can be acquired, ultimately utilized to obtain the longitudinal strain pattern throughout the entirety of the pipe.

2.4 Implementation to Finite Difference Equations

2.4.1 Finite Difference Notation

The schematic of the buried pipeline depicted in Figure 1 illustrates a straight pipe segment subject to ground displacement, with the length of the pipe within the geohazard zone (soil movement zone) defined as L_2. Outside the soil movement zone, L_1 represents the length of the pipe from the left fixed boundary condition to the ground motion initiation point, and L_3 represents the length of the pipe from the right fixed boundary condition to the ground motion end point.

The finite difference approach established by Zheng et al. (2021a) considers the governing equations for the interior grid points in segment L_2 to be modelled according to Eq. (39) based on the central finite difference method. Similarly, the finite difference equations for pipe segments L_1 and L_3 can be modelled by Eq. (40). The grid points are equally spaced in each segment in this study. λ is the internal distance of grid points, and the subscripts 1,2, and 3 indicated the corresponding pipe segment (Zheng et al., 2021b).

$$\begin{cases} \frac{1}{2\lambda_2}(N_{i+1} - N_{i-1}) + f(U - u_i) = 0 \\ \frac{1}{{\lambda_2}^2}\begin{bmatrix} (M_{i+1} - 2M_i + M_{i-1}) \\ -\frac{1}{4}(N_{i+1} - N_{i-1}) \cdot (v_{i+1} - v_{i-1}) \\ -N_i(v_{i+1} - 2v_i + v_{i-1}) \end{bmatrix} - q(V - v_i) = 0 \end{cases} \tag{39}$$

$$\begin{cases} \frac{1}{2\lambda_{1,3}}(N_{i+1} - N_{i-1}) + f(u_i) = 0 \\ \frac{1}{{\lambda_{1,3}}^2}\begin{bmatrix} (M_{i+1} - 2M_i + M_{i-1}) \\ -\frac{1}{4}(N_{i+1} - N_{i-1}) \cdot (v_{i+1} - v_{i-1}) \\ -N_i(v_{i+1} - 2v_i + v_{i-1}) \end{bmatrix} - q(v_i) = 0 \end{cases} \tag{40}$$

where i is the index denoting the ID of the grid point.

According to simulation studies performed in Abaqus by Agbo et. al (2022), a block ground displacement pattern is one of the most critical cases with respect to pipe strain and deformation. Therefore, the rectangular ground displacement pattern was implemented in this study. *U* and *V* are the magnitude of the axial and lateral component, respectively, of the ground movement in segment L_2 (Zheng et al., 2021a).

The schematic of the finite difference equations is unaffected by the inclusion of internal operating pressure or temperature variation, beneficial for ease of implementation.

2.4.2 Implementation Procedure

Implementation of the proposed method to obtain the unknown displacements at all grid points has been established by Zheng et al. (2021a) and can be repeated for the revised predictive method established in this paper. The proposed method was enhanced by implementing a solver which applies incremental loading rather than applying the entire ground displacement load simultaneously. The incremental solver allows for reliable convergence of a solution to the finite difference equations under cases of large deformation. The procedure as defined by Zheng et al. (2021) is elaborated by a series of steps, illustrated by Figure 9, and summarized as follows:

Step 1: meshing the pipe with equally spaced gird points along the axial direction for each pipe segment.

Step 2: Approximating the derivative terms using the finite difference equations according to Eqs. (39) and (40), based on the respective pipe segment.

Step 3: Calculating the internal axial forces and internal bending moments at the interior grid points by expressing $N(x)$ and $M(x)$ in the established finite difference notation.

Step 4: Constructing the governing equation for each interior grid point in each pipe segment (L_1, L_2, and L_3), where a symmetrical lateral soil resistance is assumed. Eqs. (2) and (3) defining the axial and lateral soil loads, respectively can be implemented

Step 5: Imposing boundary conditions for each grid point. The three pipe segments are consecutive, and both ends of the pipe are assumed fixed.

Step 6: Solving the simultaneous nonlinear equations using a nonlinear equation solver (Python script). When divergent solutions are obtained due to large ground deformation, incremental loading is employed in a series of steps, where the solution to the preceding applied load is used to obtain the solution for the following step, until the full load is applied, and convergence is achieved.

To solve the large system of nonlinear equations, the steps established above were implemented into a python programming package, defined by a set of several functions and sub functions. The unknown variables in the finite difference equations are solved sequentially using the Scipy optimize function (solving algorithm for nonlinear problems), where the solution of the expressions describing the pipe deformation are utilized to attain the longitudinal strain along the pipe according to Eq. (15). This procedure was established by Zheng et al. (2021a), where the maximum and minimum strain (referred to as the tensile and compressive strain demand) along the pipe and its corresponding location (critical locations) are obtained.

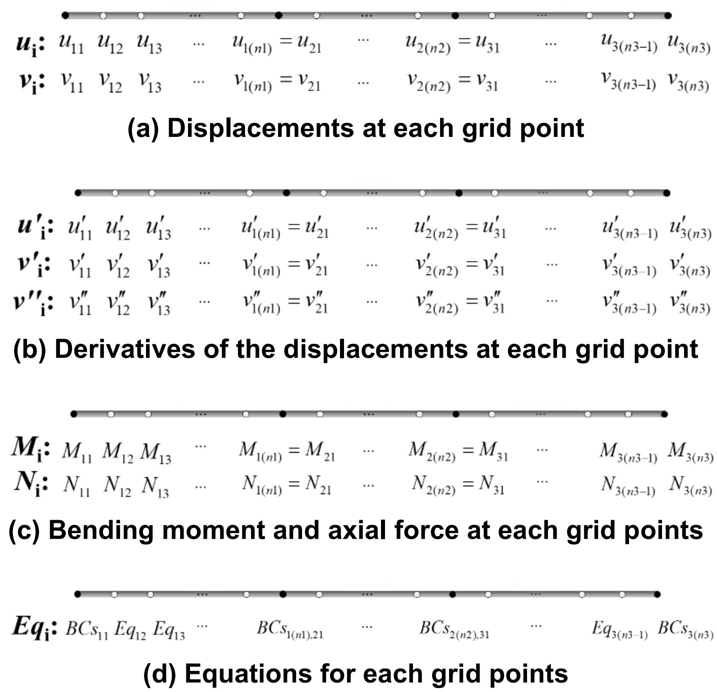

Figure 9: Schematic view for the calculation procedure of the proposed method by Zheng et al. (2021a)

In addition, the proposed method was implemented into an online cloud-based computational tool MecSimCalc. MecSimCalc provides a user-friendly interface, where model parameters pertaining to the pipe material, geometry, loading, pipe-soil interaction, and nodal structure can be implemented as inputs. The program is then run, generating the desired outputs as defined by the tool. The tool can be accessed by the link: https://mecsimcalc.com/app/6917733/pipeline_strain_demand_due_to_geohazard_with_p_t

3. RESULTS AND DISCUSSION

3.1 Case Studies: Pipe & Soil Parameters

Analogous to the study developed by Zheng et al. (2021a), the proposed method (PM) is validated against the finite element method implemented in Abaqus. Several hypothetical case studies are developed to demonstrate the accuracy of the proposed method with regards to pipeline axial and lateral deformation response, as well as the pipeline longitudinal strain pattern at the top and bottom extreme fibres of the pipe's cross-section. The finite element model established in Abaqus was employed in the study by Allouche et al. (2022) discussing the effect of pressure & temperature on pipe deformation during ground movement. The pipe-soil interaction is modelled according to ALA guidelines (2001), where non-linear soil springs are modelled using PSI36 elements (3-D 6-node pipe-soil interaction element) to develop the stiffness interaction between the pipe and soil in the axial, lateral, and bearing/uplift directions, respectively (as illustrated by Figure 3). The pipe is simulated by PIPE32 elements (3-node quadratic pipe in space), widely utilized in practice for preliminary design of pipes against geohazards (Zheng et al., 2021a). This model also accounts for material non-linearity, where plastic strains can be developed depending on the nature of the ground movement, and magnitude of internal pressure and/or temperature loading. A static analysis was performed to simulate a rectangular block ground motion, with the pressure & temperature loading applied sequentially. The model mesh considers equally spaced mesh size for the end pipe segments (L_1 and L_3), and a finer equally spaced mesh size for the middle pipe segment (L_2). The Abaqus model was also utilized as the benchmark finite element model in the study performed by Zheng et al. (2021b), adjusted here to include internal pressure & temperature change.

The model established by the proposed method considers the same number of nodes as in the Abaqus model, where the mesh of the pipeline considers the length of pipe element as 2 meters long in segments L_1 and L_3, and 1 meter

long in segment L_2. A finer mesh is considered for the geohazard zone, to allow for improved convergence and reliable model outcomes.
A theoretical straight pipeline (X65 pipe) was modelled with the following parameters

Pipeline Geometry:
D = 508 mm.
t = 7.14 mm.
L_1 = 100 m, L_2 = 10 m, L_3 = 100m (Pipe length, L = 210 m).
Burial depth: 1.8 m from the ground to the top of the pipe.

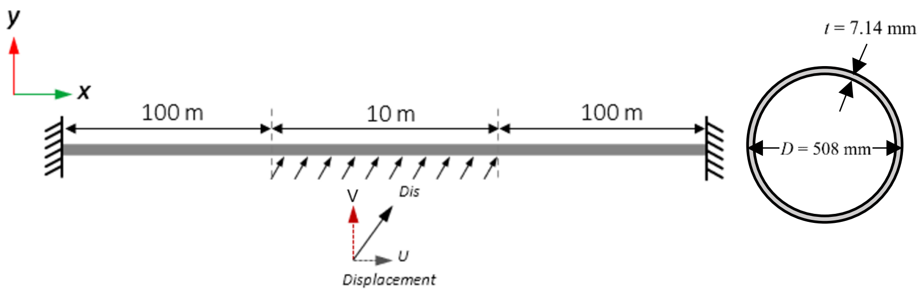

Figure 10: Simplified pipeline model

The pipe is loaded symmetrically (the transverse soil resistance at both sides of the pipe is the same), with the pipeline crossing a 10-meter geohazard zone across the mid-point location of the pipeline in the longitudinal direction. The geohazard zone induces ground motion according to the relative pipeline loading. The pipeline is assumed to have fixed-end boundary conditions.

The mesh of the pipeline includes 51 nodes for each of the 100 m spans between the supports and geohazard zone, while a finer mesh of 11 nodes was selected for the 10m span within the geohazard zone.

Pipe Material Properties & Loading:

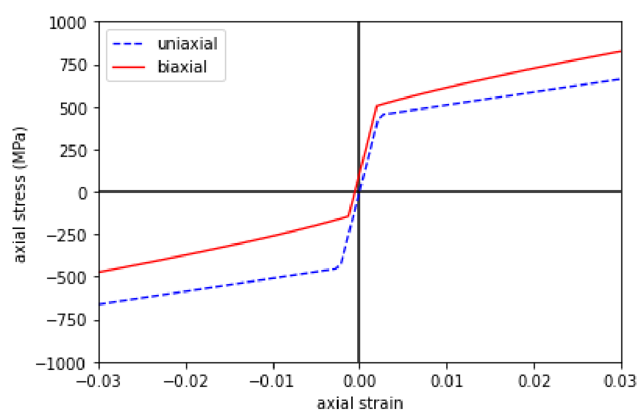

Figure 11: Uniaxial and biaxial bilinear stress-strain response for grade 448 steel

The uniaxial and biaxial stress-strain relationship for the steel employed in this study can be observed by the blue dashed-lines and red solid lines, respectively, in Figure 11. According to CSA Z662:19 standard, the allowable operating hoop stress is limited to 80% of the specified minimum yield stress (SMYS), applied prior to ground motion initiation. Therefore, an internal pressure of P = 10.26 MPa is applied according to Eq. (5). Additionally, a uniform temperature differential of ΔT = +60 ℃ is applied to the entirety of the steel pipe.

The material properties of the grade 448 steel based on the bilinear assumption are defined as follows:

$E = 199 \text{ GPa}$

$\nu = 0.3$ (Poisson's ratio)
$\propto = 12 \cdot 10^{-6} \frac{\text{m}}{\text{m°C}}$
$\sigma_y = 450 \text{ MPa}$
$\varepsilon_y = 0.00226 \frac{\text{mm}}{\text{mm}}$
$E_P = 7679 \text{ MPa}$

Biaxial material properties attributed to internal pressure (refer to Figure 6):

$\sigma_2 = 360 \text{ MPa}$
$\sigma_y^T = 505 \text{ MPa},\ \varepsilon_y^T = 0.00199 \frac{\text{mm}}{\text{mm}}$
$\sigma_y^C = -145 \text{ MPa},\ \varepsilon_y^C = -0.00127 \frac{\text{mm}}{\text{mm}}$
$E_P^T = 10147 \text{ MPa}$
$E_P^C = 9338 \text{ MPa}$

The pipeline is subject to a rectangular ground displacement δ at a ground intersection angle β based on the indicative case analyzed.

Soil Parameters:

According to the unified soils classification system (USCS) adopted by ASTM D-2487-98 (2017), soils may be classified and identified for general engineering purposes. A generalized categorization of soil strength denoted as weak, intermediate, and strong soil was adopted for this study dependant on the direct stiffness strength of the soil springs in the axial, lateral, and uplift/bearing directions as defined by ALA (2001).

Permitting to simulations conducted in the previous research by Allouche et al. (2022), the influence of additional pipe strain attributed to pressure and temperature is heavily dependant on the relative soil stiffness, where soil stiffness carries an inverse relationship to the added effects of pressure and temperature. Thus, evaluating the performance of the proposed method on multiple soil types carries importance when determining the accuracy and applicability of the developed method.

For this study, two soil types are considered, classified as Soil A and Soil B. Soil A is defined as a firm clay (intermediate strength), while Soil B is defined as a stiff clay (high strength). The strength is based on the relative stiffness in the direction of ground displacement. The soil parameters are classified according to Figure 3 (ALA, 2001) by Table 1.

Table 1: Soil properties for soil A and soil B

Parameter	**Soil A**	**Soil B**
Soil type	Firm Clay	Stiff Clay
T_u (kN/m)	14	27
Δt (mm)	5	8
P_u (kN/m)	40	109

Δp (mm)	46	32
Q_u (kN/m)	513	283
Δq_u (mm)	92	65

The soil types listed above are implemented in this study for various indicative analyses, where simulations with change in temperature & pressure loading, various ground displacement magnitude and ground intersection angles, and different geohazard lengths are considered.

3.2 Pressure, Temperature, Pressure & Temperature

To better observe the influence of pressure and/or temperature loading, four indicative loading scenarios were analyzed with the proposed method (PM), and compared with Abaqus as follows:

Case I: Ground motion with no pressure or temperature loading (P = 0 MPa, ΔT = 0 ℃).

Case II: Ground motion with a temperature loading of
ΔT = +60 ℃ and no pressure loading (P = 0 MPa).

Case III: Ground motion with a pressure load of P = 10.26 MPa and no temperature loading (ΔT = 0 ℃).

Case IV: Ground motion with both pressure and temperature loading (P = 10.26 MPa, ΔT = +60 ℃).

For all cases, an arbitrary magnitude of ground displacement δ of 500 mm was applied at a ground intersection angle of β = 90˚ (resembling a land slide perpendicular to the pipe), with the pipeline buried in Soil A. It was observed that cases analyzed at β = 90˚ presented the most critical pipe deformation response and strain demand when compared to other ground intersection angles (Allouche et al., 2022).

It is important to note that the equivalent tensile and compressive yield strains ($\varepsilon_y^T, \varepsilon_y^C$) and plastic slopes ($E_P^T, E_P^C$) associated to the biaxial state of stress are considered for Case 3 and 4, while the uniaxial material parameters are considered for Case 1 and 2. This section of the paper focuses on providing a comparative analysis directly associated to the influence of pressure and/or temperature.

Figures 14-17 illustrate the axial and lateral pipe deformation as well as the strain profile at the top and bottom extreme fibers of the pipes cross-section along the length of the pipeline for Cases I-IV, respectively. For all cases, the black solid curves represent the FEA response solved in Abaqus, while the red-dashed curves represent the response solved by the proposed method (referred to as PM). The critical locations of the pipe are defined as the locations along the pipeline where the most significant pipe strain and deformation occur, and can be observed in Figure 12, illustrating a deformed pipe subject to ground displacement.

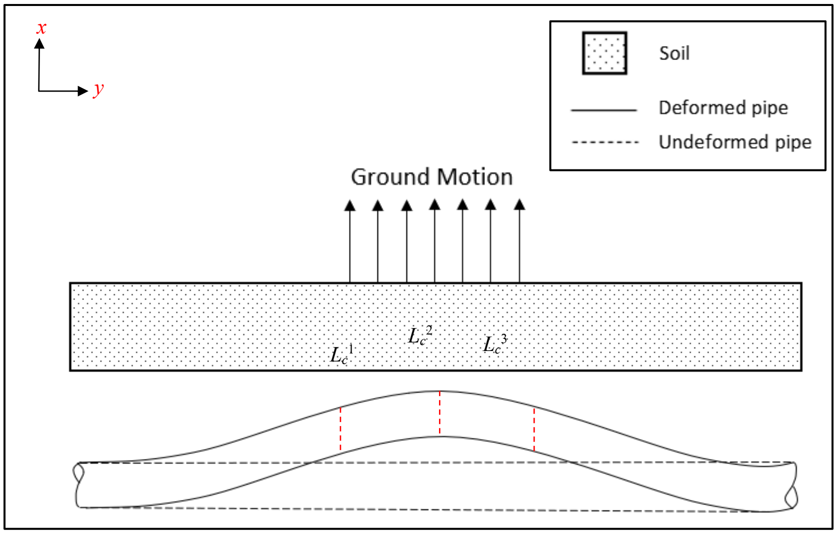

Figure 12: Representation of pipe deformation induced by ground deformation with critical locations

The maximum tensile and compressive longitudinal strain occurs at the top and bottom extreme fibers of the pipes cross-section (Figure 13), located at the center-span of the pipeline and near the end-zones of the ground displacement. These critical locations are identified in Figure 12 by the red dashed lines on the deformed pipe. L_c^1 represents the location along the pipe near where the ground motion is first initiated, L_c^2 represents the location at the center of the pipeline, and L_c^3 represents the location along the pipe near where the ground motion ends, with respect to the longitudinal direction. L_c^1 and L_c^3 are equal distances from the center of the pipeline when there is symmetry in geometry and loading.

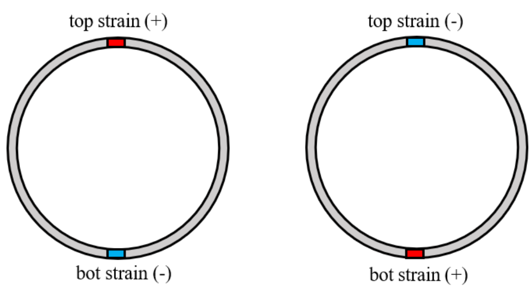

(a) Tension at top **(b) Compression at top**

Figure 13: Maximum strain locations in pipe's cross-section

Figures 14c/d to 17c/d illustrate the strain profile along the pipeline at the locations described by Figure 13 for Cases I-IV.

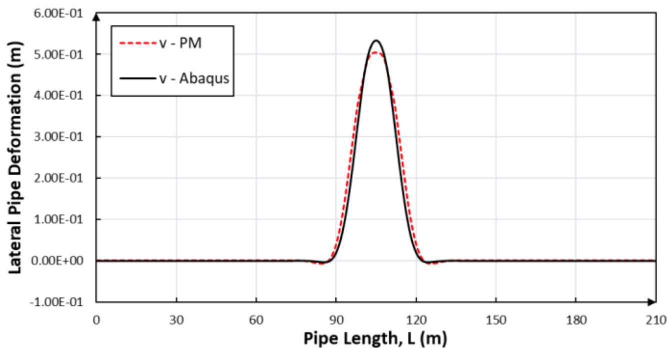

(a) Lateral pipe deformation

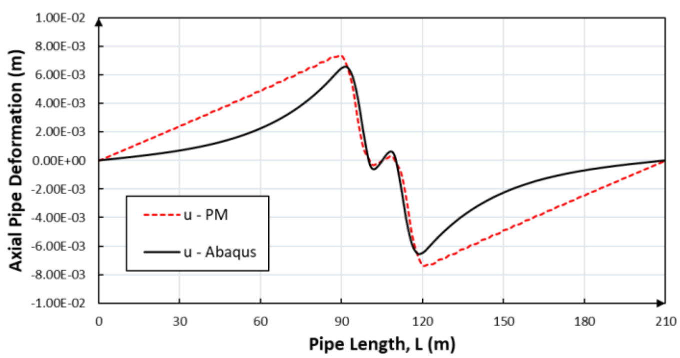

(b) Axial pipe deformation

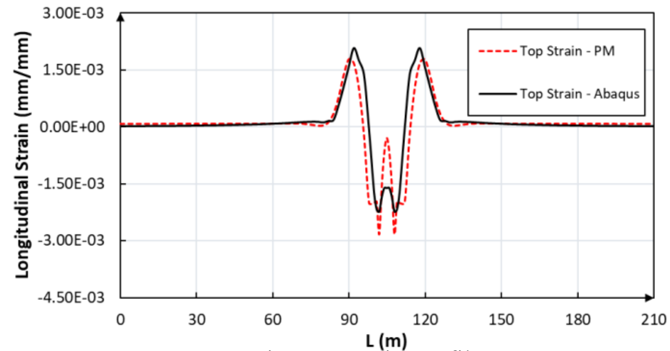

(c) Pipe top strain profile

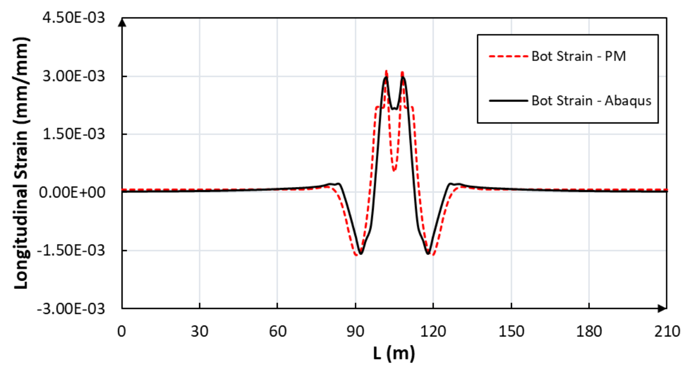

(d) Pipe bottom strain profile

Figure 14: Comparison of the proposed method and Abaqus in terms of pipe deformation and longitudinal strain response for Case I (δ = 500 mm, β = 90˚)

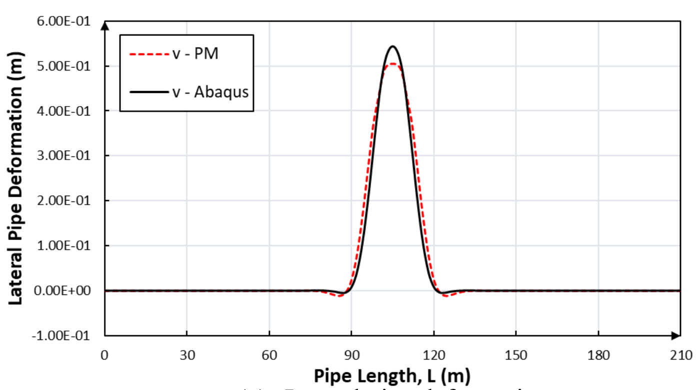

(a) Lateral pipe deformation

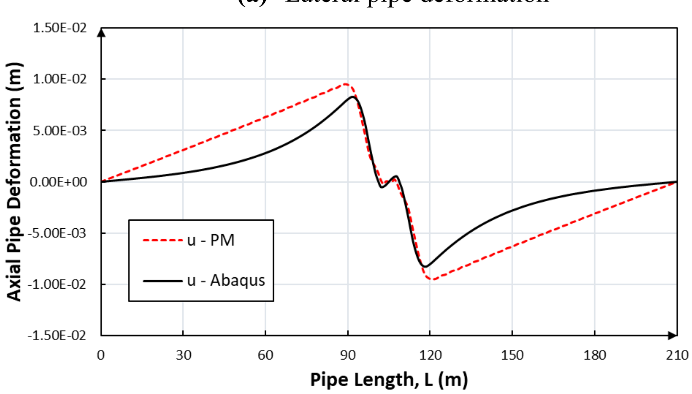

(b) Axial pipe deformation

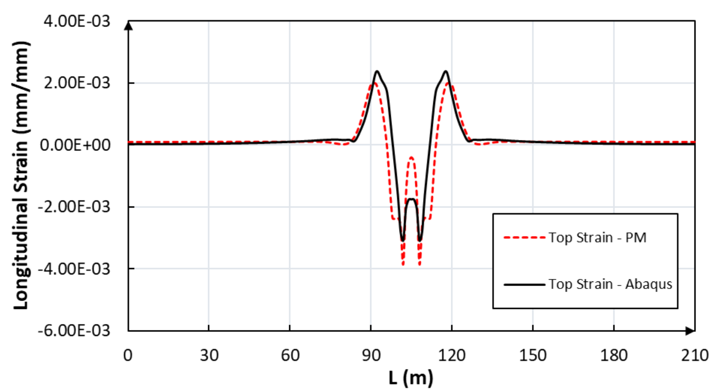

(c) Pipe top strain profile

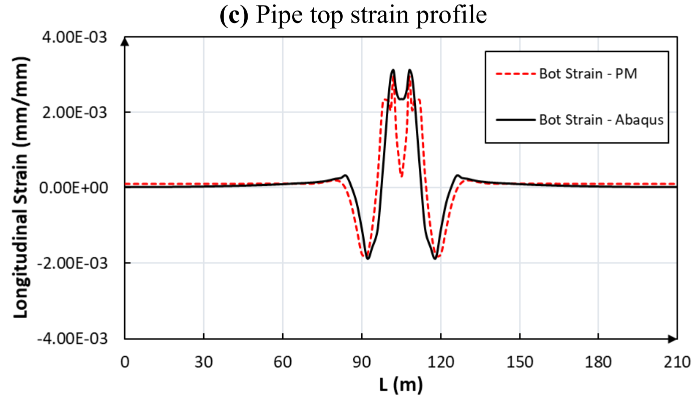

(d) Pipe bottom strain profile

Figure 15: Comparison of the proposed method and Abaqus in terms of pipe deformation and longitudinal strain response for Case II (δ = 500 mm, β = 90˚)

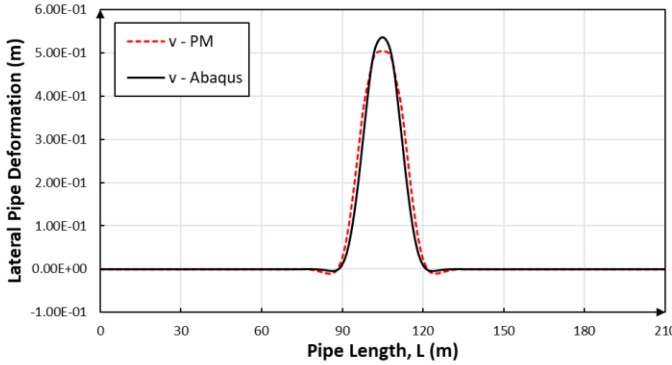

(a) Lateral pipe deformation

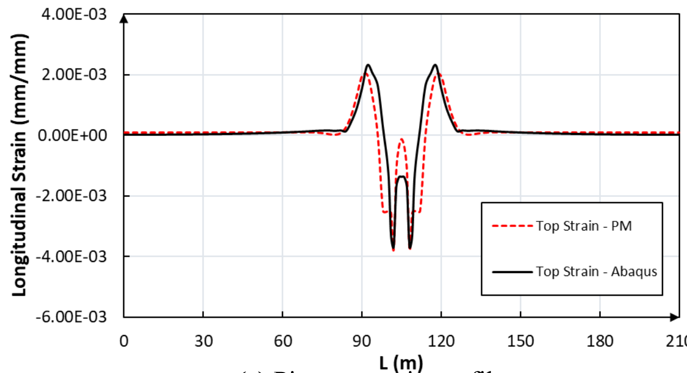

(c) Pipe top strain profile

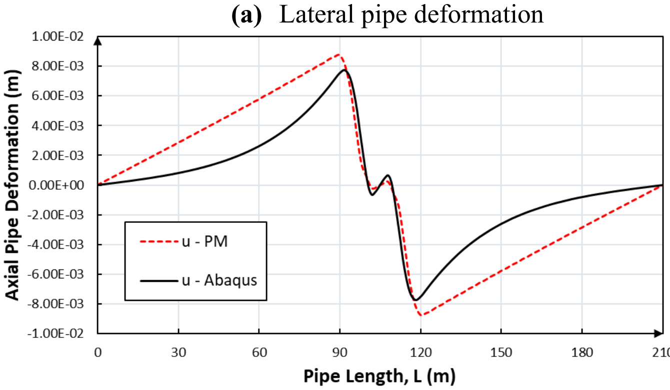

(b) Axial pipe deformation

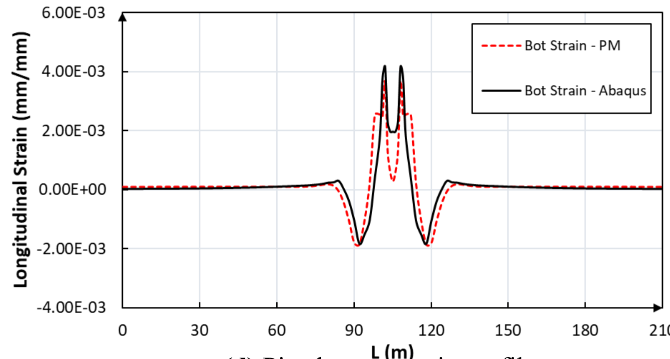

(d) Pipe bottom strain profile

Figure 16: Comparison of the proposed method and Abaqus in terms of pipe deformation and longitudinal strain response for Case III (δ = 500 mm, β = 90˚)

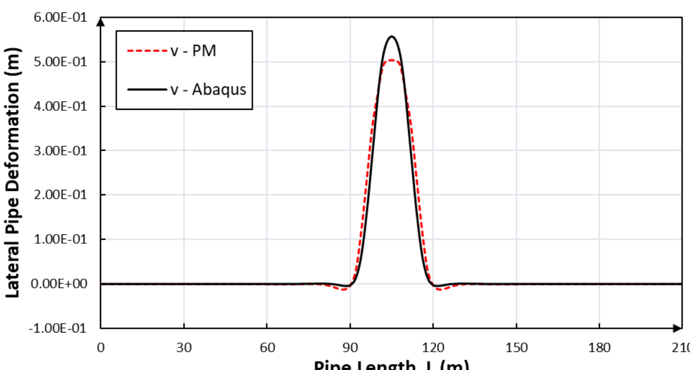

(a) Lateral pipe deformation

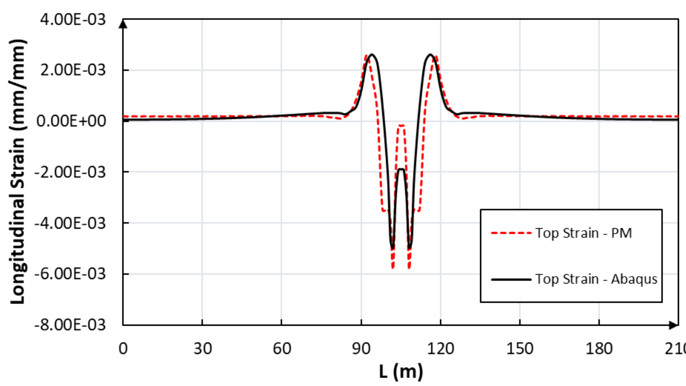

(c) Pipe top strain profile

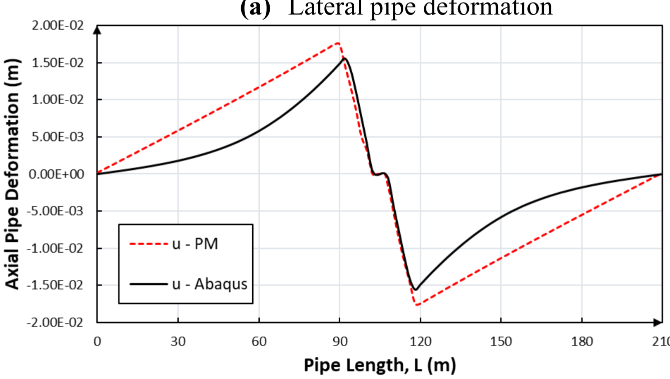

(b) Axial pipe deformation

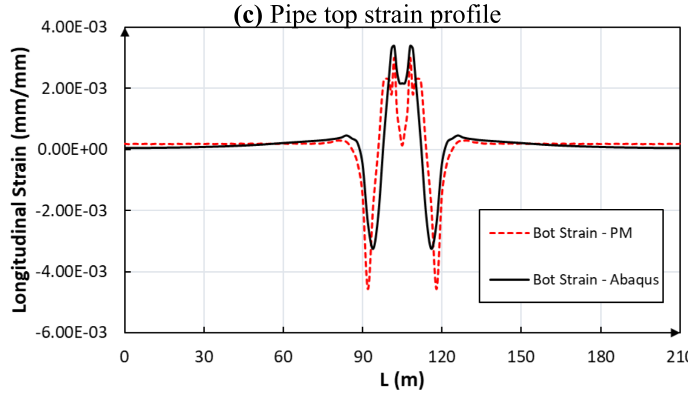

(d) Pipe bottom strain profile

Figure 17: Comparison of the proposed method and Abaqus in terms of pipe deformation and longitudinal strain response for Case IV (δ = 500 mm, β = 90˚)

From Figure 14-17, it is observed that the proposed method can accurately solve the pipe deformation response in the axial (u) and lateral (v) directions and capture the longitudinal strain response along the length of the pipeline at the top and bottom pipe locations for all four cases (referred to as top strain and bot strain, respectively). This can be deduced based on the comparison in the response between the PM and Abaqus (FEM). These results are significant as they provide validation of the proposed method for different load cases of internal operating pressure & temperature variation for pipes subject to ground deformation. For all simulation cases solved by the proposed method, it is observed that the lateral deformation response remains relatively similar among all cases, with the maximum lateral deformation remaining approximately equal to 0.504 m. Abaqus predicts a similar lateral deformation response (maximum deformation of 0.533 m), with additional predicted deformation for the case of temperature variation only (case II) as well as pressure and temperature variation (case IV). This is attributed to the firm lateral stiffness and relatively moderate yield displacements parameterized by the soil springs, where the soil carries significant loads compared to internal pipe loads in the lateral direction. Small negative deformation is apparent at the end-point critical locations (L_c^1 and L_c^3) due to the interaction of the soil resistance in accordance with the bending response.

The axial deformation response resembles an anti-symmetric curve, with the maximum deformation occurring at the end-point critical locations (L_c^1 and L_c^3). The inclusion of pressure and/or temperature does not impact the overall shape of the response obtained by the proposed method or Abaqus. The nature of the temperature and pressure loads implemented in the model are primarily axial. Therefore, the axial deformation response tends to moderately increase for case II and III, and dramatically increase for case IV with respect to case I. The longitudinal strain response illustrated by Figures 14-17 demonstrate significant inelastic strains, with greater strain demand occurring for the cases of temperature or pressure, and significant increase in strains for the case of pressure & temperature. The compressive strain demand is most impacted by the inclusion of pressure and temperature based on the additional negative stresses induced by the hoop stress, and increased strain rate credited to material plasticity. As a result, the compressive strain at the top and bottom of the pipe is slightly overpredicted by the proposed method compared to Abaqus as observed by Figures 14-17. This was also observed in the study performed by Yoosef-Ghodsi et al. (2008), assessing the impact of pipe strain demand under axial loading only.

Direct comparison of the results demonstrated in Figures 14-17 are summarized as bar graphs displayed by Figures 18 and 19. Figure 18 illustrates a summary of the maximum axial pipe deformation (u_{max}) and maximum lateral pipe deformation (v_{max}) along the length of the pipeline for cases I-IV, solved by the proposed method and Abaqus. To better illustrate the results of the axial deformation along with the vertical deformation on the same graph, it has been scaled by a factor of 10 (referred to as $10u_{max}$).

Figure 19 demonstrates the maximum of the compressive/tensile strain (taken as the absolute value) in the pipe, referred to as the strain demand for all cases. The maximum strain is most significant compared to the other strains predicted along the pipe, as it is the indicator for the state of the material under the specified loading and ground displacement. The green dashed line provides a reference for the yield displacement ($\varepsilon_y = 0.226\%$) of the steel.

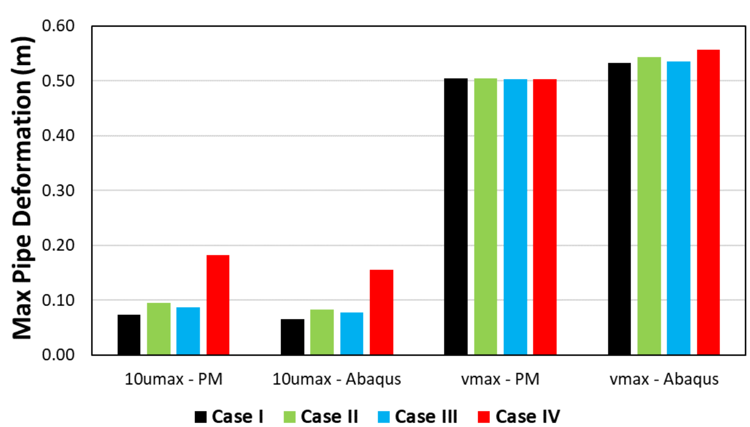

Figure 18: Maximum pipe deformation predicted by the PM and Abaqus for all cases

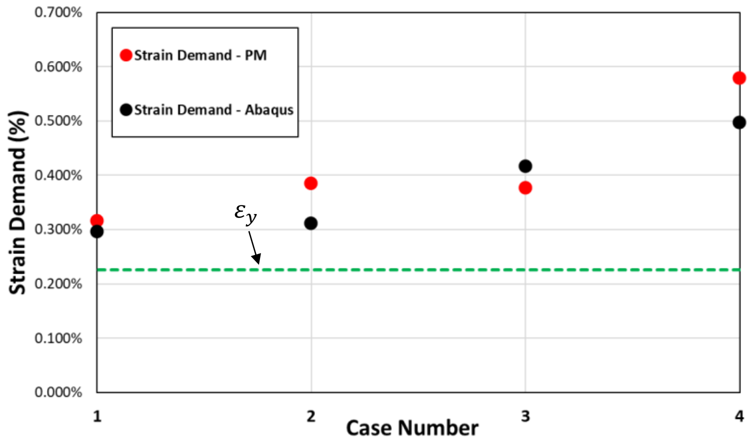

Figure 19: Strain demand predicted by the PM and Abaqus for all cases

Results of the proposed method compared to Abaqus from Figures 18 and 19 are summarized as follows:

Case I: Maximum lateral deformation and maximum axial deformation differ by 6.4% and 11.2%, respectively. Maximum strain demand differs by 6.4% (PM: 0.315% strain vs. Abaqus: 0.296% strain).

Case II: Maximum lateral deformation and maximum axial deformation differ by 5.7% and 12.8%, respectively. Maximum strain demand differs by 20% (PM: 0.385% strain vs. Abaqus: 0.311% strain).

Case III: Maximum lateral deformation and maximum axial deformation differ by 6.4% and 11.6%, respectively. Maximum strain demand differs by 9.6% (PM: 0.376% strain vs. Abaqus: 0.416% strain).

Case IV: Maximum lateral deformation and maximum axial deformation differ by 10.7% and 14.9%, respectively. Maximum strain demand differs by 16.5% (PM: 0.579% strain vs. Abaqus: 0.497% strain).

All cases indicate that the proposed method provides agreeable results when compared to Abaqus, suggesting that the inclusion of pressure and/or temperature in combination with ground movement considered in a plastic material state by the proposed method is correct and applicable.

Case IV is deemed the most critical analysis, as it captures the entire mechanical system of an operating pipeline subject to ground deformation, where internal operating pressure and temperature variations are apparent simultaneously. When comparing results from Case IV with Case I, the proposed method and Abaqus predicts the axial deformation response is expected to increase by up to 149% and 139%, respectively. Furthermore, the strain demand for the case of no pressure and temperature (Case I) compared to including both pressure and temperature (Case IV) is predicted to increase by up to 84% (PM) and 68% (Abaqus). These results further validate the solution provided by the proposed method as its results are considerably agreeable to the results obtained from complex finite element simulations in Abaqus. This further verifies the significant impact of including pressure and temperature loads during the ground displacement analysis, by accounting for additional pipe strains previously excluded by the original established model developed by Zheng et al. (2021b). The large difference in the strain demand and axial deformation between the aforementioned model and the proposed method is attributed to the impact of pressure and temperature on the pipe-soil interaction. Previous studies assessing the impact of pressure & temperature in the inelastic strain demand of pipes subject to ground displacement performed by Allouche et al. (2022) indicate that the pipe may experience a monotonic increase in strains dependent on the soil stiffness. It is observed that the pipe strains may not reach a plateau (soil yield-displacements are achieved, and thus no further deformation may occur), but rather tend to increase at larger ground displacements when compared to cases without pressure and/or temperature.

3.3 Varying Ground Displacement Magnitude & Ground Intersection Angle

To further validate the accuracy and reliability of the proposed method, analysis of the pipe subject to ground displacement at different ground intersection angles (angle between the pipe axis and the direction of the ground movement) are considered. Soil B is considered, and the pipe is assumed to operate with a pressure of P = 10.26 MPa and ΔT = +60 ℃, with the same material parameters and geometry as established in Section 3.1. The proposed method is once again validated against Abaqus, with observation of pipe deformation and strain demand at varying magnitudes of δ (from 0 up to 1 m). This analysis is conducted at different ground intersection angles β (0˚, 60˚, 90˚). For the most critical β = 90˚, additional analysis is executed to observe the performance of the proposed method at high strains (1-4%) and large δ (from 1 to 4m), where convergence of a solution can become difficult with many analytical and numerical models.

3.3.1 Ground Intersection Angle of 0 Degrees

Figures 20 through 23 present the pipe's strain demand and maximum displacement (axial and lateral) predicted using the proposed method (PM) and the finite element method (Abaqus). The maximum strain occurs at either of the critical locations defined by Figures 12 and 13, while the maximum deformation occurs at the center of the pipeline (midpoint of the segment within the geohazard). Figures 20-22 assess the maximum displacement and strain demand at different magnitudes of ground displacement (δ from 0 up to 1 m), as well as different ground intersection angles (β = 0˚, 60˚, 90˚). Figure 23 assesses the maximum displacement and strain demand at ground magnitudes of δ = 1 to 4 m, at a ground intersection angle of β = 90˚.

Figure 20 illustrates the response at β = 0˚ (direction of ground movement is parallel to the pipe in the longitudinal direction), where the pipe only withstands axial soil force. As observed from Figure 20a, the pipe deformation remains relatively small at all levels of ground displacement (< 5 mm). the maximum vertical deformation is 0 m due to only axial soil forces, while the maximum axial deformation predicted by Abaqus is slightly lower than the prediction solved by the proposed method. For both cases, the axial-soil force achieved yield displacement, where the soil plastifies and the pipe ceases to deform further (the pipe passes through the soil). Both cases also indicate a monotonic increase in pipe deformation as ground motion increases until soil yield is achieved. Abaqus predicts that the axial-soil yield displacement will occur around δ = 100 mm, where u_{max} = 1.7 mm for any further induced ground motion. The proposed method suggests that the axial-soil yield displacement occurs near δ = 400 mm, where u_{max} = 4.7 mm for any further induced ground motion. Because of the tiny displacements, the discrepancy is comparatively low, and the proposed method tends to capture the overall trend expected by the nature of this ground-motion when compared to Abaqus results.

From Figure 20b, the strain demand at the different intervals of ground motion is tiny and the pipe remains elastic. Both Abaqus and the proposed method indicate that the strains monotonically increase as ground movement increases and then plateau until axial-soil yield displacements are achieved. The extreme value (where strains plateau) of the tensile strain demand is 0.00605%, and the compressive strain demand is -0.00605%. Comparison with FEM-derived results demonstrate high accuracy of the proposed method.

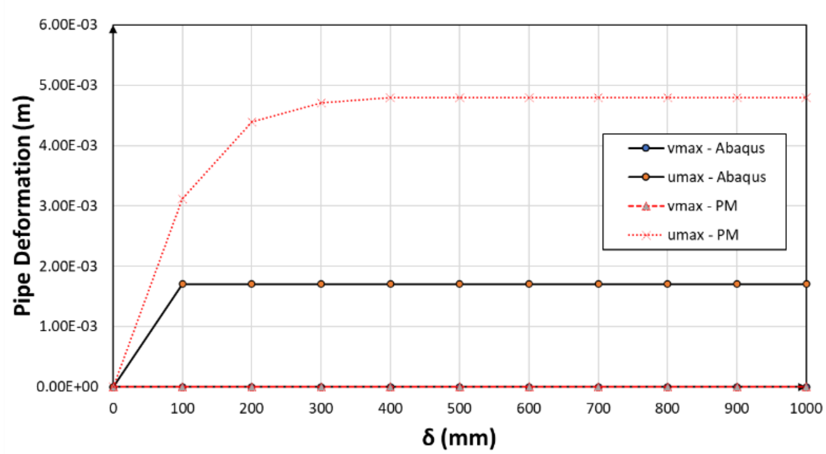

(a) Max displacement (β = 0˚)

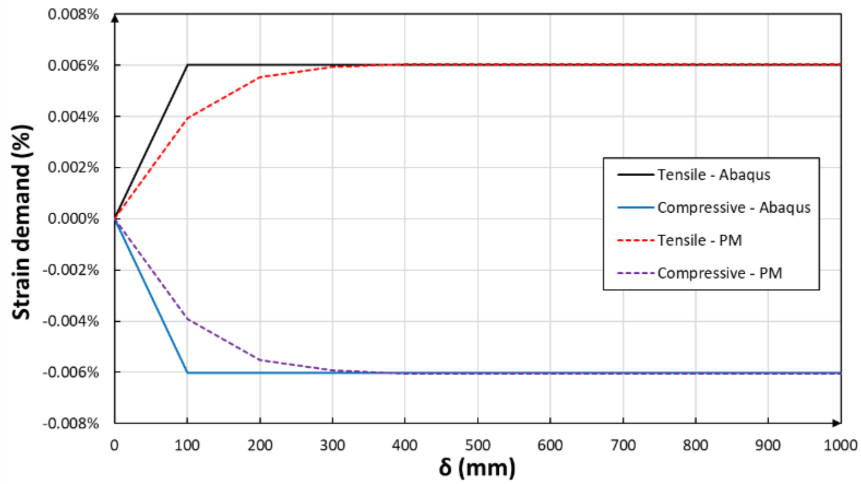

(b) Strain demand (β = 0˚)

Figure 20: Comparison between PM and Abaqus in terms of strain demand and maximum pipe deformation at different intervals of δ and β = 0˚

3.3.2 Ground Intersection Angle of 60 Degrees

Figure 21 illustrates the response at β = 60˚, where the pipe is under the combined effect of axial and lateral soil forces. At small ground movement, the pipe remains in the elastic range in which the strain demand is less than the yield strain ($\varepsilon_y = 0.226\%$, indicated by the green dashed lines). As the ground motion continues to develop, the pipe demonstrates elastic-plastic behavior, and the strain demand increases as expected. Figure 21a demonstrates high accuracy between the proposed method and Abaqus for both the axial and lateral deformation. Figure 21b indicates that the proposed method can predict the strain demand as ground displacement increases precisely with respect to Abaqus. This confirms that the proposed method accurately incorporates the effects of internal operating pressure and temperature change when the pipe is in an inelastic material state. Additionally, the accuracy of the proposed method is retained when compared to the previous proposed method established by Zheng et al. (2021b), which validates the finite difference solver with the inclusion of pressure and temperature effects employed in this study. For this ground displacement range, the strains tend to monotonically increase due to the relative axial and lateral soil-force displacements not yielding, allowing the pipe to further deform (the pipe remains intact with the soil, following the ground deformation). Because of the larger intersection angle, the lateral soil springs are more prominent than that of axial soil springs, since lateral soil springs impose greater force (Zheng et al., 2021b). The trend of the compressive strain demand predicted by the proposed method tends to have high accuracy when compared to Abaqus, while the tensile strain demand is slightly less. At δ = 1m, the tensile and compressive strain demand predicted by the proposed method and Abaqus are 1.52% & 1.74%, and -1.61% & -1.79%, respectively. This confirms the prediction capability of the proposed method, even for inelastic strains.

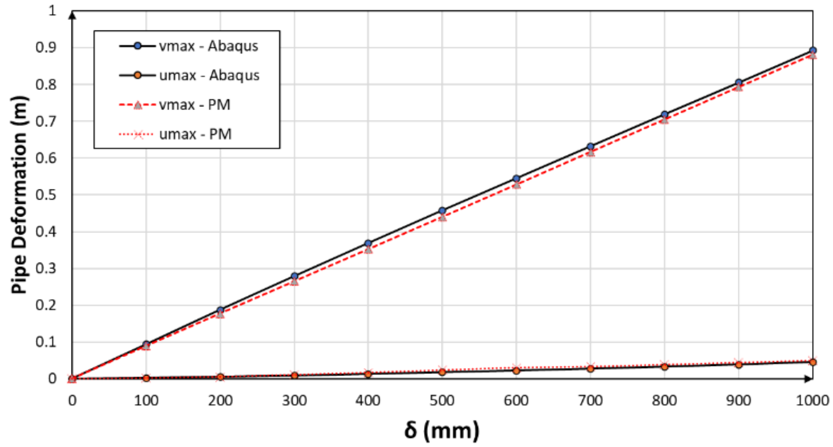

(a) Max displacement (β = 60˚)

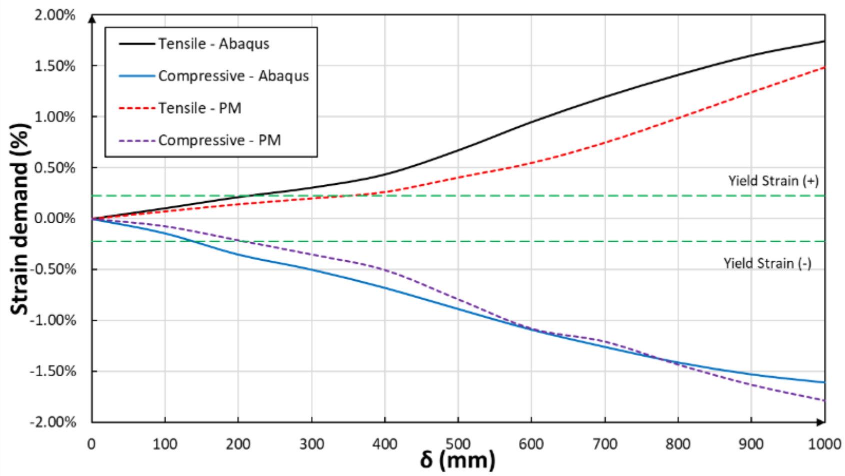

(b) Strain demand (β = 60˚)

Figure 21: Comparison between PM and Abaqus in terms of strain demand and maximum pipe deformation at different intervals of δ and β = 60˚

3.3.3 Ground Intersection Angle of 90 Degrees

Figure 22 illustrates the response at β = 90˚ (ground displacement perpendicular to the pipe), where the pipe is once again under the combined effect of axial and lateral soil forces. Comparable to Figure 21 at small ground movement, the pipe remains in the elastic range, and as the ground motion develops, the pipe demonstrates elastic-plastic behavior. The response observed is analogous to Figure 21, except for slightly higher strain and pipe deformation because of the sharp intersection angle providing larger influence of the lateral soil force component. Figure 21a demonstrates great accuracy between the proposed method and Abaqus for both the maximum axial and lateral pipe deformation. Figure 21b indicates that the tensile strain demand predicted by the proposed method is slightly more accurate at β = 90˚ compared to β = 60˚, while the compressive strain demand retains the same level of accuracy when compared to Abaqus (based on the similarity in the observed trend). This is likely credited to the ground motion being primarily lateral, where the tensile strain demand is greater impacted directly. This again confirms the validity of the proposed method derived from the analytical model established, which includes effects of pressure and temperature change in the elastic and plastic material state. At δ = 1m, the tensile and compressive strain demand predicted by the proposed method and Abaqus are 1.84% & 1.84%, and -1.98% & -1.68%, respectively.

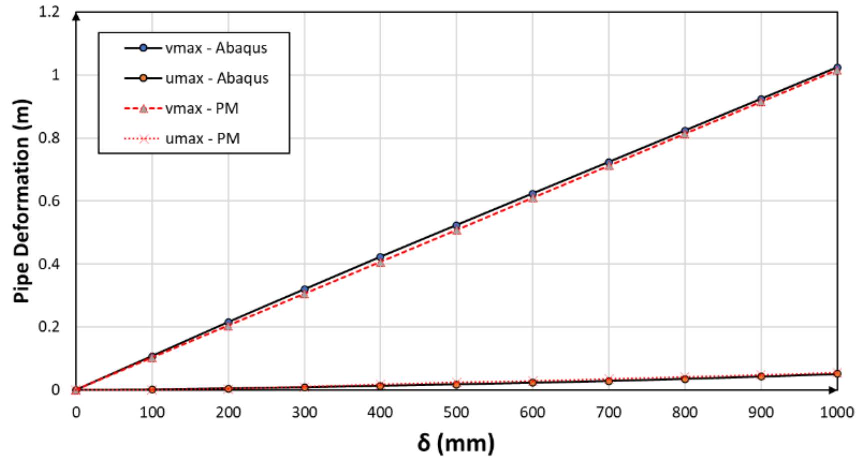

(a) Max displacement (β = 90˚)

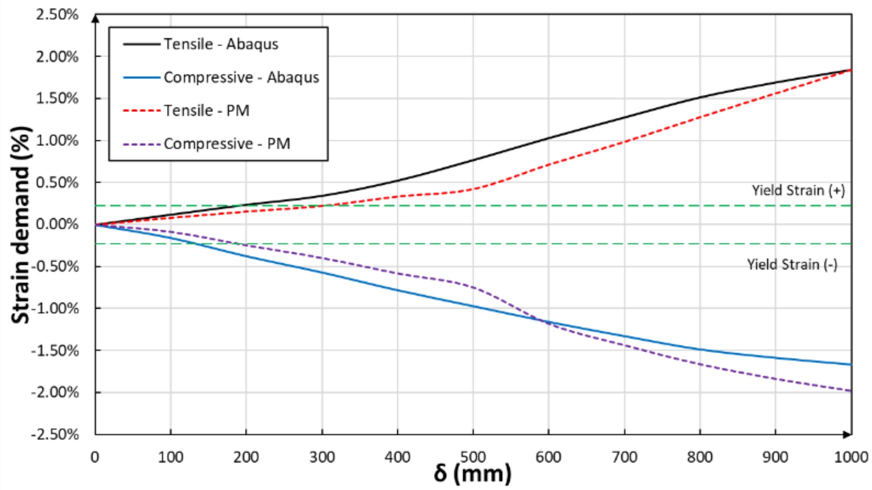

(b) Strain demand (β = 90˚)

(c)

Figure 22: Comparison between PM and Abaqus in terms of strain demand and maximum pipe deformation at different intervals of δ and β = 90˚

3.3.4 Large Strains and Ground Displacements (β = 90˚)

The proposed method is also employed to further observe the pipes response at large magnitudes of ground displacement where high strains are apparent. Analysis is conducted to assess the maximum displacement and strain demand at ground magnitudes of δ = 1 to 4 m, at a ground intersection angle of β = 90˚.

Figure 23a illustrates that the maximum axial and lateral pipe deformation predicted by the proposed method at large ground displacements (δ = 1 to 4 m) is relatively accurate when compared to Abaqus. For this case, the relative soil-force displacements plastify in the axial and lateral directions at approximately 4 m of ground movement (stiff soil tend to require large deformation for soil plastification). Thus, the pipe deformation increases monotonically from 1 to 3 m, and begins to plateau in both the axial/lateral directions as δ approaches 4 m. At soil yield, the proposed method predicts v_{max} = 3.33 m and u_{max} = 0.217 m, while Abaqus predicts v_{max} = 3.03 m and u_{max} = 0.233m. The results verify the capability of the proposed method at large ground displacement, with maximum allowable operating pressure and a specified temperature variation.

Furthermore, Figure 23b indicates the strain demand of the pipe at large intervals of δ. It is observed that the strains increase monotonically up to approximately 2 m of ground motion, until slightly decreasing as ground motion increases further, eventually plateauing as the relative soil-force displacements yield. Large inelastic strain is apparent due the large ground displacements, with the inclusion of pressure and temperature greatly influencing the strain demand observed. Results obtained from Abaqus and by the proposed method indicate that the maximum strain demand occurs as δ approaches 2m, and therefore is taken as the extreme occurrence of tensile/compressive strain demand. A governing strain plateau was employed on the proposed method to indicate the maximum strain value (indicated by the grey dashed lines) in both the tensile and compressive directions. Abaqus predicts that the maximum tensile and compressive strain demand of the pipe to be 2.80% and -1.70%, respectively. The proposed method indicates higher plastic strain where the tensile strain demand is predicted as 3.94% and the compressive strain demand is predicted as -2.09% (as indicated by the upper limit). This implies that the proposed method can be conservative when the pipe experiences high strains induced by ground deformation. The results between Abaqus and the proposed method are considerably agreeable, and discrepancies in the solution obtained are likely attributed to the level of sophistication of the solver employed to solve the highly nonlinear system of differential equations. As the ground motion becomes excessively large, the problem tends to become increasingly nonlinear. Results obtained by Figure 23 demonstrate the convergence capability of the proposed method at high levels of complexity attributed to large ground displacement while including effects of internal pressure and temperature change.

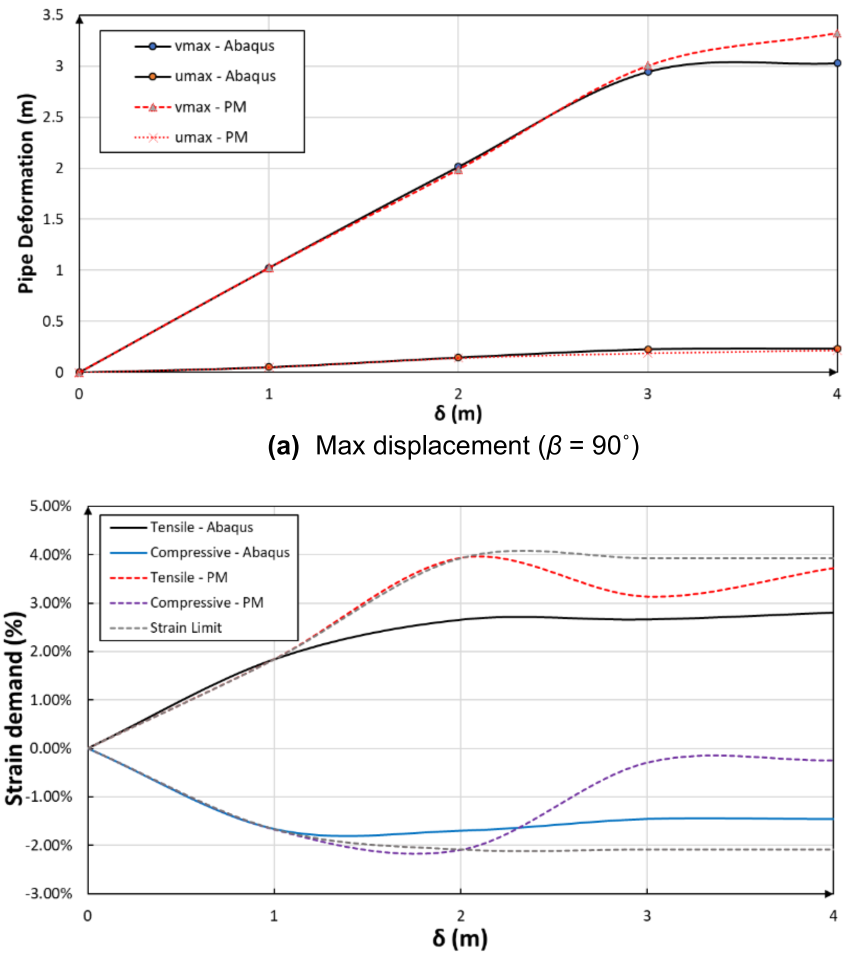

(a) Max displacement (β = 90˚)

(b) Strain demand (β = 90˚)

Figure 23: Comparison between PM and Abaqus in terms of strain demand and maximum pipe deformation for large strains at different intervals of δ and β = 90˚

3.4 Specified Pipeline Geohazard Case

To further verify the validity of the proposed method for pipes subject to ground displacement with internal pressure and temperature change, a specified case for unsymmetrical pipe geometry (with respect to the longitudinal direction) subject to a large geohazard zone can be considered.

Consider an X65 pipeline buried within a sloped (ground slope angle of 7˚ downwards) landscape, subject to high probability of landslide due to risk of earthquake or compromising slope stability. The pipeline is assumed to be buried in a stiff clay and therefore can be modelled according to Soil B. The pipeline considered spans a length of 446 m, with the left segment of the pipe L_1 = 100 m, the middle segment of the pipe (length of pipe subject to the geohazard) L_2 = 146 m, and the right segment of the pipe L_3 = 200 m. The pipeline crossing angle with respect to the ground displacement is β = 30˚. The idealization of the pipeline can be observed by Figure 24.

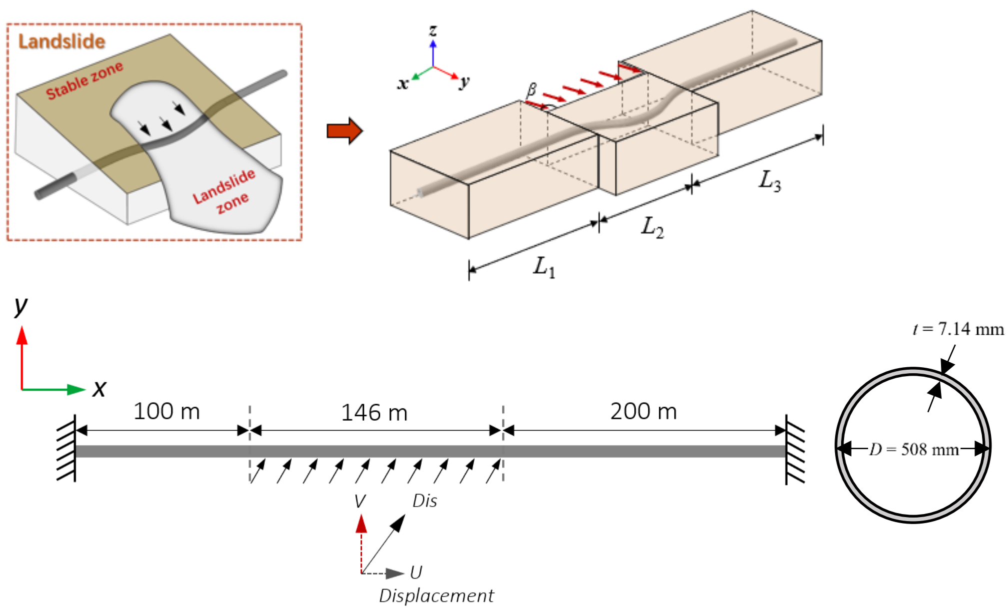

Figure 24: Idealization of pipeline subject to geohazard for specified case

The pipe size and material are modelled according to the parameters defined in Section 3.1, now with an internal operating pressure of P = 5.2 MPa and temperature change of ΔT = 30 ˚C. The material properties attributed to the biaxial state of stress in the steel under the given loading conditions are expressed below:

σ_2 = 180 MPa
$\sigma_y^T = 512\ MPa,\ \varepsilon_y^T = 0.00230\frac{\text{mm}}{\text{mm}}$
$\sigma_y^C = -332\ \text{MPa},\ \varepsilon_y^C = -0.00194\frac{\text{mm}}{\text{mm}}$
$E_P^T = 8133\ \text{MPa}$
$E_P^C = 8061\ \text{MPa}$

The pipeline is modelled according to the parameters defined above by the proposed method, and results regarding strain demand and pipe deformation are compared with Abaqus. The number of nodes considered for segment L_1, L_2 and L_3 are 51, 133, and 101, respectively for both the proposed method and Abaqus simulation.

The pipe is subject to varying intervals of ground displacement (from 0.1 to 1 m) to observe the strain demand with respect to increasing δ, as illustrated by Figure 25. It is determined that the pipe retains elasticity for small δ, while inelastic strains are developed for cases of δ larger than 400 mm and 200 mm in the tensile and compressive directions, respectively. The compressive strains initiate plasticity in the pipe based on the nature of the loading due to the direction of ground motion, and impact of temperature and pressure. Both the proposed method and Abaqus predict that the relative soil-force displacements do not yield for this range of ground motion, and the pipe strains continue to increase monotonically. It is observed that the proposed method aligns with the trend calculated by Abaqus in both the tensile and compressive directions. For this case of large geohazard length, the values of strain demand predicted by the proposed method are closer to Abaqus at lower intervals of δ compared to larger δ. At δ = 1m, the tensile strain demand calculated by Abaqus, and the proposed method is 0.97% and 0.60%, respectively. The compressive strain demand calculated by Abaqus, and the proposed method is -1.51% and -0.90%, respectively.

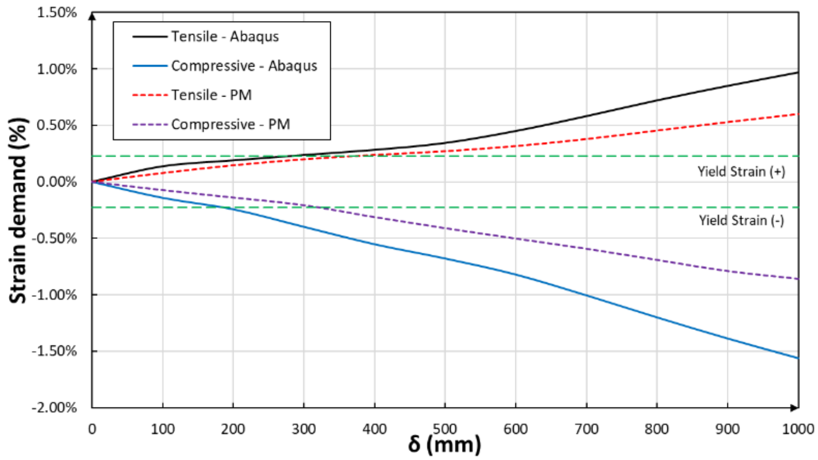

Figure 25: Comparison between PM and Abaqus in terms of strain demand and maximum pipe deformation for specified geohazard at different intervals of δ

Figure 26 illustrates the pipe deformation response and longitudinal strain pattern at the top and bottom extreme fibers along the length of the pipeline at a ground motion of 1 m. As observed by Figure 26a, the vertical deformation response (v) predicted by the proposed method aligns well with the Abaqus prediction (less than 1% disparity). The moving block shape is a result of the large geohazard span associated to the ground displacement. The axial displacement response (u) developed by the proposed method also aligns well with the Abaqus prediction, indicating that the proposed method including pressure and temperature change can accurately simulate the pipeline deformation response for large spans of pipe and geohazards.

Figure 26b demonstrates that the longitudinal strain pattern at the top and bottom locations of the pipe is well predicted by the proposed method when compared to Abaqus. For this case, consideration of a large ground displacement width demonstrates concentration of high strains, localized at the geohazard end-point critical locations (L_c^1 and L_c^3), with compressive strain demand predicted at L_c^3 and tensile strain demand at L_c^1. The proposed method also precisely predicts the location of the compressive and tensile strain demand, where development of inelastic strains attributed to the combined loading of pressure, temperature, and ground displacement is appropriately accounted for.

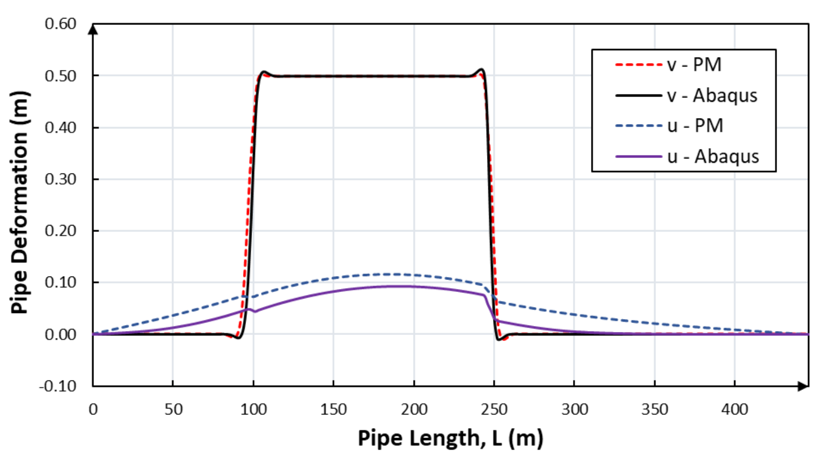

(a) Pipe deformation response (δ = 1 m, β = 30˚)

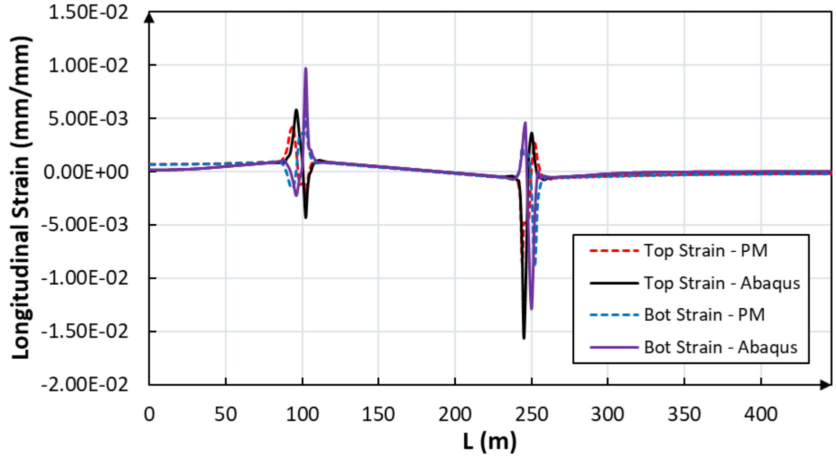

(b) Pipe longitudinal strain (δ = 1 m, β = 30˚)

Figure 26: Comparison of the proposed method and Abaqus in terms of pipe deformation and longitudinal strain response for specified geohazard

4. CONCLUSION

Pipelines travel vast distances, where risk of permanent ground movements induced by geohazards is apparent. The structural integrity of the pipe is greatly attributed to strains induced by such geohazards, where additional strains may be evident due to internal operating pressure and temperature change within the pipe. Methods established by Zheng et al. (2021b) developed to predict steel pipe deformation and strain response are extended to include the effects of internal operating pressure and temperature change, capturing the full mechanical system of an operating pipeline. This considers the pipe to be in the biaxial state of stress, induced by circumferential hoop stress due to pressure. As a result, the initial pseudo-strain hypothesis developed by Yoosef-Ghodsi et al. (2008) which incapsulates the effects of temperature and pressure on the nonlinear strain demand of pipes can be incorporated into the internal axial force and bending moment equations. These equations are explicitly derived as functions of the lateral and axial deformation expressions for pipes under flexural and axial forces, where the longitudinal strain components can be acquired based on the governing equations, and law of continuity. The pipe's stress and strain profile are also adjusted to include the effects of pressure and/or temperature variation in both the tensile and compressive directions. Furthermore, the proposed method developed by Zheng et al. (2021b) describing the finite difference equations was directly enhanced by implementing an incremental solver with respect to magnitude of the applied ground displacement to retain convergence where required. It was also determined that considering the influence of pressure and temperature did not alter the scheme for solving the explicit functions at each node, beneficial for ease of implementation.

Four indicative cases pertaining to pipe load with varying combinations of internal pressure and temperature was analyzed to verify the validity of the proposed method against finite element method (Abaqus). The comparison with the finite element results has demonstrated that the proposed method has a great predictive capability for pipe strain demand and displacement response, retaining the level of accuracy of the original model developed by Zheng et al. (2021b). It was determined that the inclusion of pressure and/or temperature compared to analyses excluding these loads predict larger inelastic strains in both directions, and a notable increase in axial pipe deformation. The proposed method was also utilized to predict the strain response at increasing increments of ground movement (δ = 100 to 1000 mm), and different ground intersection angles (β = 0˚, 60˚, 90˚). It was observed that the proposed method accurately incorporates the effects of internal operating pressure and temperature change when the pipe is in an elastic and inelastic material state. Performance of the model was also evaluated at large increments of ground movement (δ = 1 m to 4 m) for the critical case of β = 90˚, validating the model's predictive capability for excessively high strains. A large segment of pipe (L = 446 m) was also assessed, where a pipeline subject to a large unsymmetric landslide (L_2 = 146 m, β = 30˚) was analyzed for the deformation response and strain demand. It is demonstrated that the proposed method accurately determines the material response of the pipe when compared to Abaqus, appropriately predicting the location of the compressive and tensile strain demand, as well as the elastic-plastic state of the pipe at magnitudes of δ between 0 and 1000 mm. This confirms the broad application of the proposed method with respect to varying types of geohazards, magnitudes of operating pressure, and temperature change. This enhanced method offers an alternative analysis approach to be used in preliminary design, safety pre-screening, or reliability-based assessment of pipes buried through geohazard zones. The added effects of internal operating pressure and temperature change also provide greater relatability to real world pipe operation.

ACKNOWLEDGEMENTS

This work is supported by MITACS and the Natural Sciences and Engineering Council of Canada (NSERC).

DISCLAIMER

Any information or data pertaining to Enbridge Liquids Pipelines or its affiliates, contained in this paper was provided to the authors with the express permission of Enbridge Liquids Pipelines, or its affiliates. However, this paper is the work and opinion of the authors and is not to be interpreted as Enbridge Liquids Pipelines, or its affiliates', position or procedure regarding matters referred to in this paper. Enbridge Liquids Pipelines and its affiliates and their respective employees, officers, director, and agents shall not be liable for any claims for loss, damage, or costs, of any kind whatsoever, arising from the errors, inaccuracies or incompleteness of the information and data contained in this paper or for any loss, damage or costs that may arise from the use or interpretation of this paper.

REFERENCES

[1] Zheng, Q., Graf-Alexiou, G., Li, Y., Yoosef-Ghodsi, N., Fowler, M., Kainat, M., Adeeb, S., Strain demand of elastic pipes subjected to permanent ground displacements using the finite difference method, 2021a.

[2] Zheng, Q., Li, Y., Yoosef-Ghodsi, N., Fowler, M., Kainat, M., Adeeb, S., A finite difference-based approach for strain demand prediction of inelastic pipes subjected to permanent ground displacements, 2021b.

[3] Allouche, I., Zheng, Q., Yoosef-Ghodsi, N., Fowler, M., Adeeb, S., (2022). Combined Effect of Pressure, Temperature & Soil Stiffness on Pipeline Strain Demand in Geohazard Zones. Proceedings of the ASME Pressure Vessels & Piping Conference, July 17-22, Las Vegas, Nevada, USA. PVP2022-83754.

[4] O'Rourke MJ, Gadicherla V, Abdoun TH. Centrifuge modeling of PGD response of buried pipe. Earthq Eng Eng 2005; 4:69-73. https://link.springer.com/content/pdf/10.1007/s11803-553 005-0025-8.pdf

[5] Ha D, Abdoun TH, O'Rourke MJ, Symans MD, O'Rourke TD, Palmer MC, Stewart HE. Buried high-density polyethylene pipelines subjected to normal and strike-slip faulting—a

[6] Rofooei FR, H. Hojat Jalali H, Attari Nader KA, Alavi M. Full-scale laboratory testing of buried pipelines subjected to permanent ground displacement caused by reverse faulting. In: Proceedings of the 15th World Conference on Earthquake Engineering; 2012. p. 24-28. https://www.iitk.ac.in/nicee/wcee/article/WCEE2012_4381.pdf

[7] Feng W, Huang R, Liu J, Xu X, Luo M. Large-scale field trial to explore landslide and pipeline interaction. Soils Found 2015;55:1466-1473. https://doi.org/10.1016/j.sandf.2015.10.011

[8] centrifuge investigation. Can Geotech J 2008;45:1733-1742. https://doi.org/10.1139/T08-550 089

[9] Newmark NM, Hall WJ. Pipeline design to resist large fault displacement. In: Proceedings of U.S. national conference on earthquake engineering; 1975. p. 416-25.

[10] Kennedy RP, Chow AW, Williamson RA. Fault movement effects on buried oil pipeline. ASCE J Transport Eng 1977; 103:617-33. https://doi.org/10.1061/TPEJAN.0000659

[11] Wang LRL, Yeh YA. A refined seismic analysis and design of buried pipeline for fault movement. Earthq Eng Struct Dyn 1985;13:75-96. https://doi.org/10.1002/eqe.4290130109

[12] Wang, LRL, Yeh YA. Seismic design of buried pipeline for fault movement effects. J. Press. Vessel Technol 1986; 108:202-208.

[13] Karamitros DK, Bouckovalas GD, Kouretzis GP. Stress analysis of buried steel pipelines at strike-slip fault crossings. Soil Dyn Earthq Eng 2007;27:200-11.

[14] Trifonov OV, Cherniy VP. Elastoplastic stress strain analysis of buried steel pipelines subjected to fault displacements with account for service loads. Soil Dyn Earthq Eng 2012; 30:298-308. https://doi.org/10.1016/j.soildyn.2011.10.001

[15] Xu L, Lin M. Analysis of buried pipelines subjected to reverse fault motion using the vector form intrinsic finite element method. Soil Dyn Earthq Eng 2017;93:61-83. 595 https://doi.org/10.1016/j.soildyn.2016.12.004

[16] Takada, S., Hassani, N., Fukuda, K., A new proposal for simplified design of buried steel pipes crossing active faults. Earthq. Eng. Struct. Dyn. 30 (8), 2001, 1243–1257.
[17] Liu, X., Zhang, H., Li, M., Xia, M., Zheng, W., Wu, K., Han, Y., Effects of steel properties on the local buckling response of high strength pipelines subjected to reverse faulting. J. Nat. Gas Sci. Eng. 33, 2016, 378–387.
[18] Vazouras, P., Dakoulas, P., Karamanos, Pipe–soil interaction and pipeline performance under strike–slip fault movements. Soil Dyn. Earthq, S.A., 2015, Eng. 72, 48–65.
[19] Sarvanis, G.C., Karamanos, S.A., Vazouras, P., Mecozzi, E., Lucci, A., Dakoulas, P., Permanent earthquake-induced actions in buried pipelines: numerical modeling and experimental verification. Earthq. Eng. Struct. Dyn. 47 (4), 2018., 966–987.
[20] Yoosef-Ghodsi, N., Zhou, J., Murray, D.W., A simplified model for evaluating strain demand in a pipeline subjected to longitudinal ground movement. In: Proceedings of the International Pipeline Conference, 2008, p. 48593.
[21] Yoosef-Ghodsi, N., Kulak, G.L., and Murray, D.W. 1994. Behavior of Girth-Welded Line Pipe, Structural Engineering Report No. 203, Department of Civil Engineering, University of Alberta, Edmonton, AB, T6G 2G7.
[22] Lin, Y., Lv, Y., Liu, X., Chen, F., Analysis of Longitudinal Mechanical Properties of Buried Suspended Pipeline Resisting Collapse, Advances in Civil Engineering, V. 2019, Article ID 3954390, 10p., 2019.
[23] Agbo, S.; Roy, K.; Adeeb, S.; Li, Y. (2022) Effects of Permanent Ground Deformation Patterns on Strain Demand of Pressurised Buried Continuous Steel Pipelines. Journal of Pipeline Systems. DOI. 10.1061/(ASCE)PS.1949-1204.0000680.
[24] American Lifelines Alliance, American Society of Civil Engineers, Guidelines for the Design of Buried Steel Pipe, 2001
[25] ASTM International, ASTM D2487, Standard Practice for Classification of Soils for Engineering Purposes (Unified Soil Classification System), 2017.
[26] CSA Group, CSA Z662:19, Oil and Gas Pipeline Systems, 2019.
[27] C-FER Technologies, a Subsidiary of Alberta Innovates, Strain Based Design, https://www.cfertech.com/2020/03/03/strain-based-design/, viewed January 21, 2022.
[28] Dassault Systems Simulia Corporation, Abaqus Overview, https://www.3ds.com/products-services/simulia/products/abaqus/, 2022.
[29] ASME B31.4, 2019 Edition, November 1, 2019 - Pipeline Transportation Systems for Liquids and Slurries.

CHAPTER 4

SUMMARY AND CONCLUSION

An effective model has been developed using the finite element method in Abaqus/Standard to simulate a fully operational pipeline subject to deformation induced by geohazard ground deformation. By incorporating effects of internal operating pressure and temperature variation, the full mechanism of the pipeline can be emulated and tested against several hypothetical case studies. Results from four indictive case studies of varying soil strength (weak, intermediate, strong, weak – half $P\&\Delta T$) suggest that the combined effect of internal pressure and temperature amplify the overall pipe deformation (axial & vertical) and strains, with significant impact on compressive strain at the top and bottom extreme fibres of the pipes' cross-section. This is evident based on the discrepancy in results on the pipelines strain demand and deformation response between cases with and without pressure & temperature loading. Results also suggest that additional stresses attributed to hoop stress generated by internal pressure in combination with thermal stress may promote material plasticity, where the soil is expected to yield at earlier magnitudes of ground motion, and strains are expected to increase. This is significant as previous models have excluded the influence of pressure and temperature on the nonlinear strain demand of pipes subject to ground movement, potentially underpredicting pipe strains. Including the full mechanism of an operating pipe during the event of a geohazard provides greater relatability to real-world pipe operation, and enhances results that can be utilized for design, analysis, or construction pre-screening.

Furthermore, conclusions discovered by incorporating internal operating pressure and temperature change in pipelines subject to geohazard ground displacement in Abaqus provide justification for the development of a new proposed method. Methods established by Zheng et al. (2021b) developed to predict steel pipe deformation and strain response are extended to include the effects of internal operating pressure and temperature change. This considers the pipe to be in the biaxial state of stress due to pressure as well as use of the associated Von Mises flow rule which considers material plasticity and the equivalent yield stress hypothesis. As a result, the initial pseudo-strain hypothesis developed by Yoosef-Ghodsi et al. (2008) can be incorporated into the expressions of the internal axial force and bending moment equations, respectively. As a result, the longitudinal strain is acquired based on the governing equations and law of continuity to the axial and lateral pipe displacement components. The equations are solved numerically using the finite difference method in Python, which was also enhanced by implementing an incremental solver with regards to the magnitude of applied ground displacement to help retain convergent solutions when necessary. The proposed method was than tested against several hypothetical simulations developed in Abaqus Standard to verify the precision of this new method.

Results from four hypothetical cases pertaining to pipe load with varying combinations of internal pressure and temperature demonstrated that the proposed method has a great predictive capability for pipe strain demand and displacement response when compared to Abaqus, retaining the level of accuracy of the original model developed by Zheng et al. (2021b). The proposed method was also utilized to predict the strain response at increasing increments of ground movement (δ = 100 to 1000 mm), different ground intersection angles (β = 0˚, 60˚, 90˚), large levels of ground movement (δ = 1 m to 4 m), and a large segment of pipe (L = 446 m) with a specified geohazard condition (Landslide with L_2 = 146 m, β = 30˚). Results indicate that the proposed method accurately incorporates the effects of internal operating pressure and temperature change when the pipe is in an elastic and inelastic material state, even at large levels of strain and large pipeline length. Additionally, it is demonstrated that the proposed method accurately determines the material response of the pipe when compared to Abaqus, appropriately predicting the magnitude and location of the compressive and tensile strain demand, as well as the elastic-plastic state of the pipe at varying magnitudes of δ. This confirms the extensive application of the proposed method with respect to varying types of geohazards, magnitudes of operating pressure, and temperature change. This enhanced method offers an alternative analysis approach to be used in preliminary design or safety pre-screening, with future work involving applying the method to a reliability-based assessment of pipes buried through geohazard zones.

BIBLIOGRAPHY

- Newman, N., Pipeline & Gas Journal, Appropriate Methods for Repairing Pipelines (2020), https://pgjonline.com/news/2020/12-december/appropriate-methods-for-repairing-pipelines

- Zheng, Q., Graf-Alexiou, G., Li, Y., Yoosef-Ghodsi, N., Fowler, M., Kainat, M., Adeeb, S., Strain demand of elastic pipes subjected to permanent ground displacements using the finite difference method, 2021a.

- Zheng, Q., Li, Y., Yoosef-Ghodsi, N., Fowler, M., Kainat, M., Adeeb, S., A finite difference-based approach for strain demand prediction of inelastic pipes subjected to permanent ground displacements, 2021b.

- Allouche, I., Zheng, Q., Yoosef-Ghodsi, N., Fowler, M., Adeeb, S., (2022). Combined Effect of Pressure, Temperature & Soil Stiffness on Pipeline Strain Demand in Geohazard Zones. Proceedings of the ASME Pressure Vessels & Piping Conference, July 17-22, Las Vegas, Nevada, USA. PVP2022-83754.

- O'Rourke MJ, Gadicherla V, Abdoun TH. Centrifuge modeling of PGD response of buried pipe. Earthq Eng Eng 2005; 4:69-73. https://link.springer.com/content/pdf/10.1007/s11803-553_005-0025-8.pdf

- Ha D, Abdoun TH, O'Rourke MJ, Symans MD, O'Rourke TD, Palmer MC, Stewart HE. Buried high-density polyethylene pipelines subjected to normal and strike-slip faulting—a

- Rofooei FR, H. Hojat Jalali H, Attari Nader KA, Alavi M. Full-scale laboratory testing of buried pipelines subjected to permanent ground displacement caused by reverse faulting. In: Proceedings of the 15th World Conference on Earthquake Engineering; 2012. p. 24-28. https://www.iitk.ac.in/nicee/wcee/article/WCEE2012_4381.pdf

- Feng W, Huang R, Liu J, Xu X, Luo M. Large-scale field trial to explore landslide and pipeline interaction. Soils Found 2015;55:1466-1473. https://doi.org/10.1016/j.sandf.2015.10.011

- centrifuge investigation. Can Geotech J 2008;45:1733-1742. https://doi.org/10.1139/T08-550 089

- Newmark NM, Hall WJ. Pipeline design to resist large fault displacement. In: Proceedings of U.S. national conference on earthquake engineering; 1975. p. 416-25.

- Kennedy RP, Chow AW, Williamson RA. Fault movement effects on buried oil pipeline. ASCE J Transport Eng 1977; 103:617-33. https://doi.org/10.1061/TPEJAN.0000659

- Wang LRL, Yeh YA. A refined seismic analysis and design of buried pipeline for fault movement. Earthq Eng Struct Dyn 1985;13:75-96. https://doi.org/10.1002/eqe.4290130109

- Wang, LRL, Yeh YA. Seismic design of buried pipeline for fault movement effects. J. Press. Vessel Technol 1986; 108:202-208.

- Karamitros DK, Bouckovalas GD, Kouretzis GP. Stress analysis of buried steel pipelines at strike-slip fault crossings. Soil Dyn Earthq Eng 2007;27:200-11.

- Trifonov OV, Cherniy VP. Elastoplastic stress strain analysis of buried steel pipelines subjected to fault displacements with account for service loads. Soil Dyn Earthq Eng 2012; 30:298-308. https://doi.org/10.1016/j.soildyn.2011.10.001

- Xu L, Lin M. Analysis of buried pipelines subjected to reverse fault motion using the vector form intrinsic finite element method. Soil Dyn Earthq Eng 2017;93:61-83. 595 https://doi.org/10.1016/j.soildyn.2016.12.004

- Takada, S., Hassani, N., Fukuda, K., A new proposal for simplified design of buried steel pipes crossing active faults. Earthq. Eng. Struct. Dyn. 30 (8), 2001, 1243–1257.

- Liu, X., Zhang, H., Li, M., Xia, M., Zheng, W., Wu, K., Han, Y., Effects of steel properties on the local buckling response of high strength pipelines subjected to reverse faulting. J. Nat. Gas Sci. Eng. 33, 2016, 378–387.

- Vazouras, P., Dakoulas, P., Karamanos, Pipe–soil interaction and pipeline performance under strike–slip fault movements. Soil Dyn. Earthq, S.A., 2015, Eng. 72, 48–65.

- Sarvanis, G.C., Karamanos, S.A., Vazouras, P., Mecozzi, E., Lucci, A., Dakoulas, P., Permanent earthquake-induced actions in buried pipelines: numerical modeling and experimental verification. Earthq. Eng. Struct. Dyn. 47 (4), 2018., 966–987.

- Yoosef-Ghodsi, N., Zhou, J., Murray, D.W., A simplified model for evaluating strain demand in a pipeline subjected to longitudinal ground movement. In: Proceedings of the International Pipeline Conference, 2008, p. 48593.

- Yoosef-Ghodsi, N., Kulak, G.L., and Murray, D.W. 1994. Behavior of Girth-Welded Line Pipe, Structural Engineering Report No. 203, Department of Civil Engineering, University of Alberta, Edmonton, AB, T6G 2G7.

- Lin, Y., Lv, Y., Liu, X., Chen, F., Analysis of Longitudinal Mechanical Properties of Buried Suspended Pipeline Resisting Collapse, Advances in Civil Engineering, V. 2019, Article ID 3954390, 10p., 2019.

- Agbo, S.; Roy, K.; Adeeb, S.; Li, Y. (2022) Effects of Permanent Ground Deformation Patterns on Strain Demand of Pressurised Buried Continuous Steel Pipelines. Journal of Pipeline Systems. DOI. 10.1061/(ASCE)PS.1949-1204.0000680.

- American Lifelines Alliance, American Society of Civil Engineers, Guidelines for the Design of Buried Steel Pipe, 2001

- ASTM International, ASTM D2487, Standard Practice for Classification of Soils for Engineering Purposes (Unified Soil Classification System), 2017.

- CSA Group, CSA Z662:19, Oil and Gas Pipeline Systems, 2019.

- C-FER Technologies, a Subsidiary of Alberta Innovates, Strain Based Design, https://www.cfertech.com/2020/03/03/strain-based-design/, viewed January 21, 2022.

- Dassault Systems Simulia Corporation, Abaqus Overview, https://www.3ds.com/products-services/simulia/products/abaqus/, 2022

- ASME B31.4, 2019 Edition, November 1, 2019 - Pipeline Transportation Systems for Liquids and Slurries.

APPENDIX A: Sub-function of Python Code Used for Predictive Method

```
import numpy as np
from scipy import optimize
import math

#%% Soil springs
def Tu0(x, Tu, kTu):
    return Tu*np.tanh(kTu*x) #N/mm returns +ve in the direction of x
def TuU(x, Tu, kTu, U):
    return -Tu*np.tanh(kTu*(x-U)) #N/mm returns +ve in the direction of x
def Pu0(x, Qu, kQu):
    # return Qd*np.tanh(kQd*x)+Qu*np.tanh(kQu*x) #N/mm returns +ve in the vertical direction of y
    return Qu*np.tanh(kQu*x)
def PuW(x, Qd, kQd, W):
    # return -Qd*np.tanh(kQd*(x-W))-Qu*np.tanh(kQu*(x-W)) #N/mm returns +ve in the vertical direction of y
    return -Qd*np.tanh(kQd*(x-W))

#%% Function definition: centered finit difference
def firstD(a,c,h): # a: the a(i-1); aii: a(i+1)
    p=(c-a)/(2*h) # ai: the a(i)
    return p
def secondD(a,b,c,h):
    pp=(c-2*b+a)/(h**2)
    return pp

#%% Function definition: N and M in material nonlinearity
def NMnon(du,dw,d2w, basic_params):
    D, t, A, Eel, EplT,EplC, epsilon_YT, epsilon_YC, epsilon_initial = basic_params
    eA=du+1/2*(dw)**2 + epsilon_initial
    eBmax=D/2*(d2w)   # If -, then H2 = MIN, H1 = MAX
    if np.abs(d2w)<= 1e-15:
        M = 0.
        if eA>epsilon_YT:
            N=A*(Eel*epsilon_YT+EplT*(eA-epsilon_YT))
        elif eA<epsilon_YC:
            N=A*(Eel*epsilon_YC+EplC*(eA-epsilon_YC))
        else:
            N=A*Eel*eA
```

```
else:
    hty=D/2-D*(epsilon_YT-eA)/(2*eBmax)
    hcy=D/2+D*(-epsilon_YC+eA)/(2*eBmax)
    # print(hty, hcy)
    # I=np.sign(hcy-hty)
    H1=min(hty,hcy)
    H2=max(hty,hcy)
    # H2=min(hty,hcy)
    # H1=max(hty,hcy)
    if H1>=D:
        phi1=np.pi
    elif H1<=0:
        phi1=0
    else:
        phi1=np.arccos((D-2*H1)/D)
    if H2>=D:
        phi2=np.pi
    elif H2<=0:
        phi2=0
    else:
        phi2=np.arccos((D-2*H2)/D)
    if hcy > hty: # Ii = 1
        N = (D - t)*t*(
            (EplC*np.pi + (Eel - EplC)*phi2)*eA
            - ((Eel - EplT)*np.sin(phi1) - (Eel - EplC)*np.sin(phi2))*eBmax
            - (Eel - EplT)*(eA - epsilon_YT)*phi1
            + (Eel - EplC)*(np.pi - phi2)*epsilon_YC
            )
        M = 0.25*(D - t)**2*t*(
            (EplC*np.pi - (Eel - EplT)*(phi1 + np.sin(phi1)*np.cos(phi1)) + (Eel - EplC)*(phi2+np.sin(phi2)*np.cos(phi2)))*eBmax
            - 2*((Eel - EplT)*np.sin(phi1) - (Eel - EplC)*np.sin(phi2))*eA
            + 2*np.sin(phi1)*epsilon_YT*(Eel - EplT) - 2*np.sin(phi2)*epsilon_YC*(Eel - EplC)
            )
    else:
        N = (D - t)*t*(
            (EplT*np.pi + (Eel - EplT)*phi2)*eA
            - ((Eel - EplC)*np.sin(phi1) - (Eel - EplT)*np.sin(phi2))*eBmax
            - (Eel - EplC)*(eA - epsilon_YC)*phi1
            + (Eel - EplT)*(np.pi - phi2)*epsilon_YT
            )
```

```
        M = 0.25*(D - t)**2*t*(
            (EplT*np.pi - (Eel - EplC)*(phi1 + np.sin(phi1)*np.cos(phi1)) + (Eel - EplT)*(phi2+np.sin(phi2)*np.cos(phi2)))*eBmax
            - 2*((Eel - EplC)*np.sin(phi1) - (Eel - EplT)*np.sin(phi2))*eA
            + 2*np.sin(phi1)*epsilon_YC*(Eel - EplC) - 2*np.sin(phi2)*epsilon_YT*(Eel - EplT)
            )
    return [N,M]


#%% Equations
def Equations(x, zero_arrays, Equations_params, soil_params, MNnon_params):       # Finite difference z is an array containing us followed by ws with length nodes.
    (upL, uppL, wpL, wppL, NL, NwpL, ML, NpL, MpL, MppL,
     upM, uppM, wpM, wppM, NM, MM, NpM, MpM, NwpM, MppM,
     upR, uppR, wpR, wppR, NR, MR, NpR, MpR, NwpR, MppR) = zero_arrays
    hL, hM, hR, nodeL, nodeM, nodeR, coordinate = Equations_params
    Tu, kTu, U, Qu, kQu, Qd, kQd, W = soil_params
    D, t, A, Eel, EplT,EplC, epsilon_YT, epsilon_YC, epsilon_initial = MNnon_params

    l=int(len(x)/2)
    u=x[:l]
    w=x[l:]
    # Range function doesn't consider last value
    # Forward
    upL[0]=(u[1]-u[0])/hL
    wpL[0]=(w[1]-w[0])/hL
    wppL[0]=(w[2]-2*w[1]+w[0])/hL**2
    [NL[0],ML[0]]=NMnon(upL[0],wpL[0],wppL[0], MNnon_params)
    # Backward
    upL[nodeL-1]=(u[nodeL-2]-u[nodeL-1])/(-hL)
    wpL[nodeL-1]=(w[nodeL-2]-w[nodeL-1])/(-hL)
    wppL[nodeL-1]=(w[nodeL-1]-2*w[nodeL-2]+w[nodeL-3])/hL**2
    [NL[nodeL-1],ML[nodeL-1]]=NMnon(upL[nodeL-1], wpL[nodeL-1], wppL[nodeL-1], MNnon_params)
    for i in range(1, nodeL-1): #First derivatives and second derivatives start from second node to one before last
        upL[i]=firstD(u[i-1],u[i+1],hL)
        uppL[i]=secondD(u[i-1],u[i],u[i+1],hL)
        wpL[i]=firstD(w[i-1],w[i+1],hL)
        wppL[i]=secondD(w[i-1],w[i],w[i+1],hL)
        [NL[i],ML[i]]=NMnon(upL[i],wpL[i],wppL[i], MNnon_params)
    for i in range(1, nodeL-1): #First derivatives and second derivatives start from second node to one before last
        NpL[i]=firstD(NL[i-1],NL[i+1],hL)
```

```
    MppL[i]=secondD(ML[i-1],ML[i],ML[i+1],hL)
    NwpL[i]=firstD(NL[i-1]*wpL[i-1],NL[i+1]*wpL[i+1],hL)

# Forward
upM[0]=(u[nodeL+1]-u[nodeL+0])/hM
wpM[0]=(w[nodeL+1]-w[nodeL+0])/hM
wppM[0]=(w[nodeL+2]-2*w[nodeL+1]+w[nodeL+0])/hM**2
[NM[0],MM[0]]=NMnon(upM[0],wpM[0],wppM[0], MNnon_params)
# Backward
upM[nodeM-1]=(u[nodeL+nodeM-2]-u[nodeL+nodeM-1])/(-hM)
wpM[nodeM-1]=(w[nodeL+nodeM-2]-w[nodeL+nodeM-1])/(-hM)
wppM[nodeM-1]=(w[nodeL+nodeM-1]-2*w[nodeL+nodeM-2]+w[nodeL+nodeM-3])/hM**2
[NM[nodeM-1],MM[nodeM-1]]=NMnon(upM[nodeM-1],wpM[nodeM-1],wppM[nodeM-1], MNnon_params)
for i in range(1, nodeM-1):
    upM[i]=firstD(u[i-1+nodeL],u[i+1+nodeL],hM)
    uppM[i]=secondD(u[i-1+nodeL],u[i+nodeL],u[i+1+nodeL],hM)
    wpM[i]=firstD(w[i-1+nodeL],w[i+1+nodeL],hM)
    wppM[i]=secondD(w[i-1+nodeL],w[i+nodeL],w[i+1+nodeL],hM)
    [NM[i],MM[i]]=NMnon(upM[i],wpM[i],wppM[i], MNnon_params)
for i in range(1, nodeM-1): #First derivatives and second derivatives start from second node to one before last
    NpM[i]=firstD(NM[i-1],NM[i+1],hM)
    MppM[i]=secondD(MM[i-1],MM[i],MM[i+1],hM)
    NwpM[i]=firstD(NM[i-1]*wpM[i-1],NM[i+1]*wpM[i+1],hM)

# Forward
upR[0]=(u[nodeL+nodeM+1]-u[nodeL+nodeM+0])/hR
wpR[0]=(w[nodeL+nodeM+1]-w[nodeL+nodeM+0])/hR
wppR[0]=(w[nodeL+nodeM+2]-2*w[nodeL+nodeM+1]+w[nodeL+nodeM+0])/hR**2
[NR[0],MR[0]]=NMnon(upR[0],wpR[0],wppR[0], MNnon_params)
# Backward
upR[nodeR-1]=(u[nodeL+nodeM+nodeR-1]-u[nodeL+nodeM+nodeR-2])/hR
wpR[nodeR-1]=(w[nodeL+nodeM+nodeR-1]-w[nodeL+nodeM+nodeR-2])/hR
wppR[nodeR-1]=(w[nodeL+nodeM+nodeR-1]-2*w[nodeL+nodeM+nodeR-2]+w[nodeL+nodeM+nodeR-3])/hM**2
[NR[nodeR-1],MR[nodeR-1]]=NMnon(upR[nodeR-1],wpR[nodeR-1],wppR[nodeR-1], MNnon_params)
for i in range(1, nodeR-1):
    upR[i]=firstD(u[i-1+nodeL+nodeM],u[i+1+nodeL+nodeM],hR)
    uppR[i]=secondD(u[i-1+nodeL+nodeM],u[i+nodeL+nodeM],u[i+1+nodeL+nodeM],hR)
    wpR[i]=firstD(w[i-1+nodeL+nodeM],w[i+1+nodeL+nodeM],hR)
    wppR[i]=secondD(w[i-1+nodeL+nodeM],w[i+nodeL+nodeM],w[i+1+nodeL+nodeM],hR)
    [NR[i],MR[i]]=NMnon(upR[i],wpR[i],wppR[i], MNnon_params)
```

```
    for i in range(1, nodeR-1): #First derivatives and second derivatives start from second node to one before last
        NpR[i]=firstD(NR[i-1],NR[i+1],hR)
        MppR[i]=secondD(MR[i-1],MR[i],MR[i+1],hR)
        NwpR[i]=firstD(NR[i-1]*wpR[i-1],NR[i+1]*wpR[i+1],hR)
# Establishing equations
    EqsLu = np.array([NpL[i] - Tu0(u[i], Tu, kTu) for i in range(1, nodeL - 1)])
    EqsLw = np.array([MppL[i] - NwpL[i] + Pu0(w[i], Qu, kQu) for i in range(2, nodeL - 2)])
    EqsMu = np.array([NpM[i] + TuU(u[i + nodeL], Tu, kTu, U) for i in range(1, nodeM - 1)])
    EqsMw = np.array([MppM[i] - NwpM[i] - PuW(w[i + nodeL], Qd, kQd, W) for i in range(2, nodeM - 2)])
    EqsRu = np.array([NpR[i] - Tu0(u[i + nodeL + nodeM], Tu, kTu) for i in range(1, nodeR - 1)])
    EqsRw = np.array([MppR[i] - NwpR[i] + Pu0(w[i + nodeL + nodeM], Qu, kQu) for i in range(2, nodeR - 2)])

    BCs=[]
    BCs.append(u[0])#Fixed horizontal displacement end 1
    BCs.append(u[nodeL+nodeM+nodeR-1])#Fixed horizontal displacement far end
    BCs.append(w[0])#Fixed vertical displacement end 1
    BCs.append(w[nodeL+nodeM+nodeR-1])#Fixed vertical displacement far end
    BCs.append((w[1]-w[0])/hL)#Fixed rotation near end
    BCs.append((w[nodeL+nodeM+nodeR-1]-w[nodeL+nodeM+nodeR-2])/hR)#Fixed rotation far end
    # First connection
    BCs.append(u[nodeL-1]-u[nodeL]) #connectivity of u
    BCs.append(w[nodeL-1]-w[nodeL]) #connectivity of w
    BCs.append((u[nodeL-1]-u[nodeL-2])/(coordinate[nodeL-1]-coordinate[nodeL-2])-(u[nodeL+1]-u[nodeL])/(coordinate[nodeL+1]-
coordinate[nodeL])) #connectivity of first slope of u
    BCs.append((w[nodeL-1]-w[nodeL-2])/(coordinate[nodeL-1]-coordinate[nodeL-2])-(w[nodeL+1]-w[nodeL])/(coordinate[nodeL+1]-
coordinate[nodeL])) #next is connectivity of first slope of w
    BCs.append((w[nodeL-3]-2*w[nodeL-2]+w[nodeL-1])/(hL**2)-(w[nodeL+2]-2*w[nodeL+1]+w[nodeL])/(hM**2))      #connectivity      of      second
derivative of w
    BCs.append((w[nodeL-1]-3*w[nodeL-2]+3*w[nodeL-3]-w[nodeL-4])/(hL**3)-(w[nodeL+3]-3*w[nodeL+2]+3*w[nodeL+1]-w[nodeL])/(hM**3))
#connectivity of third derivative of w
    # Second connection
    BCs.append(u[nodeM+nodeL-1]-u[nodeM+nodeL]) #connectivity of u
    BCs.append(w[nodeM+nodeL-1]-w[nodeM+nodeL]) #connectivity of w
    BCs.append((u[nodeM+nodeL-1]-u[nodeM+nodeL-2])/(coordinate[nodeM+nodeL-1]-coordinate[nodeM+nodeL-2])-(u[nodeM+nodeL+1]-
u[nodeM+nodeL])/(coordinate[nodeM+nodeL+1]-coordinate[nodeM+nodeL])) #connectivitify of first slope of u
    BCs.append((w[nodeM+nodeL-1]-w[nodeM+nodeL-2])/(coordinate[nodeM+nodeL-1]-coordinate[nodeM+nodeL-2])-(w[nodeM+nodeL+1]-
w[nodeM+nodeL])/(coordinate[nodeM+nodeL+1]-coordinate[nodeM+nodeL])) #next is connectivity of first slope of w
    BCs.append((w[nodeM+nodeL-3]-2*w[nodeM+nodeL-2]+w[nodeM+nodeL-1])/(hM**2)-(w[nodeM+nodeL+2]-
2*w[nodeM+nodeL+1]+w[nodeM+nodeL])/(hR**2)) #connectivity of second derivative of w
```

```
    BCs.append((w[nodeM+nodeL-1]-3*w[nodeM+nodeL-2]+3*w[nodeM+nodeL-3]-w[nodeM+nodeL-4])/(hM**3)-(w[nodeM+nodeL+3]-
3*w[nodeM+nodeL+2]+3*w[nodeM+nodeL+1]-w[nodeM+nodeL])/(hR**3)) #connectivity of third derivative of w
    BCs = np.array(BCs)
    Eqs = np.concatenate((EqsLu, EqsLw, EqsMu, EqsMw, EqsRu, EqsRw, BCs))
    return Eqs

def task(params):
    (D, t,
     Eel, EplT,EplC,sigmaYT, sigmaYC, epsilon_YT, epsilon_YC, epsilon_initial,
     delta, beta,
     Tu, kTu, Qu, kQu, Qd, kQd,
     soilL, soilM, soilR, nodeL, nodeM, nodeR,IG) = params

    soilL = soilL * 1000. # mm
    soilM = soilM * 1000.
    soilR = soilR * 1000.

    # epsilonY = sigmaY/Eel # Yield strain
    nodes = nodeL + nodeM + nodeR
    hL = soilL / (nodeL - 1)
    hM = soilM / (nodeM - 1)
    hR = soilR / (nodeR - 1)
    coordinateL = np.array([i * hL for i in range(nodeL)])
    coordinateM = np.array([soilL + i * hM for i in range(nodeM)])
    coordinateR = np.array([soilL + soilM + i * hR for i in range(nodeR)])
    coordinate = np.concatenate((coordinateL, coordinateM, coordinateR))

    A = 1 / 4 * np.pi * (D ** 2 - (D - 2 * t) ** 2)    # Section area, mm^2
    U = round(delta * np.cos(beta * np.pi / 180) * 1000, 2)    # Horizontal displacement, mm
    W = round(delta * np.sin(beta * np.pi / 180) * 1000, 2)    # Vertical displacement, mm

    upL = np.zeros(nodeL)
    uppL = np.zeros(nodeL)
    wpL = np.zeros(nodeL)
    wppL = np.zeros(nodeL)
    NL = np.zeros(nodeL)
    NwpL = np.zeros(nodeL)
    ML = np.zeros(nodeL)
    NpL = np.zeros(nodeL)
    MpL = np.zeros(nodeL)
```

```
MppL = np.zeros(nodeL)

upM = np.zeros(nodeM)
uppM = np.zeros(nodeM)
wpM = np.zeros(nodeM)
wppM = np.zeros(nodeM)
NM = np.zeros(nodeM)
MM = np.zeros(nodeM)
NpM = np.zeros(nodeM)
MpM = np.zeros(nodeM)
NwpM = np.zeros(nodeM)
MppM = np.zeros(nodeM)

upR = np.zeros(nodeR)
uppR = np.zeros(nodeR)
wpR = np.zeros(nodeR)
wppR = np.zeros(nodeR)
NR = np.zeros(nodeR)
MR = np.zeros(nodeR)
NpR = np.zeros(nodeR)
MpR = np.zeros(nodeR)
NwpR = np.zeros(nodeR)
MppR = np.zeros(nodeR)

zero_arrays = (upL, uppL, wpL, wppL, NL, NwpL, ML, NpL, MpL, MppL,
  upM, uppM, wpM, wppM, NM, MM, NpM, MpM, NwpM, MppM,
  upR, uppR, wpR, wppR, NR, MR, NpR, MpR, NwpR, MppR)

#IG = np.zeros(2 * nodes)
# Equation params: x, zero_arrays, Equations_params, NMnon_params, other_params
root = optimize.root(
    Equations,
    IG,
    jac=False,
    tol=1e-10,
    args=(zero_arrays,
        (hL, hM, hR, nodeL, nodeM, nodeR, coordinate),
        (Tu, kTu, U, Qu, kQu, Qd, kQd, W),
        (D, t, A, Eel, EplT,EplC, epsilon_YT, epsilon_YC, epsilon_initial))
    )
```

```
#%% Extract the deformation
root_success = root.success
loc = np.delete(coordinate/1000., [nodeL - 1, nodeL+nodeM - 1])
# significant_digits = 5
loc = [round(i, 2) for i in loc]
u = root.x[:nodeL+nodeM+nodeR]/1000.
w = root.x[nodeL+nodeM+nodeR:]/1000.
u = np.delete(u, [nodeL - 1, nodeL+nodeM - 1])
w = np.delete(w, [nodeL - 1, nodeL+nodeM - 1])
u = [round(i, 3 -int(math.floor(math.log10(abs(i))))) for i in u]
w = [round(i, 3 -int(math.floor(math.log10(abs(i))))) for i in w]
#%% Calculate the strain
dudx = np.concatenate((upL, upM, upR))
dwdx = np.concatenate((wpL, wpM, wpR))
d2wdx2 = np.concatenate((wppL, wppM, wppR))
eTop = dudx + 1 / 2 * dwdx ** 2 + D / 2 * d2wdx2
eBot = dudx + 1 / 2 * dwdx ** 2 - D / 2 * d2wdx2
eTop = np.delete(eTop, [nodeL - 1, nodeL + nodeM - 1])
eBot = np.delete(eBot, [nodeL - 1, nodeL + nodeM - 1])
eTop = [round(i, 5 -int(math.floor(math.log10(abs(i))))) for i in eTop]
eBot = [round(i, 5 -int(math.floor(math.log10(abs(i))))) for i in eBot]
#%% Find the location of strain demand
eL = np.concatenate((eTop, eBot))
significant_digits = 5
eL=[round(i, 5-int(math.floor(math.log10(abs(i))))) for i in eL]
eT = np.max(eL)
eC = np.min(eL)
loc_eL = np.concatenate((loc, loc))
loc_eT = np.where(eL==eT)
loc_eC = np.where(eL==eC)
loc_TSD = loc_eL[loc_eT]
loc_CSD = loc_eL[loc_eC]
#%% Significant digits
data = np.transpose(np.vstack((loc, u, w, eTop, eBot)))
return (root_success, eT, eC, loc_TSD, loc_CSD, data)
```

APPENDIX B: Main-Function of Python Code Used for Predictive Method

```
# Title: Pipe deformation due to ground movement (three segments)
# Author: Samuel Allouche
# Date: 20220520

# Clear all variables
from IPython import get_ipython
get_ipython().magic('reset -sf')
# Clear Console
try:
    from IPython import get_ipython
    get_ipython().magic('clear')
    get_ipython().magic('reset -f')
except:
    pass
# Import functions needed
import Subfun_PT
import numpy as np
import math
from colorama import Fore, Style
#%% Parameter definition (Need to change based on your study cases)
# Pipe geometries
OD = 508 # Diameter, mm
WT = 7.14 # Wall thickness, mm

# Material properties (Bilinear model)
Ee = 199e3 # Young's modulus, MPa
sY = 450 # Yield strength, MPa
eY = sY / Ee
sU = 663 # Ultimate strength, MPa
eU = 0.03 # Ultimate strain
Ep = (sU-sY)/(eU-eY) # Plastic slope (uniaxial)

# Ground displacement
Delta = 0.5 # Ground displacement, m
Beta = 90 # Intersection angle, °

# Horizontal & vertical bi-linear force
```

```
Tu = 14 # Axial soil spring resistance, kN/m
kTu = 0.005 # unit: m
Pu2 = 40 # Lateral soil spring resistance, kN/m (symmetric: Pu2 = Pu13; non-symmetric: Pu2 != Pu13)
kPu2 = 0.046
Pu13 = 513
kPu13 = 0.092

# Pressure and temperature

Pmax = -0.8*sY/(OD-2*WT)*(2*WT) # Maximum Allowable Internal Pressure (negative into pipe walls)
P = -Pmax # Pressure, MPa (This value is negative)
nu = 0.3 # Possion's ratio
Delta_t = 60 # Temperature change (current T - previous T)
alpha = 12.e-6 # Coef. thermal expansion
sigma_2 = P*(OD-2*WT)/(2*WT) # hoop stress, MPa
x = alpha*Delta_t # Thermal strain

sigma_initial = np.piecewise(x, [np.abs(x) <= eY, np.abs(x) > eY],
                             [lambda x:nu*sigma_2 - Ee*x, lambda x: nu*sigma_2 - (Ee*eY + Ep*(x-eY))])
e_initial = sigma_initial/Ee

### Biaxial stress-strain curve (axial direction)
sYT = 0.5 * (sigma_2 + np.sqrt(4*sY**2 - 3*sigma_2**2)) # Equivalent Sy tension, MPa
sYC = 0.5 * (sigma_2 - np.sqrt(4*sY**2 - 3*sigma_2**2)) # Equivalent Sy compression, MPa
e_YT = (sYT-nu*sigma_2)/Ee # Equivalent ey tension
e_YC = (sYC-nu*sigma_2)/Ee # Equivalent ey compression
h = (Ee*Ep)/(Ee-Ep)

#%% Plastic slopes EpC & EpT for material non-linearity

# Elastic stress-strain
ne = 50
incr1 = (sYT-sYC)/(ne-1)
se1 = np.arange(sYC,sYT,incr1)

ee1 = np.zeros(len(se1))
for i in range (len(se1)):
    ee1[i] = (se1[i]-nu*sigma_2)/Ee
```

```
# Plastic state

# Tensile
nitr = 50
incr2 = (1000-sYT)/(nitr-1)
sp1T = np.arange(sYT,1000+incr2,incr2)

# Compressive
incr3 = (-1000-sYC)/(nitr-1)
sp1C = np.arange(sYC,-1000+incr3,incr3)

# Tensile bot
botT = -2*(-2*sYT+sigma_2)+2*np.sqrt(3)*sigma_2*math.atan((-2*sYT+sigma_2)/(np.sqrt(3)*sigma_2))

# Compressive bot
botC = -2*(-2*sYC+sigma_2)+2*np.sqrt(3)*sigma_2*math.atan((-2*sYC+sigma_2)/(np.sqrt(3)*sigma_2))

# Tensile top

topT = np.zeros(len(sp1T))
for i in range (len(sp1T)):
    topT[i] = -2*(-2*sp1T[i]+sigma_2)+2*np.sqrt(3)*sigma_2*math.atan((-2*sp1T[i]+sigma_2)/(np.sqrt(3)*sigma_2))

# Compressive top

topC = np.zeros(len(sp1C))
for i in range (len(sp1C)):
    topC[i] = -2*(-2*sp1C[i]+sigma_2)+2*np.sqrt(3)*sigma_2*math.atan((-2*sp1C[i]+sigma_2)/(np.sqrt(3)*sigma_2))

# strains

diffT = np.zeros(len(sp1T))
for i in range (len(sp1T)):
    diffT[i] = topT[i]-botT

ep1T = np.zeros(len(sp1T))
for i in range (len(sp1T)):
    ep1T[i] = (e_YT+(1/Ee)*(sp1T[i]-sYT)+1/(4*h)*diffT[i])

diffC = np.zeros(len(sp1C))
```

```
for i in range (len(sp1C)):
    diffC[i] = topC[i]-botC

ep1C = np.zeros(len(sp1C))
for i in range (len(sp1C)):
    ep1C[i] = (e_YC+(1/Ee)*(sp1C[i]-sYC)+(1/(4*h))*diffC[i])


#Tensile plastic slope, EpT

EpT = (sp1T[-1]-sp1T[0])/(ep1T[-1]-ep1T[0])

# Compressive plastic slope, EpC

EpC = (sp1C[-1]-sp1C[0])/(ep1C[-1]-ep1C[0])

#%% Pipe length and nodes

# Pipe section length
L1= 100 # m
L2 = 10 # m
L3= 100 # m

# Node setting
node1 = 51 # Node number of segment 1 (including boundary nodes)
node2 = 11 # Node number of segment 2 (including boundary nodes)
node3 = 51 # Node number of segment 3 (including boundary nodes)
nodes = node1+node2+node3
count = 0

#%% Using incremental load


count = count + 1
IG = np.zeros(2 * nodes)
parameters = (OD, WT,
              Ee, EpT, EpC, sYT, sYC, e_YT, e_YC, e_initial,
              Delta, Beta,
              Tu, kTu, Pu2, kPu2, Pu13, kPu13,
              L1, L2, L3, node1, node2, node3,IG)
```

```
ans0 = Subfun_PT.task(parameters)
Converge = ans0[0]   # Return the result of convergence: if the calculation is convergent, return "True"; if the calculation is divergent, return
"False"
if Converge:
    last_ans = ans0
    sino = 0
else:
#%% Using incremental load
    Factor = [1000., 1.0, 10., 100., 500., 2000., 10000.]   # Factor assigned for the results of IG=0 (sometimes purely using the results of IG=0
doesn't guarantee a convergent solution, you can try to use some other initial guesses)
    MaxCal = len(Factor)
    sino = 0
    position1 = np.ones(node1-1)
    position2 = np.array([2])
    position3 = np.ones(node2-2)
    position4 = np.ones(node3-1)
    position = np.concatenate((np.concatenate((np.concatenate((np.concatenate((position1, position2)), position3)),position2)),
position4)).astype(int)
    while Converge == 0 and sino < MaxCal:
        factor = Factor[sino]
        #print(Fore.RED + 'Case ', count,': factor = ', factor)
        # print(Style.RESET_ALL)
        IG_u = np.repeat(ans0[5][:, 1], repeats = position, axis=0)
        IG_v = np.repeat(ans0[5][:, 2], repeats = position, axis=0)
        IG = np.concatenate((IG_u, IG_v)) * factor # Should *1000 to unit of mm
        parameters = (OD, WT,
                      Ee, EpT, EpC, sYT, sYC, e_YT, e_YC, e_initial,
                      Delta, Beta,
                      Tu, kTu, Pu2, kPu2, Pu13, kPu13,
                      L1, L2, L3, node1, node2, node3,IG)
        ans = Subfun_PT.task(parameters)
        Converge = ans[0]
        sino = sino + 1
        if Converge:
            last_ans = ans
    #%% Using divergent results as initial guess
    if Converge == 0:
        sino = 0
        Factor = [1000., 1.0, 10., 100., 500., 2000., 5000., 10000.]
        MaxCal = len(Factor)
```

```
        while Converge == 0 and sino < MaxCal:
            factor = Factor[sino]
            #print(Fore.GREEN + 'Case ', count,': factor = ', factor)
            # print(Style.RESET_ALL)
            IG_u = np.repeat(ans0[5][:, 1], repeats = position, axis=0)
            IG_v = np.repeat(ans0[5][:, 2], repeats = position, axis=0)
            IG = np.concatenate((IG_u, IG_v)) * factor # Should *1000 to unit of mm
            parameters = (OD, WT,
                          Ee, EpT, EpC, sYT, sYC, e_YT, e_YC, e_initial,
                          Delta, Beta,
                          Tu, kTu, Pu2, kPu2, Pu13, kPu13,
                          L1, L2, L3, node1, node2, node3,IG)
            ans0 = Subfun_PT.task(parameters)
            Converge = ans0[0]
            sino = sino + 1
            if Converge:
                last_ans = ans0
if Converge == 0:
    print(Fore.CYAN + 'This case is not convergent')
#%% Strain demand calculation (No need to change)


parameters = (OD, WT,
              Ee, EpT, EpC, sYT, sYC, e_YT, e_YC, e_initial,
              Delta, Beta,
              Tu, kTu, Pu2, kPu2, Pu13, kPu13,
              L1, L2, L3, node1, node2, node3,IG)
ans = Subfun_PT.task(parameters)

Converge = ans[0] # Return the result of convergence: if the calculation is convergent, return "True"; if the calculation is divergent, return "False"
TSD = ans[1] # Result of tensile strain demand
CSD = ans[2] # Result of compressive strain demand
loc_TSD = ans[3] # Result of coordinate of tensile strain demand
loc_CSD = ans[4] # Result of coordinate of compressive strain demand
result = ans [5] # Result of strain at the top (the second column) and the bottom (the third column) along the pipe

print('Calculation convegent? ', Converge)
if len(loc_TSD)<=1:
    print('Tensile strain demand:', '{:.5%}'.format(TSD), ', location: ', loc_TSD[0], 'm')
else:
```

```
    print('Tensile strain demand:', '{:.5%}'.format(TSD), ', location: ', loc_TSD[0], 'm', ' and ', loc_TSD[1], 'm')

if len(loc_CSD)<=1:
    print('Compressive strain demand:', '{:.5%}'.format(CSD), ', location: ', loc_CSD[0], 'm')
else:
    print('Compressive strain demand:', '{:.5%}'.format(CSD), ', location: ', loc_CSD[0], 'm', ' and ', loc_CSD[1], 'm')

print('Maximum Vertical Deformation:',max(result[:, 2]),"m")
print('Maximum Axial Deformation:',max(result[:, 1]),"m")
#%% Drawing the curve of deformation along the pipe
import matplotlib.pyplot as plt
plt.figure()
plt.subplot(211)
plt.plot(result[:, 0], result[:, 2], color = 'red', label = 'Vertical deformation')
plt.legend()
plt.xlabel("Pipe length (m)")
plt.ylabel("Pipe deformation (m)")
plt.subplot(212)
plt.plot(result[:, 0], result[:, 1], color = 'blue', label = 'Axial deformation')
plt.legend()
plt.xlabel("Pipe length (m)")
plt.ylabel("Pipe deformation (m)")
plt.figure()
plt.plot(result[:, 0], result[:, 3]*100, color = 'blue', label = 'Exterme fiber 1')
plt.plot(result[:, 0], result[:, 4]*100, color = 'red', label = 'Exterme fiber 2')
plt.legend()
plt.xlabel("Pipe length (m)")
plt.ylabel("Strain (%)")

#%% Axial Stress vs. Strain response of steel (uniaxial and biaxial)

# Plots
revesed_ep1C = np.flipud(ep1C)
revesed_sp1C = np.flipud(sp1C)
# ebi1 = np.concatenate([ep1C,ee1,ep1T])
# sbi1 = np.concatenate([sp1C,se1,sp1T])

ebi1 = np.concatenate([revesed_ep1C,ee1,ep1T])
sbi1 = np.concatenate([revesed_sp1C,se1,sp1T])
x = np.linspace(-eU, eU, 100)
```

```
eY_uni = np.piecewise(x, [x < -eY, ((x >= -eY) & (x <= eY)), x > eY], [lambda x:Ep*x + (-sY + Ep*eY), lambda x: Ee*x, lambda x: Ep*x + (sY -
Ep*eY)])
plt.figure()
plt.plot([-eU, eU], [0, 0], '-', color = 'black')
plt.plot([0, 0], [-1000, 1000], '-', color = 'black')
plt.plot(x, eY_uni, '--', color = 'blue', label = 'uniaxial', linewidth = 1.3)
plt.legend(loc = 'best')

#eY_bi = np.piecewise(x, [x < eYC, ((x >= eYC) & (x <= eYT)), x > eYT], [lambda x:EpC*(x-eYC) + sYC, lambda x: Ee*x, lambda x: EpT*(x-eYT) +
sYT])
#plt.plot(x, eY_bi, '-', color = 'red', label = 'biaxial', linewidth = 1.3)
plt.plot(ebi1, sbi1, '-', color = 'red', label = 'biaxial', linewidth = 1.3)
plt.legend(loc = 'best')
plt.xlabel('axial strain')
plt.ylabel('axial stress (MPa)')
# plt.axis([-0.03, 0.03, None, None])
plt.axis([-eU, eU, -1000, 1000])


#%% Print results to an Excel in a designated folder
import numpy as np
import pandas as pd
from datetime import datetime

now = datetime.now()   # current date and time
year = now.strftime("%Y")
month = now.strftime("%m")
day = now.strftime("%d")
date = year + month + day
doc_name = "Results_" + date + ".xlsx"
title = ['Cooridnate (m)', 'Axial deformation (m)', 'Lateral deformation (m)', 'Strain along the exterme fiber 1', 'Strain along the exterme fiber 2']
data = pd.DataFrame(result, columns = title)
# data.to_excel(r'C:\Users\zq4\Desktop\New folder\doc_name.xlsx', index = False, header=True)
# path = 'C:/Users/zq4/Desktop/New folder/new/'+doc_name
# data.to_excel(path, index = False, header=True)
# print('\nPlease enter the path to save the results (e.g., C:/Users/zq4/Desktop/New folder):')
# path = input('Folder path: ')
# path = path + '/' + doc_name
# data.to_excel(path, index = False, header=True)
## Main function runs the sub-function to solve the strain demand and display the defined results
```